Influence of Machining on the Surface Integrity and Fatigue Strength of 34CrNiMo6 Steel

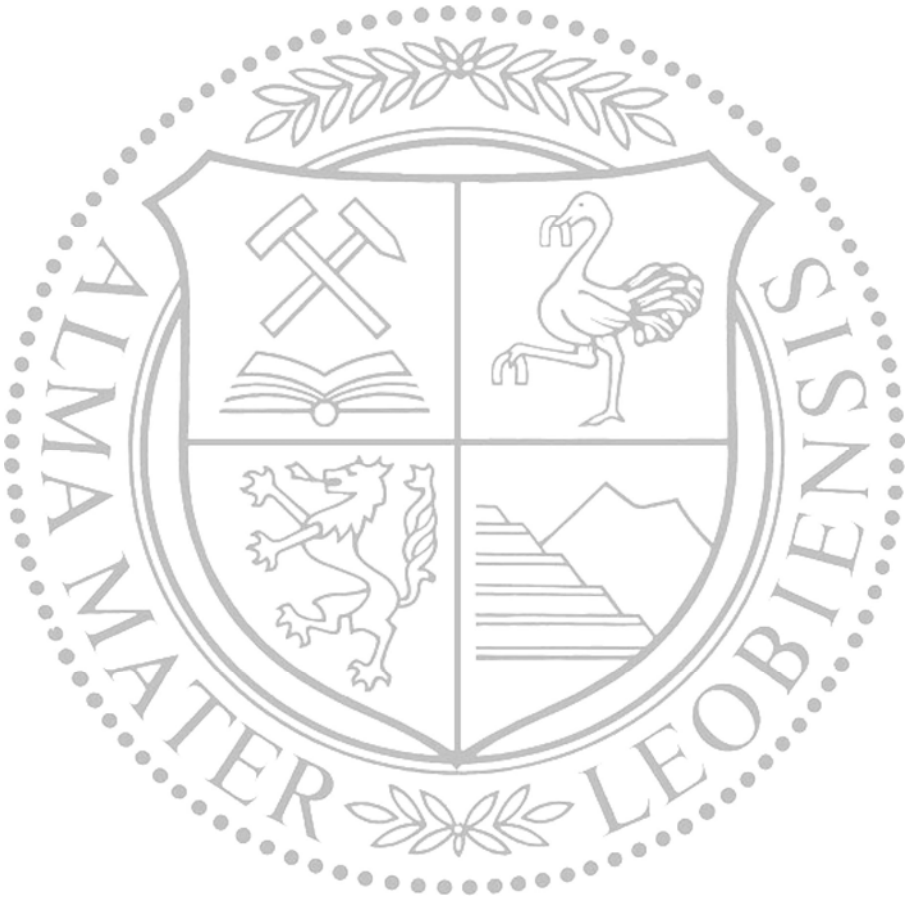

Dipl.-Ing. Ataollah Javidi

being a thesis in partial fulfilment of the requirements for the degree of a

Doctor of Montanistic Sciences (Dr. mont.)

at the University of Leoben

Leoben, July 2008

This thesis was supported by the Austrian Aeronautics Research (AAR) via a grant from the Styrian Economic Promotion Fund SFG.

Affidavit

I declare in lieu of oath that I did the PhD thesis by myself using only literature cited in this volume.

Leoben, July 2008

Ataollah Javidi

Acknowledgements

This work would have not been possible without the help, support and understanding of so many people, who made my life so much easier and enjoyable. Here is the right place to name some of them.

First of all, I would like to express my great appreciation to my supervisor Prof. Wilfried Eichlseder, head of the Department of Mechanical Engineering, for giving me the opportunity to carry out this work and for his support and friendship. Working in your team was a great pleasure and a wonderful experience.

Special thanks to the stuff and all the friends at the Department of Mechanical Engineering, past and present, for their support and more importantly, the casual chats during the innumerable coffee and tea breaks that kept me sane.

My sincere gratitude goes also to Robert Schreiber and his team at Pankl Racing Systems Group for their support in sample machining

Inexpressible thanks to my parents Leila and Ardeshir for not only believing in me and encouraging me, but much more for their love and endurance through what became a long distance relationship during my studies in Austria. In equal measure I would like to thank my sister Maryam and my brother Ali for their endless love and trust. My special thanks goes to my wife Nazanin for always being on my side. I love you all.

Contents

1. Introduction

The specification and manufacture of unimpaired or enhanced surfaces require an understanding of the interrelationship among metallurgy, machinabitity and mechanical testing. To satisfy this requirement, an encompassing discipline known as surface integrity was introduced and it has gained worldwide acceptance. Surface integrity technology describes and controls the many possible alterations produced in a surface layer during manufacture, including their effects on material properties and the performance of the surface in service. Surface integrity is achieved by the selection and control of manufacturing processes, estimating their effects on the significant engineering properties of work materials, such as fatigue performance.

The calculation of the fatigue strength for the development of structural components has become more important in recent years. In order to save time and cost, it is attempted to limit the experimental strength testing and to calculate the fatigue strength from material data. The fatigue strength of smooth, polished material specimens can be estimated or obtained from the corresponding fatigue charts with high accuracy. However, the results of fatigue strength determinations on material specimens cannot be directly applied to real components. This is because there are various parameters such as surface topography, residual stresses, hardness, microstructure, etc. that have a large impact on fatigue strength of structural components. The effect of these parameters on the fatigue strength of components is complex and causes difficulty in its evaluation with respect to the fatigue strength of material specimens.

The fatigue strength of a metal is generally defined in terms of the endurance limit and the effects of surface integrity are considered by correcting the endurance limit using the appropriate factors. The traditional correction factors provide a simple and useful means to estimate the fatigue strength related to the surface alternation they are, however, generally restricted to surface roughness analysis.

Despite the great volume of work done on the influence of surface integrity on fatigue strength, no reliable quantitative models have been developed to describe this effect. A model that would be able to predict the fatigue strength based on the surface alteration must include the quantitative analyses of surface topography, hardness and residual stresses.

Within this work, two new factors, namely, surface fatigue factor and residual stress factor were proposed to evaluate the fatigue strength of different surface conditions. The Surface fatigue factor characterizes the surface topography and the residual stress factor takes into account the multiaxiality nature of residual stresses. Both factors are presented by empirical models.

The main contribution of the present work is to build up a new relationship between surface integrity, turning process parameters and fatigue behavior of 34CrNiMo6 steel.

The outline of this thesis starts with a general overview of surface integrity and metal cutting, i.e. surface topography, residual stresses, hardness and microstructure, by reviewing the published literature. The following chapters in this thesis introduce the surface integrity and fatigue and describe some experimental aspects with regard to the investigated specimens. Subsequent to a short conclusion of the main findings, the major experimental research is given in three scientific publications, where the obtained results are comprehensively discussed.

2. Surface Integrity and Metal Cutting

A part surface has two important aspects that must be defined and controlled. The first concerns the geometric irregularities of the surface, and the second concerns the metallurgical alterations of the surface and the surface layer. The first aspect is termed surface finish or surface topography and the second one surface integrity [1]. Field and Kahles [2] described surface integrity as the relationship between surface geometrical values such as surface roughness and the physical properties such as residual stresses, hardness and structure of the surface layers. Both of these factors, surface topography and surface metallurgy, act together and affect the fatigue strength in a complex manner, Figure 2.1.

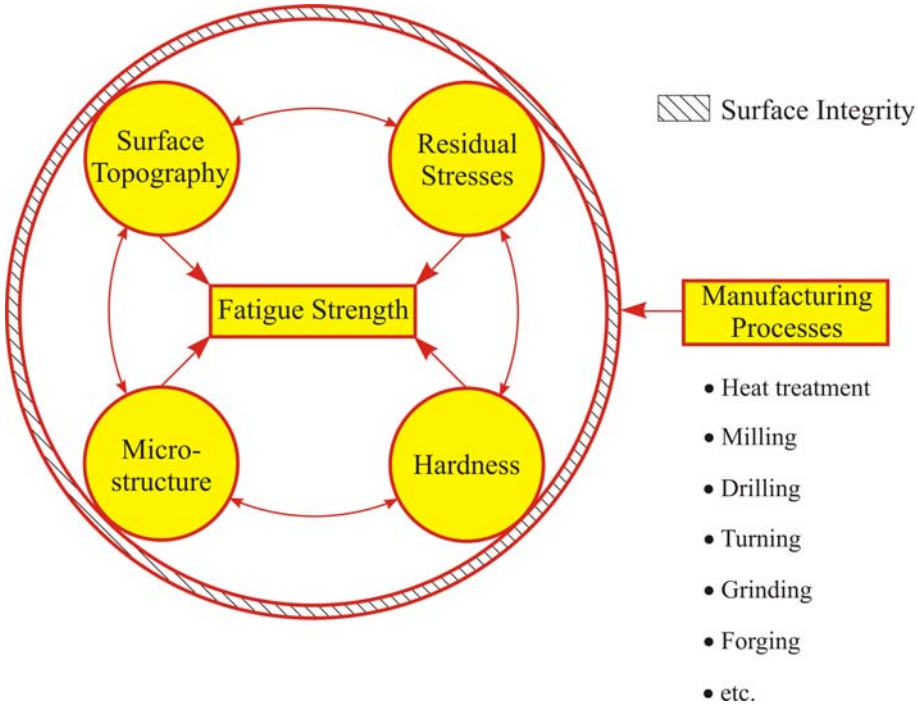

Figure 2.1: Schematic illustration of surface integrity and its effect on fatigue strength.

Manufacturing processes induce many possible alterations in the surface layer of mechanical components which have important influence on their practical properties, especially on their resistance to failures initiated from the surface, such as fatigue and stress corrosion cracking, Figure 2.2.

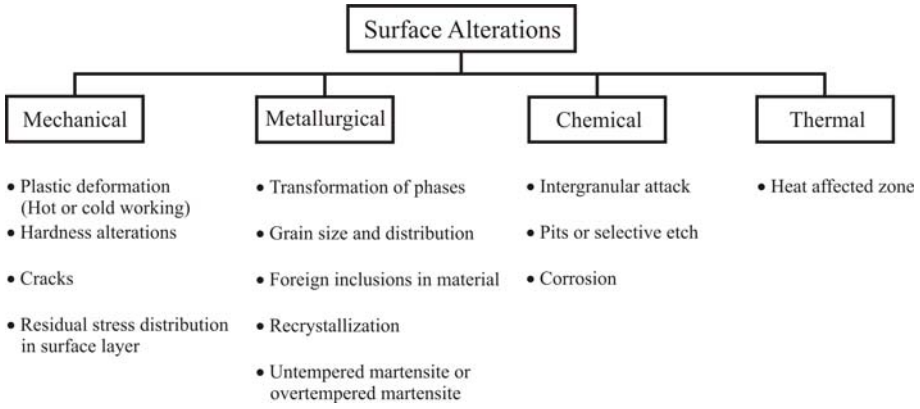

Figure 2.2: Types of surface alterations associated with metal removal practices [3].

Since the influence of manufacturing processes on the surface integrity is very important for the control of workpiece quality, therefore it is necessary to gain better understanding how the finishing processes affect the functional behavior of the machined parts. The functional behavior of a machined component is considerably determined by the physical state of its surface integrity. The surface integrity obtained in machining depends strongly on the employed process parameters. There are various cutting parameters that are known to have a large impact on the surface quality of the machined parts. Therefore, a great deal of research has been performed in order to quantify the effect of various turning process parameters to improve the surface quality. These parameters are classified into three types: set-up parameters, tool parameters and workpiece parameters, Figure 2.3.

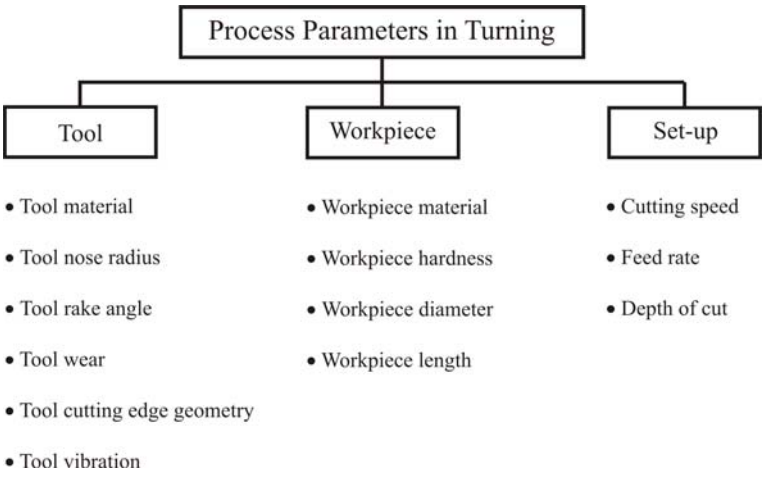

Figure 2.3: List of process parameters in turning.

Figure 2.4 illustrates the main process parameters in turning operation.

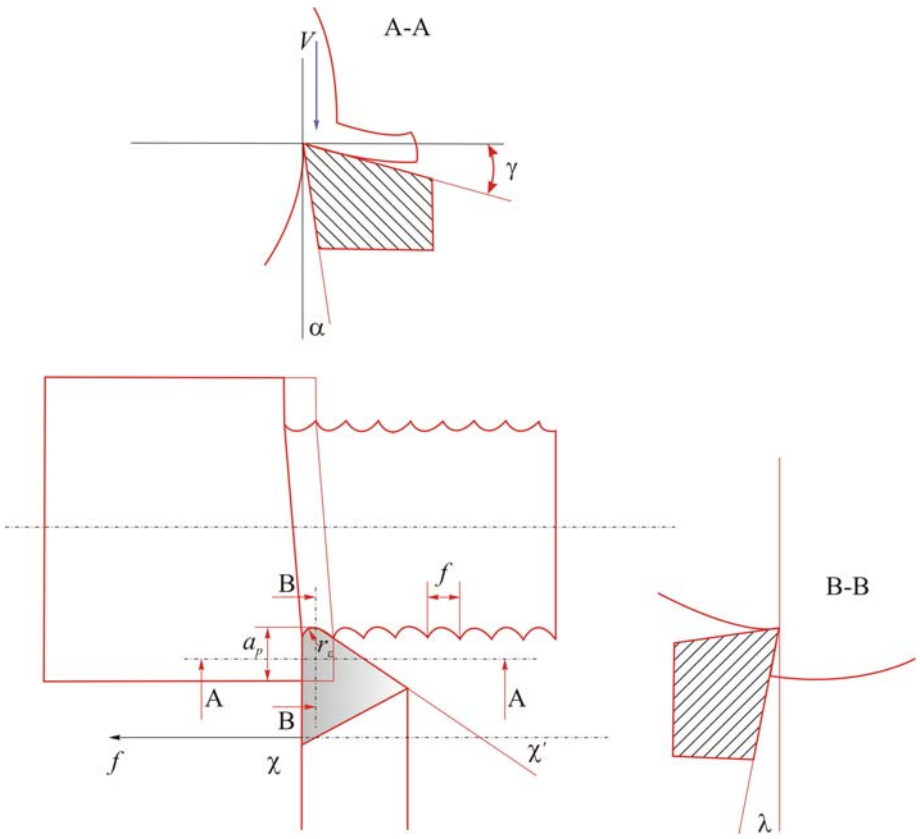

Figure 2.4: Main process parameters in turning [4].

where f, r_ε, d and χ are feed rate, tool nose radius, depth of cut and the entrance angle, respectively. χ', λ and α point out to the exit angle, side relief angle and the back rake angle.

It is well known that the quality of the surface plays a very important role in the performance of machined parts. A good-quality machined surface significantly improves fatigue strength, corrosion resistance or creep life. Thus, it is necessary to know how to control the machining parameters to produce a fine surface quality for the mechanical structures. The criteria of the surface quality are appraised for properties such as surface roughness, residual stresses, hardness variations, structural changes, etc. Hence, many investigations are needed to quantify the properties of the surface integrity caused by the machining parameters [5].

3. Topography of Surfaces

Most surfaces have regular and irregular spacings that tend to form a pattern or texture on the surface. This surface texture is generated by a combination of various factors that are due either to the manufacturing process or the material being finished. The topography of a surface is made up of a combination of three features: surface roughness, surface waviness and surface form. Surface roughness refers to the high-frequency irregularities on the surface caused by the interaction of the material microstructure and the cutting tool action. Surface waviness refers to the medium-frequency irregularities on the surface on which the surface roughness is superimposed. These forms can be caused by the instability of the cutting tool and errors in the machine tool guideway. Surface form is the general shape of the surface, neglecting roughness and waviness, which are caused principally by errors in the machine tool guideway, and deformations due to stress patterns in the component. Figure 3.1 shows the roughness and waviness components of an arbitrary surface [6].

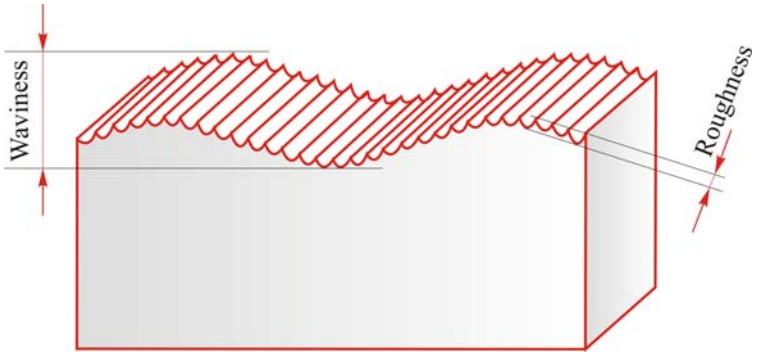

Figure 3.1: Illustration of the roughness and waviness and general form of a surface [7].

3.1. Measuring Surface Roughness

The most common type of contact method for measuring surface topography is the surface texture recorder. The principle of this method is shown in Figure 3.2.

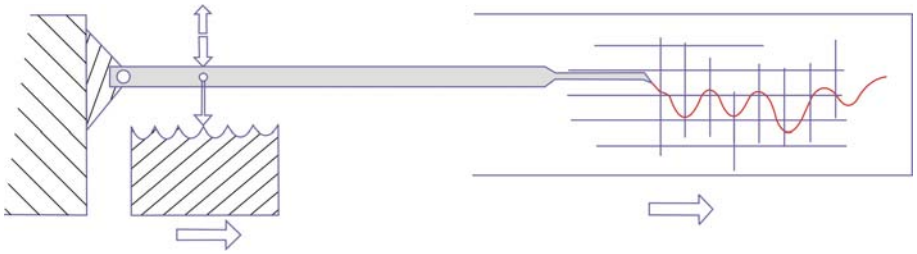

Figure 3.2: Basic principle of a surface texture recorder [6].

The stylus of the instrument is moved across the surface via a guiding mechanism to produce the traced profile, which is defined by the interaction of the stylus with the component. The transducer produces a signal that is the difference between the traced profile and a reference profile or datum profile provided by the guideway. The transducer signal is then converted into a digital signal via an analog-to-digital converter. At this point the transducer contains only the vertical or Z-component of the profile. The horizontal or X-component generated by the traversing mechanism is combined with the Z-component to produce the total profile. The total profile is then filtered to remove unnecessary information, which produces a primary profile. This profile can then be subjected to filtering techniques that can separate the roughness, waviness and form features of the surface [6].

Noncontact techniques are becoming increasingly popular in the measurement of surface topography, especially for surfaces that may be subject to damage using contact techniques. The results obtained are very similar to those of stylus methods and can use the same parameter definitions. Some noncontact methods, such as diffraction measurement, can measure surfaces quickly and easily and can potentially be used on machine tools at the point of manufacture [6].

3.2. Surface Parameter

For effective analysis of surface roughness or waviness, the profile generated by the measuring instrument needs to be evaluated according to mathematical formulas, called surface parameters. The purpose of using a parameter is to apply a number that can characterize a surface [8].The application of different types of surface parameters can best be described by discussing the various types of surfaces generated by finishing methods. One of the most commonly used roughness parameters is the roughness average R_a, which is used to assess the coarseness of the surface such as those produced by grinding, turning and milling

operations. The parameter R_a is defined as the mean height of the roughness profile Figure 3.3.

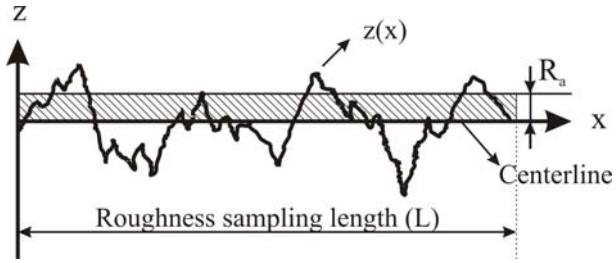

Figure 3.3: Arithmetical average roughness, R_a.

Eq. (3.1) shows the definition of parameter R_a.

$$R_a = \frac{1}{L}\int_0^L \left|z(x)\right| dx \qquad \text{Eq. (3.1)}$$

Another averaging parameter, R_q, takes the root mean square of the profile and is more sensitive to surface variations Eq. (3.2).

$$R_q = \left(\frac{1}{L}\int_0^L z(x)^2 dx\right)^{\frac{1}{2}} \qquad \text{Eq. (3.2)}$$

For some surfaces it is sometimes desirable to specify the maximum roughness height, R_{max}, or the peak-to-valley height, R_z, rather than use the mean height given by R_a. The R_{max} parameter measures the highest and lowest points of the profile and is particularly valuable where components are subjected to high stresses. Any large peak-to-valley heights may be areas likely to suffer from crack propagation. However, because R_z is very susceptible to dirt or scratches, it is an unstable parameter [8]. A schematic description of the R_{max} parameter for an arbitrary machined surface is shown in Figure 3.4.

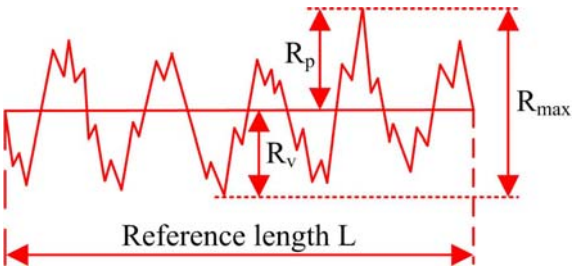

Figure 3.4: Schematic illustration of R_{max}.

3.3. Effect of Turning Process Parameters on Surface Roughness

The machining or finishing process has the greatest impact on the geometry of the surface. A major factor is the action of the cutting tool on the material. Elements such as tool shape, cutting speed, feed rate, depth of cut and cutting fluid can be varied to affect the surface topography. Other factors affecting the surface are the instability of the cutting tool and errors in the machine tool guideway [6].

Several researches have studied the effect of cutting parameters on surface roughness in turning operations. Thiele and Melkote [9] showed that an increase in edge hone radius increase the average surface roughness because of increase in the ploughing component compared to the shearing component of deformation. Chou and Evans [10-11] showed that the surface roughness tend to increase when the tool wear increases.

Many attempts have been made to model surface roughness in hard turning as a function of various process parameters. Whitehouse [12] proposed an empirical model to estimate the surface roughness variation, Eq. (3.3).

$$R_a = \frac{f^2}{32 \cdot r_\varepsilon} \qquad \text{Eq. (3.3)}$$

This relationship only takes into account the geometric part of roughness. The real surface finish is a combination of the geometric roughness and the secondary roughness derived from the plastic flow of the material, the removal process, tool wear, tool or workpiece chatter, etc. This implies that the agreement between the measured roughness and the values predicted according to Eq. (3.3) is fairly good only for medium-high levels of R_a. For low levels of roughness the model systematically under-estimates the real surface roughness, because in this case secondary roughness becomes more significant than geometric roughness [13].

Sasahara [14] investigated the effect of tool nose r_ε radius, feed rate f and two kinds of tool edges, sharp and chamfered (Figure 3.5) on the surface roughness of a 0.45%C steel.

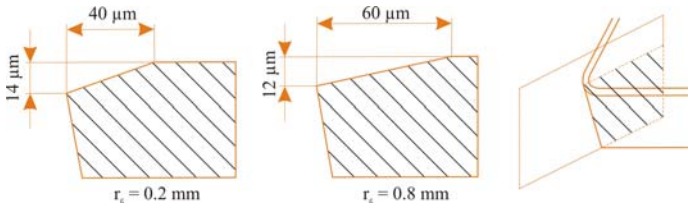

Figure 3.5: Tool edge configuration with chamfer [14].

Figure 3.6 shows the correlation between surface roughness and cutting conditions in feed direction.

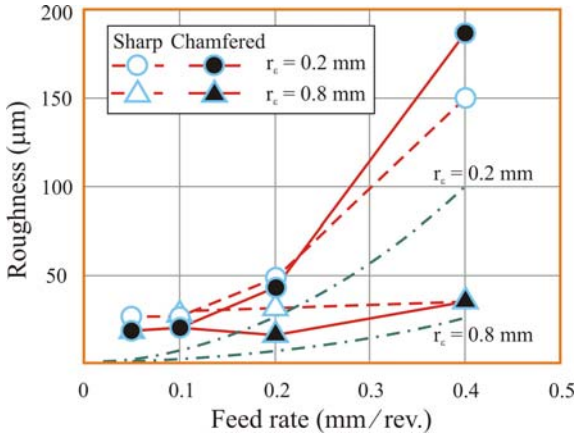

Figure 3.6: Effect of cutting conditions on surface roughness [14].

It can be seen that the surface roughness increases when the feed rate increases, where the tool nose radius becomes smaller.

4. Residual Stresses

Residual stresses in a machined surface are one of the decisive factors in determining surface quality. They are defined as the locked-in stresses that exist in a machine part after all the external loads are removed. Due to their nature, the residual stresses are in equilibrium (self-balance) [15].

Manufacturing processes are the most common causes of residual stresses. Virtually all manufacturing and fabricating processes such as casting, welding, machining, molding, heat treatment, etc. introduce residual stresses into the manufactured object. The effects of residual stresses may be either beneficial or detrimental, depending upon the magnitude, sign, and distribution of the stress with respect to the load-induced stresses. In general, the residual stresses are detrimental, and there are many documented cases in which these stresses were the predominant factor contributing to fatigue and other structural failures when the service stresses were superimposed on the already present residual stresses [16].

4.1. Classification

Macherauch and Kloss [17] proposed a classification of the residual stresses into three orders or types, related to the scale on which one considers the material. Residual stresses of the first order, or type I residual stresses, are homogeneous over a very large number of crystal domains of the material. Such stresses are also termed macrostresses, σ_{RS}^{I}. The internal forces related to this stress are balanced on all planes. The moments related to these forces are equal to zero around all axes. Residual stresses of the second order, or type II residual stresses, are homogeneous within small crystal domains of the material (a single grain or phase). The internal forces related to these stresses are in balance between the different grains or phases. Residual stresses of the third order, or type III residual stresses, are homogeneous on the smallest crystal domains of the material (over a few interatomic distances). The internal forces coupled to these stresses are in balance in very small domains (such as around dislocations or point defects). Type II and III residual stresses are collectively termed microstresses σ_{RS}^{II} and σ_{RS}^{III}. In the case of real materials, the actual residual stress state at a point comes from the superposition of stresses of type I, II and III stresses, as is illustrated in Figure 4.1, [18].

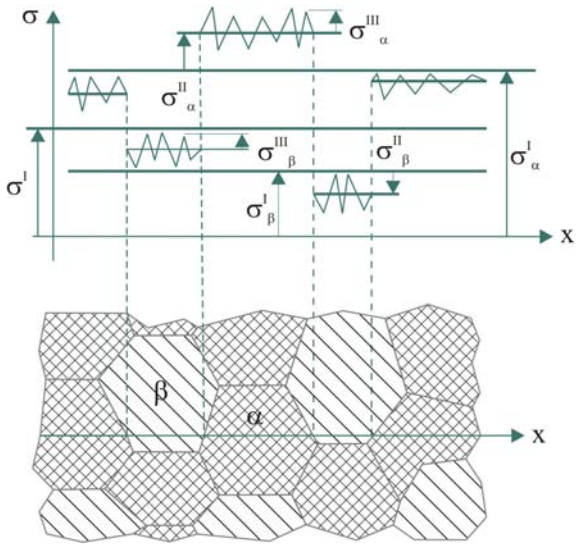

Figure 4.1: Three orders of stresses in two-phase materials [18].

4.2. Origin of Residual Stresses

The creation of residual stresses is caused by elastic-plastic deformation, which takes place in the contact area between the tool and workpiece and is aided sometimes by high temperatures [19]. Tricard [20] explained how residual stresses are generated during a grinding operation, Figure 4.2.

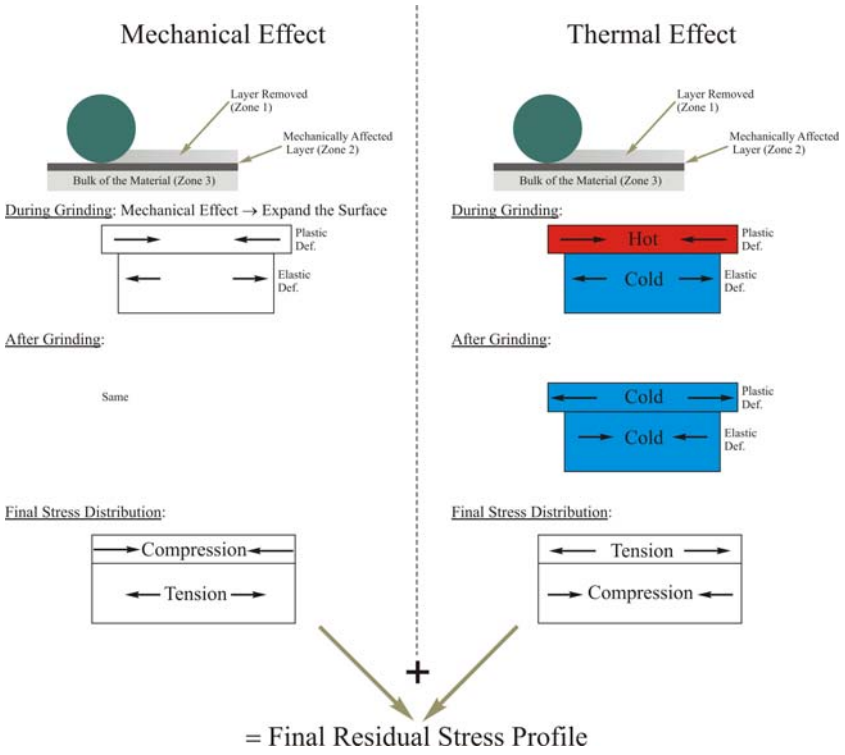

Figure 4.2: Mechanism of residual stress generation during grinding [20].

Figure 4.2 illustrates the mechanism of residual stress generation in ground components by the superimposition of a mechanical (left) and a thermal (right) effect. For the process shown on the left, three distinct zones can be distinguished: zone 1 is the surface layer being ground, zone 2 is the mechanically affected zone immediately underneath zone 1 and zone 3 is the remaining bulk of the material. During grinding, zone 2 experiences an increase in length, which is constrained by the unaffected zone 3. The plastically deformed surface (zone 2) is therefore left in a state of compression, while the bulk of the material (zone 3) is in slight tension. For the process shown on the right, zone 2 is the heat-affected zone at the surface of the material. During grinding, the heated surface (zone 2) expands in length, but once again is constrained by the bulk of the material (zone 3), which remains at room temperature, leaving the surface in a state of compression. The workpiece begins to cool immediately after grinding, reversing the distribution and resulting in a surface layer in tension and the bulk of the part in slight compression. As shown in Figure 4.2, the resulting value of the residual stress induced during the grinding operation is the superimposition of these two phenomena.

Gunnberg et. al. [21] described how turning influences the generation of the residual stress level when the cutting tool slides across the workpiece, Figure 4.3.

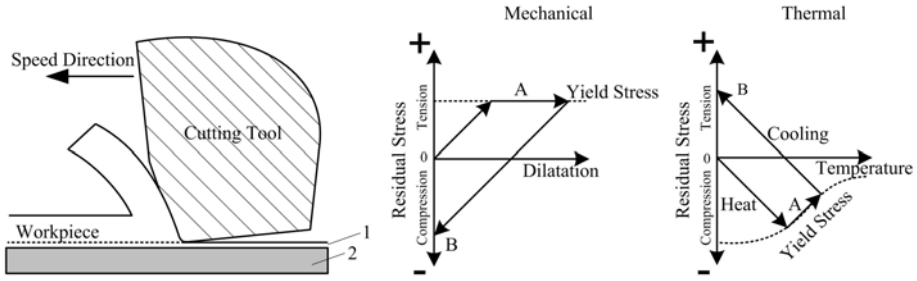

Figure 4.3: Generation of residual stress by turning [21].

The mechanism of mechanically generated residual stress during cutting (A) can be explained by a plastic deformation in the surface layer (1) and elastic deformation in the underlying surface layer (2). To achieve force equilibrium and geometric compatibility after the cutting processes, the elastic dilatation places the surface layer in residual compressive stress (B). The thermal residual stress mechanism is due to the heat of the cutting process, which expands the surface layer and produces compressive stress (A). The workpiece is then cooled (B) and contractions in the surface layer (1) produce tension residual stress. The thermal

effect decreases further inside the workpiece, thus the main consequence of tension stress is on the surface.

4.3. Measurement of Residual Stresses

Over the last few years, it has been a continuing interest in developing methods for measuring residual stresses. The materials scientist and the engineer can now access a large number of residual stress measurement techniques. Some are destructive, while others can be used without significantly altering the component, some have excellent spatial resolution, whereas others are restricted to near surface stresses or to specific classes of material [22]. Among the different methods developed for this purpose, the hole-drilling and X-ray diffraction are widely employed for the quantitative residual stress analysis and are described in detail in the following.

4.3.1. Hole-Drilling Method

One of the popular and widely used techniques for measuring residual stresses is the hole-drilling method. A typical application of the hole-drilling method involves drilling a small shallow hole in the specimen. This removal of stressed material causes localized stress and strain relaxations around the hole location. The strain relaxations are measured using a specially designed strain gauge rosette [23]. Figure 4.4 shows the arrangement of the strain gauge rosette with three elements and the preferred notation for the direction of the principal stresses, σ_{max} and σ_{min}.

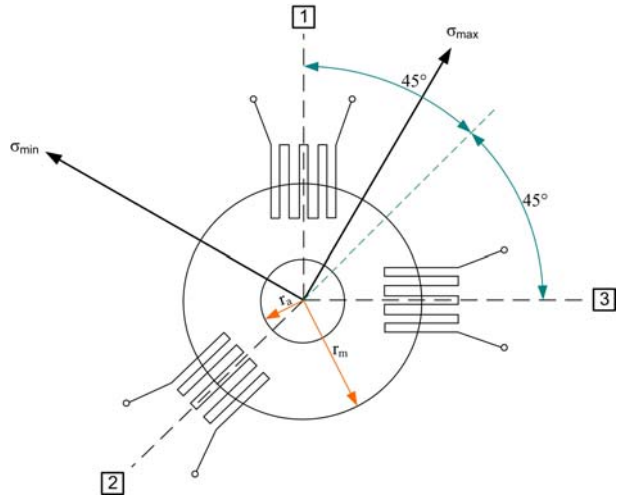

Figure 4.4: Strain gauge rosette arrangement for measuring residual stresses.

In this design the three radially oriented gauges are arranged with their centers from the gauge target and the center of the hole. Although, in theory, the angles between the gauges can be chosen arbitrarily, the simplest analytical calculations are achieved with 45°, and this is now the standard for most commercially available designs. r_a and r_m are the hole radius and mean gauge circle radius, respectively [24]. The recorded strains are converted to stress using equations that have calibration coefficients determined by test.

Standard hole-drilling is a method, frequently used to evaluate in-plane residual stresses that can be assumed to be uniform with depth below the surface. However, in many practical cases, the residual stresses are not uniform. In such cases, the assumption of uniform stress with depth may give a misleading solution [25]. There are four calculation procedures available to determine non-uniform residual stress fields using incremental strain relaxation data from the hole-drilling method, which are described in the following.

4.3.1.1. Incremental Strain Method

The incremental strain method for estimating non-uniform residual stresses was first introduced by Soete and Van Crombrugge [26] and further developed by Kelsey [27]. The experimental procedure is similar to that for traditional hole-drilling. However, the incremental strain method has a significant theoretical shortcoming. The assumption that the incremental strain relaxation measured after making an increment in hole depth are wholly due to the stresses within that depth increment is not valid. The relaxed strain, measured at the surface subsequent to the drilling of an increment, is partly due to the stresses released in the increment and partly due to the previously released stresses which yields a modified response as the geometry is changed. For this reason, strain relaxation can continue to grow, even when the new hole depth increment is totally unstressed [28-30].

4.3.1.2. Average Stress Method

In order to overcome the theoretical shortcomings of the incremental strain method, Nickola [31] introduced a new stress calculation method using the concept of equivalent uniform stress. The equivalent uniform stress is defined as that stress magnitude within the total hole depth which produce the same total strain relaxations as the actual non-uniform stress distribution. With the average stress method, the equivalent uniform stress is calculated using the strain relaxations measured before and after each hole depth increment.

The average stress method, however, also has a significant shortcoming. It is assumed that the equivalent uniform stress equals the average stress over the hole depth. In practice the stresses in the material closer to the surface contribute much more to the surface strain relaxations that do the stress further from the surface. The need to use experimental calibration data has also limited the theoretical scope of this calculation procedure, which has recently been identified [28-30, 32].

4.3.1.3. Power Series Method

The Power Series Method proposed by Schajer [29] is an approximate, but theoretically acceptable method to calculate non-uniform stress fields from incremental strain data. It provides a limited amount of spatial resolution by assuming that the residual stresses vary linearly with depth from specimen surface. Finite element calculations are used to compute series of coefficients corresponding to the strain responses measured during hole-drilling.

An advantage of this method is that the least square procedure forms a best fit curve through the measured strain data. However, a limitation of the power series method is that it is suitable only for smoothly varying stress fields [23, 25].

4.3.1.4. Integral Method

In the integral method, the contributions of the total measured strain relaxations at all depths are considered simultaneously. This provides a separate evaluation of residual stress within each increment of depth. Thus, the spatial resolution is the highest of all the calculation methods and is the method of choice when measuring rapidly varying residual stresses. However, the stress calculation inaccuracy increases quickly with the number of hole depth increments used in the calculation. In practice, five or six increments yield a satisfactory level of detail for many stress distributions [25].

Figure 4.5 shows a comparison of the results of four stress calculation methods for a non-uniform stress field.

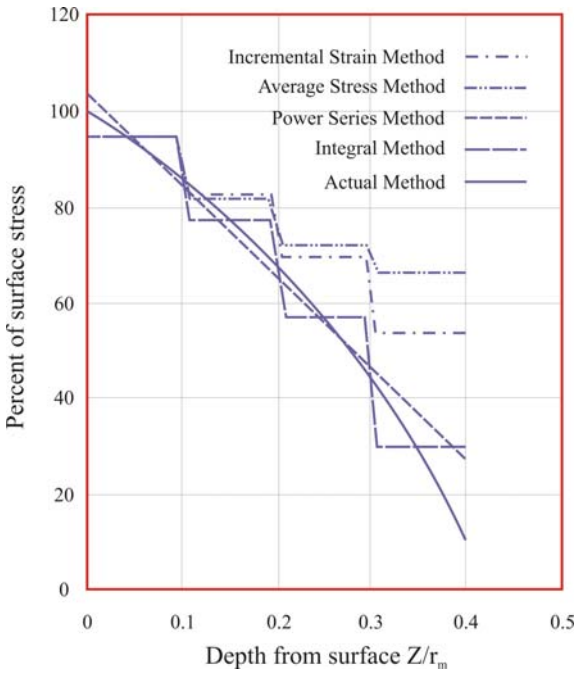

Figure 4.5: Comparisons of the results from the four stress calculation methods [23].

It can be seen that the integral method gives a good stepped approximation to the actual stress variation with depth while the power series method gives a close straight-line fit. The incremental strain and the average stress methods give much less satisfactory results because they are essentially calibrated using uniform stress field data.

In the present work, the integral method has been chosen as it offers flexibility regarding the stress variation. This method is briefly described in the following.

As a hole is drilled to a certain depth z, the residual stresses released at every intermediate depth Z, between the surface and the depth z, contribute to the relaxed strain measured at the surface. Figure 4.6 illustrates the hole depth z, stress depth Z, hole radius r_a and mean gauge circle radius r_m.

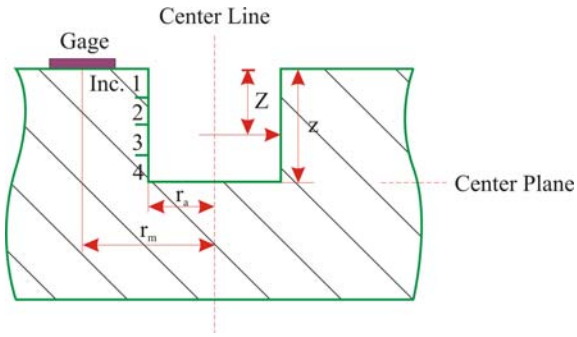

Figure 4.6: Definition of hole depth z and stress depth Z [35].

The relaxed strain contribution from the residual stress release at the depth *Z* is dependent on the actual hole depth *z*. This is described as the geometrical effect and is taken into account by the integral method. This means that the relaxed strain, measured at the surface subsequent to the drilling of an increment, is partly due to the stresses released in the increment and partly due to the previously released stresses, which yields a modified response as the geometry is changed [35]. The two contributions are illustrated in Figure 4.7.

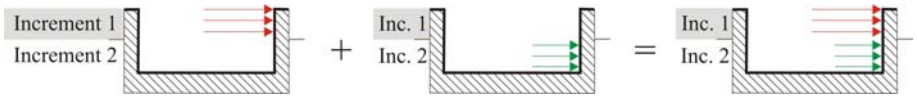

Figure 4.7: Geometrical contribution to the relieved strain in drilling of the second increment [35].

Some simplification can be achieved with the hole radius and depth dependencies. It is desirable to normalize the depth dimensions with respect to the mean radius of the strain gauge rosette, r_m. The normalized depths $H = Z/r_m$ and $h = z/r_m$ are called non-dimensional depth from surface and non-dimensional hole depth, respectively.

Assuming that the stress field $\sigma(H)$ is equal biaxial, i.e., at any given depth from the surface, the stresses are the same in all directions parallel to the surface [23]. The measured strain relaxation $\varepsilon(h)$, due to drilling a hole of depth h, is the integral of the infinitesimal strain relaxation components from the stresses at all depths in the range $0 \leq H \leq h$, Eq. (4.1).

$$\varepsilon(h) = \frac{1+\nu}{E} \int_0^h A(H,h)\,\sigma(H)\,d(H) \quad 0 \leq H \leq h \qquad \text{Eq. (4.1)}$$

where $A(H, h)$ is the strain relaxation per unit depth caused by a unit stress at depth H, when the hole depth is h. The term $(1+\nu)/E$ describes the dependence of the strain relaxations on material properties.

In practice, the strain relaxation response $\varepsilon(h)$ is not continuously determined. Only values at n discrete points are known. In this case, an approximate solution can be achieved using a discrete form of equation Eq. (4.2).

$$\sum_{j=1}^{j=i} a_{ij}\,\sigma_j = \frac{E}{1+\nu}\,\varepsilon_i \qquad 1 \le j \le i \le n \qquad \text{Eq. (4.2)}$$

where ε_i, σ_j, a_{ij} and n are the total strain relaxation after the i^{th} increment is drilled, equivalent uniform stress within the j^{th} hole depth increment, strain relaxation due to a unit stress within increment j of a hole i increments deep and total number of hole depth increments, respectively. It should be noted that index i refers to the number of increments drilled, whereas j refers to the increment in which the stress is acting.

The relationship between the coefficient a_{ij} and the strain relaxation function $A(H, h)$ is given by Eq. (4.3).

$$a_{ij} = \int_{H_{j-1}}^{H_j} A\left(H, h_i\right) dH \qquad \text{Eq. (4.3)}$$

In matrix notation, Eq. (4.2) becomes

$$a \cdot \sigma = \frac{E \cdot \varepsilon}{\left(1+\nu\right)} \qquad \text{Eq. (4.4)}$$

The discrete strain relaxation matrix a is lower triangular. If the matrix coefficients a_{ij} are known, a stepwise approximate solution for the stress variation with depth can be found by solving Eq. (4.4).

Figure 4.8 illustrates the physical interpretation of the coefficients a_{ij} of matrix a. The columns of the matrix correspond to the strain relaxations caused by the stresses within a fixed increment, for holes of increasing depth.

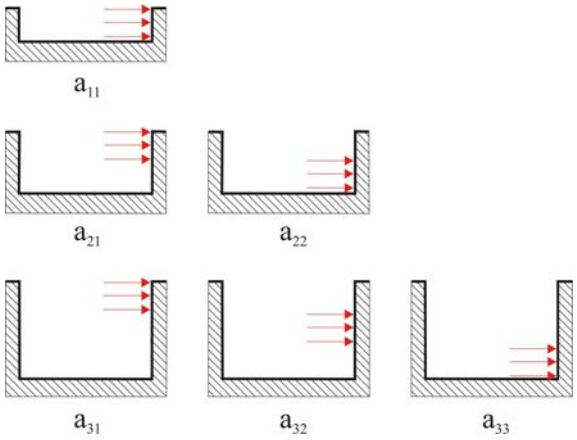

Figure 4.8: Stress loadings corresponding to the coefficients a_{ij} of matrix a.

For conceptual simplicity, the discussion so far has been limited to a simple equal biaxial stress field. The in-plane stresses at a given depth were the same in all directions, and the three measured relaxed strains were all equal. For the general case, the three stress components σ_1, σ_3 and τ_{13} and the three strains ε_1, ε_2 and ε_3 vary independently throughout the hole depth. For calculations with such general non-uniform stress fields, it is mathematically convenient to work in terms of transformed stress and strain variables. This decouples the stress/strain equations and simplifies their mathematical structure. The Cartesian stress components acting at depth H in a plane parallel to the specimen surface are described in terms of transformed stress variables, Eq. (4.5).

$$\begin{aligned} P(H) &= (\sigma_3(H) + \sigma_1(H))/2 \\ Q(H) &= (\sigma_3(H) - \sigma_1(H))/2 \\ T(H) &= \tau_{13}(H) \end{aligned} \qquad \text{Eq. (4.5)}$$

Similarly, the three strain relaxations measured after the hole reaches a depth h are expressed in terms of transformed strain variables, Eq. (4.6).

$$\begin{aligned} p(h) &= (\varepsilon_3(h) + \varepsilon_1(h))/2 \\ q(h) &= (\varepsilon_3(h) - \varepsilon_1(h))/2 \\ t(h) &= (\varepsilon_3(h) + \varepsilon_1(h) - 2\varepsilon_2(h))/2 \end{aligned} \qquad \text{Eq. (4.6)}$$

In matrix notation, Eq. (4.2) and similar equations for the other two transformed stresses become

$$\begin{aligned} a \cdot P &= E \cdot p/(1+\nu) \\ b \cdot Q &= E \cdot q \\ b \cdot T &= E \cdot t \end{aligned} \qquad \text{Eq. (4.7)}$$

The Cartesian stress components for each increment can be recovered from the calculated transformed stresses using Eq. (4.8).

$$\begin{aligned} \sigma_1(H) &= P(H) - Q(H) \\ \sigma_3(H) &= P(H) + Q(H) \\ \tau_{13}(H) &= T(H) \end{aligned} \qquad \text{Eq. (4.8)}$$

Finally, the principal stresses can be evaluated very compactly in terms of the transformed stresses or strains, Eq. (4.9).

$$\sigma_{\max}(H), \sigma_{\min}(H) = P(H) \pm \sqrt{Q^2(H) + T^2(H)} \qquad \text{Eq. (4.9)}$$

A detailed description of the integral method can be found in Schajer [23, 33] and Andersen [34].

4.3.2. X-ray Diffraction Method

X-ray methods have been used widely for measuring residual stresses in crystalline materials. This method is a non-destructive technique based on the evaluation of interplanar distances in deformed samples along different orientations. However, in order to obtain stress depth information, it has to be combined with layer removal methods. The sample size is also limited, and therefore, it is difficult to analyze residual stresses in real machine parts. Usually the measurements are made manually on a conventional powder X-ray diffractometer or with a special unit. X-rays penetrate typically less than 20 μm into the material and the method is therefore restricted to determination of residual stresses at the immediate surface of the

specimen [36]. Figure 4.9 shows a schematic illustration of X-ray diffractometer using a single wavelength λ.

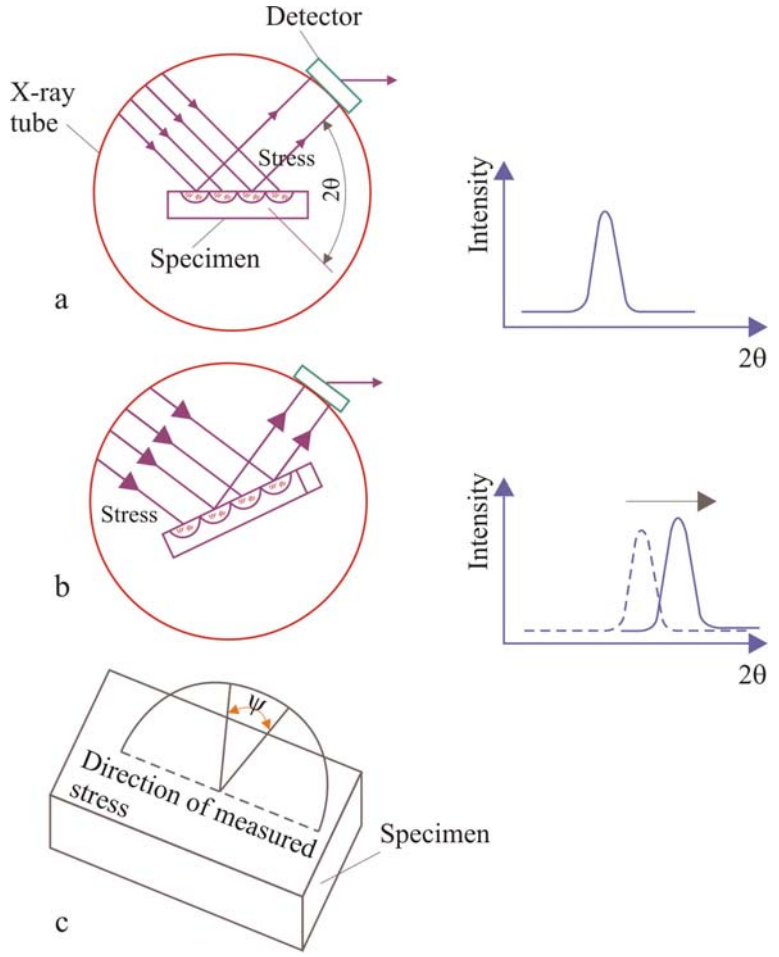

Figure 4.9: Diffracting grains in a polycrystalline specimen at (a) $\psi = 0$, (b) $\psi = \psi$, during a stress measurement, (c) direction of measured stress [36].

With reference to Figure 4.9, assume that X-ray detector is moved over a range of angles, 2θ, to find the angle θ, of the diffraction from grains that satisfies Bragg's law $n \cdot \lambda = 2 \cdot d \cdot \sin\theta$. In this law n represents the class of diffraction, λ is the wavelength of the incident radiation, d_{hkl} is the interplanar spacing of a lattice plane, described by the Miller indices h, k and l and θ is the diffraction angle. Grains that have planes with this spacing which are parallel to the surface will diffract as shown in Figure 4.9a. The d spacing is obtained from the peak in intensity versus scattering angle 2θ and Bragg's law $\lambda = 2 \cdot d \cdot \sin\theta$ [37-38]. If the surface of the specimen is in compression, the d spacing of these planes are further apart than in the stress-free state due to the Poisson's effect. After the specimen is tilted with respect to the incoming

beam (Figure 4.9b), new grains diffract and the orientation of the diffraction planes is more nearly perpendicular to the stress direction. The result is that, with the tilt, the *d* spacing decreases and the angle 2θ increases. As shown in Figure 4.9c, the stress is measured in a direction which is the intersection of the circle of tilt and the surface of the specimen. In effect, the interplanar spacing acts as an internal strain gauge. Since the spacing of lattice planes (the strain gauges) is extremely small they will be affected by both micro and macro stresses. The X-ray method measures the sum of these stresses. The fact that X-rays penetrate only a shallow depth is useful, because in many cases there are steep gradients in the macrostress near the surface [36].

Within this work, X-ray residual stress analysis was carried out using an XSTRESS 3000 analyzer emitting CrKα at 200 W. By assuming that the out-of-plane stress is zero and that the stress state in the analyzed sampling volume is homogenous, the so-called $sin^2\psi$ method [39] was used to determine the stress from the experimental strain value. In this model, Young modulus and Poisson ration are the only necessary constants. According to the $sin^2\psi$ method the stress value σ_ϕ in the plane of the sample surface is defined as, Eq. (4.10) [36]:

$$\varepsilon_{\phi\psi} = \frac{1}{2} S_2 \sigma_{\phi\psi} \sin^2\psi + S_1(\sigma_1 + \sigma_2) \qquad \text{Eq. (4.10)}$$

where $\varepsilon_{\phi\psi}$ is the strain measured in the direction defined by the tilting angle ψ and rotating angle ϕ with respect to the incident beam. The largest and smallest principal macroscopic stresses in the plane are designated by σ_1 and σ_2, whereas $\sigma_{\phi\psi}$ is the stress in the measurement direction. The X-ray elastic constants S_1 and S_2 are mainly dependent on the crystallographic texture, which is an important microstructural parameter in polycrystalline samples, describing the distribution of the crystal lattice orientation.

4.4. Effect of Turning Process Parameters on Residual Stresses

Different processing methods show different effects on the character of residual stresses. The effects occur as a result of a combined action of several causes. Either the character or the magnitude of residual stresses induced in the surface layer can be changed by altering processing conditions [19].

Several researches have investigated the effect of process parameters on residual stresses in turning operations. Thiele and Melkote [9] have shown that cutting edge geometry have a large impact on the stress levels generated in finish hard turning. They reported that increased edge hone radius on the insert generated higher cutting forces. A higher passive force tangential to the surface generates higher compressive residual stresses. Dahlman et. al. [40] studied the influence of rake angle, cutting feed and cutting depth on residual stresses in hard turning. They showed that a greater negative rake angle induces higher compressive residual stresses as well as a deeper affected zone below the surface. The maximum stress position is moved further into the material using increase rake angles. They also demonstrated that the cutting depth does not affect residual stresses and an increased feed rate generates significantly higher compressive residual stresses.

Figure 4.10 shows the residual stress distribution affected by different feed rates according to [41].

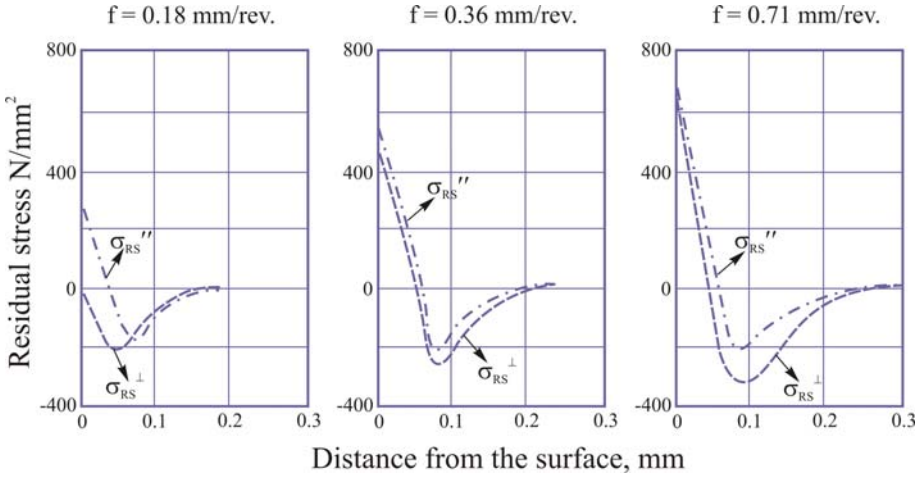

Figure 4.10: Residual stresses in the parallel (dash-dotted line) and transverse (dashed line) directions caused by turning of SAE 1045 for different cutting feeds. The cutting speed is 90 m/s and no cooling [41].

It can be seen that the higher the feed rate is, the higher the induced residual stresses either at the surface or beneath the surface is. Figure 4.10 also illustrates that the tensile stresses often appear near the surface and compressive stresses occur deeper into the material. The stress distribution is affected by friction in the cutting process, which tends to cause tensile stresses in the surface near layer and by plastic deformation, which causes compressive stresses in the deeper layers.

Leskovar et. al. [42] investigated the effect of feed rate *f*, cutting speed v_c and tool wear *VB* on the residual stresses, Figure 4.11.

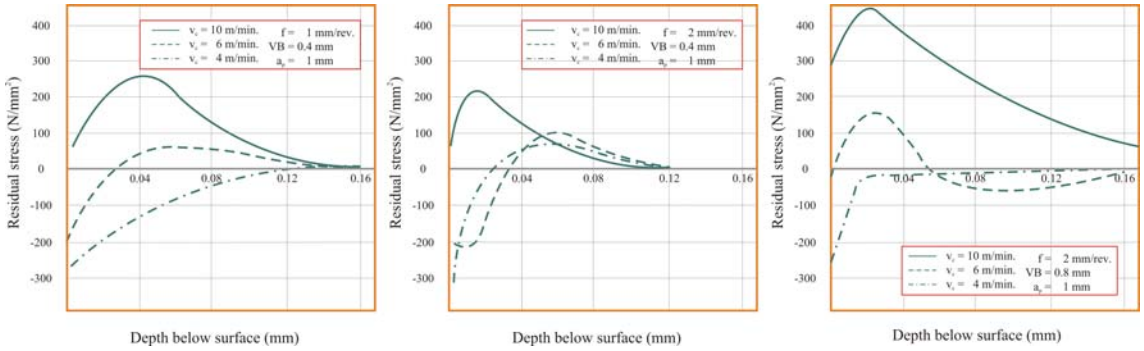

Figure 4.11: Residual stresses of turned specimens [42].

Figure 4.11 shows that turning generates residual stresses of great intensity in the layers directly underneath the surface, particularly at high cutting speeds. With the increased wear VB the residual stresses increase, too, reaching even deeper into the layers underneath the surface. These stresses accelerate the occurrence and diffusion of microcracks.

5. Hardness

Mechanical properties are based on the bonding characterizations and the microstructure of a material. Careful examination of the mechanical behavior of materials can give information on the lattice imperfections and atomic defects. In some branches of industry the common mechanical tests, such as tensile, hardness, creep and fatigue tests, may be used, not to study the defect state but to check the quality of the product against a standard specification [43].

The hardness of a metal, defined as the resistance to penetration, gives a conveniently rapid indication of its deformation behavior. There are different definitions of hardness depending on the subject area, which can be found in literature. However, all definitions have in common, that the material is subject of plastic deformation.

Various methods of indentation were developed over the last decades, where the most important ones were defined by Vickers, Knoop, Brinell and Rockwell [44]. All of them relate the applied load to a geometrical feature of the remaining imprint produced by indenters of different shape and geometry. The hardness may be related to the yield or tensile strength of the metal, since during the indentation, the material around the impression is plastically deformed to a certain percentage strain. The residual imprint in the tested material due to plastic deformation is evaluated in size by optical microscope after removal of the load [43]. The Vickers diamond indenter is ground in the form of a squared pyramid with an angle of 136° between faces. The Knoop indenter is a diamond ground to pyramidal form that produces a diamond shaped indentation having approximate ratio between long and short diagonals of 7:1. Brinell uses a steel ball as indenter and Rockwell a steel ball or a diamond cone.

5.1. Evaluation of Hardness

One of the methods for hardness measurement is called depth sensing indentation where force and depth of a loading and unloading indentation cycle are recorded. A schematic illustration of such an indentation is shown in Figure 5.1 with a corresponding load-displacement curve. In general the probed volume is small, why it can be ranked as a non-destructive investigation technique. On the other hand it is necessary to evaluate several indents to obtain a statistical representative hardness value of the material. The most common evaluation method of the load-displacement curves, also used in this work, was proposed by

Oliver and Pharr [45]. This technique is standardized in the standard DIN EN ISO 14577 part 1-3 [46]. This has the benefit that no size evaluation of the remaining imprint is necessary since the hardness values are obtained from the evaluation of the unloading segment of the load-displacement curve. As illustrated in Figure 5.1, the hardness is defined as applied load F divided by the corresponding projected contact area A_c. The elasto-plastic behavior of the material causes an indentation depth of h_{max} under maximum load F_{max}, whereas the indenter is only in contact with the material for the depth h_c. After unloading the residual imprint has the depth h_r due to the elastic recovery. The elastic contribution to the maximum displacement is indicated with h_e.[44].

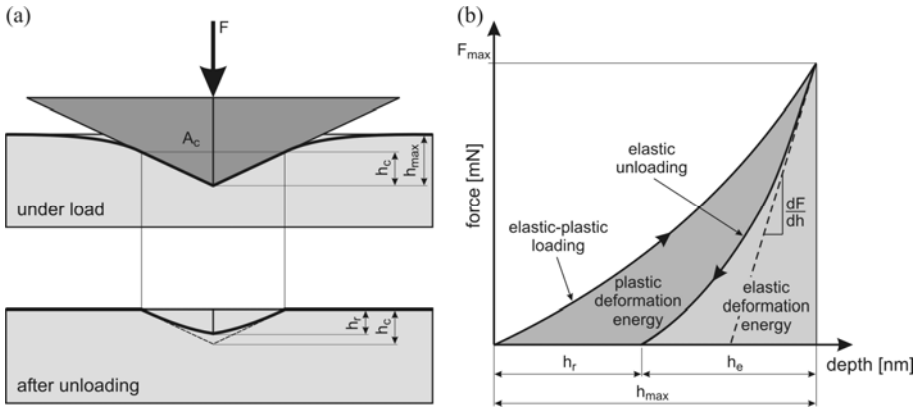

Figure 5.1: a) Schematic illustration of an indentation with a pyramidal indenter under the load F and b) schematic of a corresponding load-displacement curve with the loading and unloading segment [43].

The facility used to determine the hardness of the samples used in this work was a Fischerscope H100C equipped with a Vickers indenter with a continuously load of 100 mN. The device measures the universal hardness according to ISO 14577 [47]. The universal hardness HU is defined as the load F, applied to the indenter divided by the surface of the indent at maximum load. The created area of the indent is calculated from a constant, which is characteristic for the indenter geometry and the indentation depth. HU_{pl} is the plastic universal hardness, that means the elastic part is not considered and the load is correlated with the remaining plastic indent area which is calculated from the depth value h_r [48].

$$HU_{pl} = \frac{F}{26.43 \cdot h_r^{\,2}} \qquad \text{Eq. (5.1)}$$

The factor 26.43 correlates the surface of the indent of a Vickers indenter and the indentation depth.

To determine the hardness within this work, all samples have been polished because of the high roughness. At least 16 indentations were made on each sample resulting in a statistically confirmed average hardness value. Before mathematical evaluation, the recorded loading-unloading curves were checked for irregularities and irregular curves were omitted from statistics.

5.2. Effect of Cutting Parameters on Hardness

Sasahara [14] investigated the effect of tool nose r_ε radius, feed rate f and two kinds of tool edges, sharp and chamfered (Figure 3.5), on the surface hardness of a 0.45%C steel. In general, the hardness distribution along the depth direction caused by cutting is higher as it comes nearer to the surface. He reported that the tool nose radius and the chamfer have an important influence on machined surface hardness and the feed rate does not affect the surface hardness so much Figure 5.2.

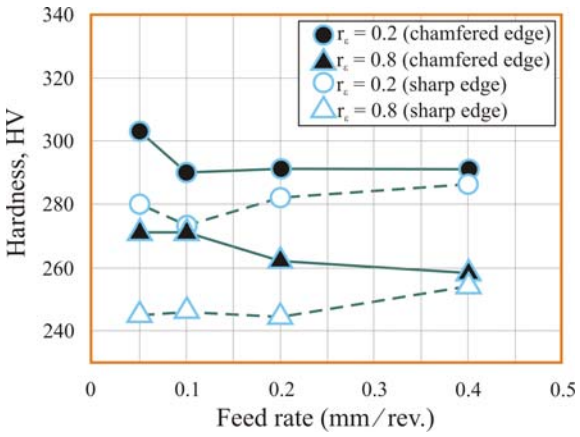

Figure 5.2: Effect of cutting conditions on machined surface hardness [14].

Figure 5.2 shows that the surface hardness becomes higher when a smaller corner radius tool with chamfer is used. That means that the plastic deformation within the machined surface layer becomes greater.

Leskovar et. al. [42] studied the influence of feed rate f and the tool wear VB on the hardness in turning operation. The material employed in this study was Č.4782 according to JUS or 42CrMoS4 according to DIN. The basic material exhibits the hardness HB = 275.

Results reported in this study show that changes of hardness do not occur beyond the depth of 50 µm. The maximum changes of hardness appear directly underneath the generated surface, with the increase in hardness reaching up to 60% in relation to the hardness of the basic material. The wear of the cutting edge affects hardness most, the greatest surface hardening thus occurring when wear is $VB > 0.30$ mm, Figure 5.3.

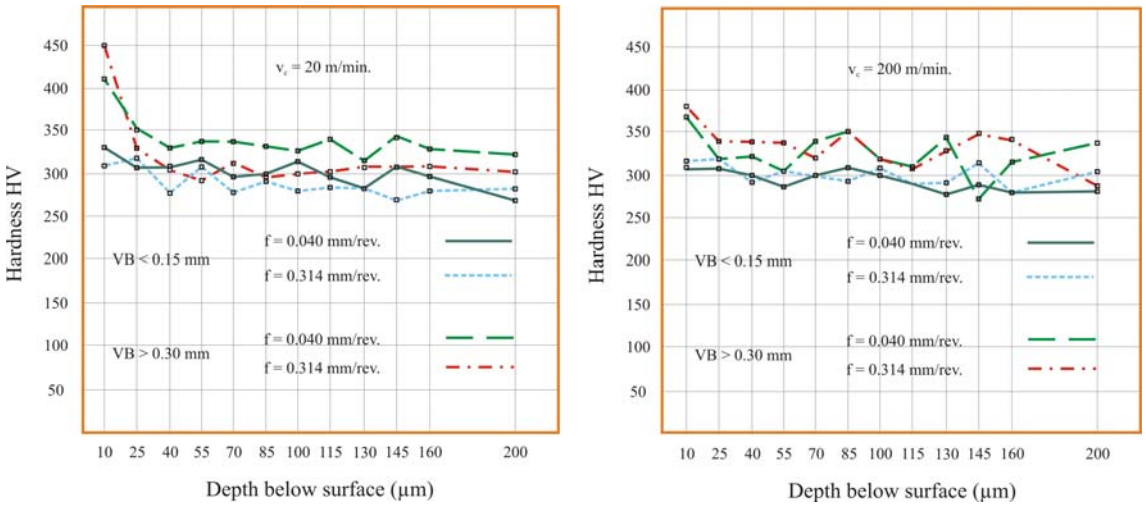

Figure 5.3: Hardness as a function of the feed rate *f* and the tool wear *VB* [42].

Figure 5.3 indicates that the cutting speed does not exert a noticeable influence on hardness.

6. Microstructure

The surface texture is generated by a combination of various factors that are due either to the manufacturing process or the material being finished. Of the factors due to the material, the most fundamental is the microstructure of the material. For example, cast aluminum surfaces generally produce a granular surface when machined, while wrought aluminum alloys can be machined to produce a highly reflective, flat and smooth topography [49].

Surface structural change in workpieces introduced by a material removal process is an important consequence of any finishing process. This surface modification occurs because of intense, localized and rapid thermal mechanical working resulting in metallurgical transformation and, perhaps, chemical interactions. The worked surface can show an extremely different structure from the bulk.

A microstructural perspective of machined surfaces is white layer. White layer is a result of microstructural alteration. It is called white layer because it resists standard etchants and appears white under an optical microscope (or featureless in a scanning electron microscope).

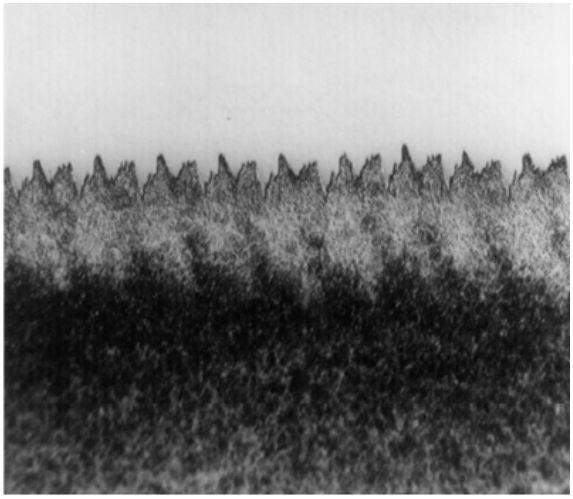

Figure 6.1: An example of microstructural change at a hard turned of 52100 steel, optical micrograph [50].

White layers are found in many material removal processes such as grinding [51-53], electrical discharge machining [54] and drilling [55]. In grinding, white layers have been suggested to have an untempered martensitic structure [53]. In cutting of hard steels, there are some reports of white layers [56-60]. Most noted that white layer occurs when cutting tools wear out to a certain level, but did not provide an in-depth explanation. Tönshoff et al. [60]

studied the influence of hard turning on workpiece properties and reported that retained austenite is the major composition of white layer structures. Surface chemistry was also investigated; the concentration of trace elements is constant with depth, implying no chemical reaction. A higher thrust force component seems to accompany white layer occurrence, as tensile residual stress does. They further showed that the white layer decreases bending fatigue strength probably due to associated tensile residual stresses. In contrast, König et al. [56] and Abrao and Aspinwall [61] reported that, despite white layer occurrence, hard turned steels have greater fatigue resistance than ground steels. They considered that fine surface finish of hard turned parts resulted in longer fatigue life than ground counter parts even though the former had a deeper white layer. König et al. [62] further explained that strain-induced hardening could suppress the formation of a thermally damaged soft skin and could consequently show high levels of rolling strength even with a white layer.

Tool wear was suggested as the most influential parameter on white layer formation, though frequently it was the only variable studied. However, the explanation of white layer formation was rather qualitative and, thus, there was no implication that optimization of surface structures or minimization of white layers is possible [50].

In this thesis, the observations of machined surfaces show no white layer after machining. The absence of the white layer is due to the greater thermal stability of the material used in this work.

7. Surface Integrity and Fatigue

Metals subjected to a repetitive or fluctuating stress will fail at a stress much lower than that required to cause fracture under a constant stress. Failures occurring under conditions of dynamic loading are called fatigue failures, presumably because it is generally observed that these failures occur only after a considerable period of service. A fatigue failure is particularly insidious because it occurs without any obvious warning [63].

An important structural feature which appears to be unique to fatigue deformation is the formation on the surface of ridges and grooves called slip-band extrusions and slip-band intrusions. Extremely careful metallography on tapered sections through the surface of the specimen has shown that fatigue cracks initiate at intrusions and extrusions.

Wood [64], who made many basic contributions to the understanding of the mechanism of fatigue, suggested a mechanism for producing slip-band extrusions and intrusions. He interpreted microscopic observations of slip produced by fatigue as indicating that the slip bands are the result of a systematic buildup of fine slip movements, corresponding to movements of the order of 1 nm rather than steps of 100 to 1000 nm, which are observed for static slip bands. Such a mechanism is believed to allow for the accommodation of the large total strain (summation of the microstrain in each cycle) without causing appreciable strain hardening. Figure 7.1 illustrates Wood's concept of how continued deformation by fine slip might lead to a fatigue crack.

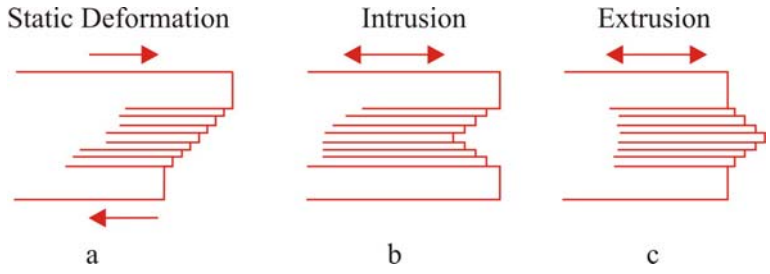

Figure 7.1: Wood's concept of microdeformation leading to formation of fatigue crack [65].

The figures illustrate schematically the fine structure of a slip band at magnifications obtainable with the electron microscope. Slip produced by static deformation would produce a contour at the metal surface similar to that shown in Figure 7.1a. In contrast, the back-and-forth fine slip movements of fatigue could build up notches Figure 7.1b or ridges Figure 7.1c

at the surface. The notch would be a stress raiser with a notch root of atomic dimensions. Such a situation might well be the start of a fatigue crack [65].

Fatigue cracks generally initiate from free surfaces and that performance is therefore reliant on the surface integrity produced by machining. Koster and Field [66] suggested that the major mechanical property affected by machining is high cycle fatigue strength, the actual endurance limit being dependent on the particular process used and the severity of operation.

7.1. Effect of Surface Topography on Fatigue

In many early fatigue models, the effect of surface topography on fatigue strength was considered by the amplitude surface roughness parameters, in particular the arithmetic average roughness, R_a. Siebel and Gaier [67], for instance, compared fatigue strength with the maximum depth of surface irregularities, measured by a surface roughness scan, and found a critical depth below which there was no change in fatigue strength and above which there was a linear fall in fatigue strength. Many researchers proposed the surface roughness parameters as appropriate factor to correct the endurance limit. In contrast, Syren [68] reported that the standard surface roughness parameters provide a simple and useful means of quantifying profile height distributions, which are important for estimating fatigue strength, they are however relatively insensitive to specific features of the surface height distribution. He showed that not only the maximum depth of surface irregularity but also the whole surface topography influences the fatigue strength. This means that the standard surface roughness parameters should not be used on an individual basis for evaluating the effect of surface finish on fatigue strength.

7.1.1. Effect of Stress Concentration on Fatigue

The effects of macroscopic geometric discontinuities on the strength of engineering components are usually approached in terms of the stress concentration factor, K_t. The surface stress concentration factor characterizes the stress at the edge of a hole or at a notch root of the surface topography [69]. The theoretical dependency between the stress concentration factor and the size of surface grooves is defined by the Neuber rule [70].

$$K_t = 1 + n\sqrt{\lambda \frac{R_z}{\rho}} \qquad \text{Eq. (7.1)}$$

where R_z and ρ are the 10-point surface height and the notch root radius, respectively. Coefficient n depends on the kind of stresses: $n = 1$ in shear and $n = 2$ in tension and bending. Coefficient λ depends on the ratio of spacing and height of surface irregularities.

The effectiveness of the notch in decreasing the fatigue limit is expressed by the fatigue-strength reduction factor, or fatigue-notch factor, K_f. Kuhn et al. [71] explained K_f as the ratio of the fatigue strength of a smooth specimen to the fatigue strength of a notched specimen under the same experimental conditions and the same number of cycles. The limiting condition proposed for K_f is explained as $1 \leq K_f \leq K_t$. The fatigue notch factor is dependent on many parameters such as size and geometry, stress gradient, material properties and loading type. Two general trends are usually observed for test conditions of completely reversed loading. First, K_f is usually less than K_t, and second, the ratio of K_f/K_t decreases as K_t increases. Thus, very sharp notches (high K_t) have less effect on fatigue strength than would be expected from their high value of K_t. The notch sensitivity of a material in fatigue is expressed by a notch-sensitivity factor q, [72].

$$q = \frac{K_f - 1}{K_t - 1} \qquad \text{Eq. (7.2)}$$

Eq. (7.2) was chosen so that a material which experiences no reduction in fatigue due to a notch ($K_f = 1$) has a factor of $q = 0$, while a material in which the notch has its full theoretical effect ($K_f = K_t$) has a factor of $q = 1$. However, q is not a true material constant since it varies with the severity and type of notch (Figure 7.2), the size of specimen (large components failing sooner than expected), and the type of loading.

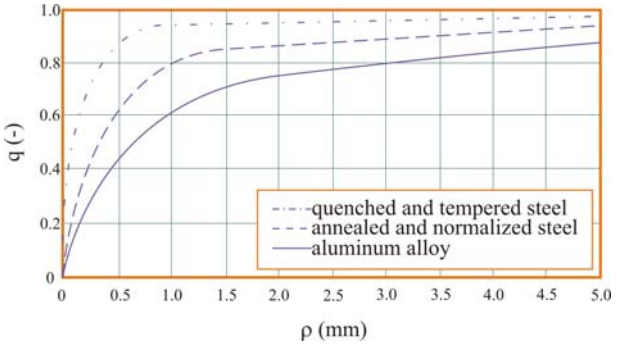

Figure 7.2: Variation of notch-sensitivity index with notch radius for materials of different tensile strength [65].

As Figure 7.2 indicates notch sensitivity increases with tensile strength. Thus, it is possible in certain circumstances to decrease fatigue performance by increasing the hardness or tensile strength of a material.

Neuber [70] proposed another approach for defining K_f based on the average stress model instead of the peak stress. He expressed the fatigue stress concentration factor as Eq. (7.3).

$$K_f = 1 + \frac{K_t - 1}{1 + \sqrt{\frac{\rho^*}{\rho}}} \qquad \text{Eq. (7.3)}$$

The above relationship express the fact that, for large notches with large radii, K_f is almost equal to K_t, but for small notches it is found $K_f << K_t$ for soft ductile metals and K_f higher for stronger metals. This means that these are more notch sensitive [65].

The classical approaches can be most useful, where the calculations are made to ensure an infinite fatigue life, i.e. to maintain stress levels below the fatigue limit, however, in the finite life regime such calculations can be dangerous. The major failing of the classical approach is that failure is associated with bulk stress or strain parameters and not to the behavior of a fatigue crack and its local stress strain field. Such bulk parameters do not take into account the various regimes of fatigue, the duration of which are dependent on stress level [73].

The limitations of classical approaches to notch fatigue studies via stress concentration factors, fatigue strength reduction factors and notch sensitivity factors are identified. They do not take into account the presence of a crack, they do not distinguish between the different modes and processes of crack extension and they say nothing about the extent and strength of the notch field. Thus the formulation of a new approach must eliminate some if not all of these deficiencies.

7.1.2. Fatigue Crack Propagation at Notches

Frost et. al. [74] investigated a series of tests in which the notch depth a is kept constant but the stress concentration factor is varied by modifying the notch root radius ρ, Figure 7.3.

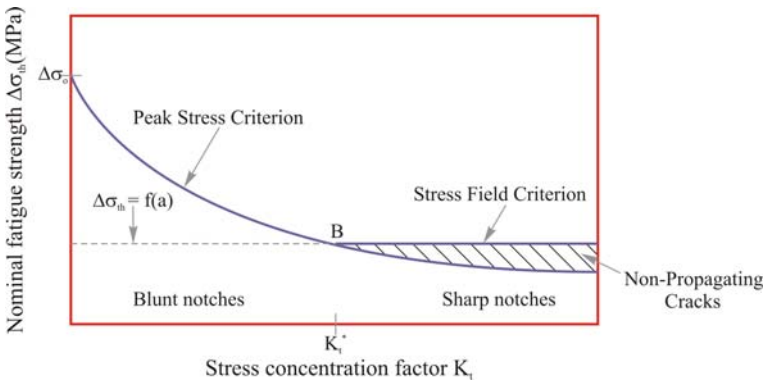

Figure 7.3: Nominal stress at fatigue limit versus the theoretical stress concentration factor for notches of constant depth *a* [75].

It can be seen that the fatigue initially falls rapidly as K_t increases, but beyond the critical value K_t*, the fatigue limit of the notched specimens remains constant despite increases in K_t. Above the branch point B (the junction between the two lines), the initiation of a fatigue crack is the necessary and sufficient criterion for complete failure. This criterion is correctly predicted by the notch root fatigue stresses. Below the branch point, fatigue crack initiation is correctly predicted by notch root fatigue stresses, but this is not a sufficient condition for complete failure, and non propagating cracks may be present in unbrocken specimens after testing to very long endurances. Smith and Miller [75] showed that all notches with K_t greater than K_t* behave identically and can be treated like cracks of the same length [76].

Eq. (7.4) shows the fatigue limit of cracked components based on linear elastic fracture mechanics.

$$\Delta\sigma_{th} = \frac{\Delta K_{th}}{\sqrt{\pi a}} \qquad \text{Eq. (7.4)}$$

In a cracked metallic specimen the fatigue limit is sometimes controlled by the crack length, together with the threshold for fatigue crack propagation. The relationship, for a metallic material, between the fatigue limits of specimens containing cracks of various sizes and the fatigue limit of an uncracked (plain) specimen may be summarized by means of a Kitagawa diagram [77]. In a Kitagawa diagram, shown schematically in Figure 7.4, fatigue limits are plotted against crack length, both on logarithmic scales.

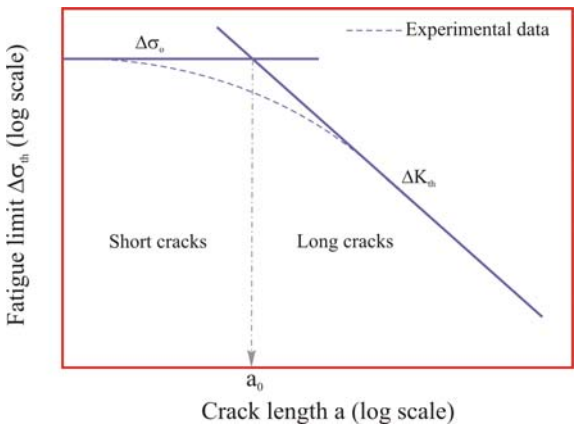

Figure 7.4: Kitagawa diagram showing relationship between crack length and fatigue limits [78].

In this diagram the fatigue limit of an uncracked specimen is shown by the horizontal line. If cracks are below a critical size then they have no effect on the fatigue limit. The other line, which has a slope of -0.5, shows fatigue limits calculated from the crack length and the long crack fatigue crack propagation threshold using an appropriate expression for the *Mode I* stress intensity factor. Actual material behavior, shown by the dashed line, is a smooth blend between the two straight lines. This blend can be interpreted as summarising the threshold behavior of short cracks [76].

Atzori and Lazzarin [78] showed that notch sensitivity and defect sensitivity are two different aspects of the fatigue behavior of materials. They extended the Kitagawa diagram to blunt cracks (U-shaped notches) and proposed the Eq. (7.5).

$$K_t = \left(\frac{a^*}{a_0} \right)^{0.5} \qquad \text{Eq. (7.5)}$$

where a_0 is the El-Haddad's length parameter and a^* is a particular blunt crack depth corresponding to the intersection between the ΔK_{th} and $\Delta\sigma_0/K_t$ curves. The expression proposed by Atzori and Lazzarin provides an explicit bridging between the classic concept of notch sensitivity and the concept of sensitivity to defect. They showed that the Kitagawa-Takahashi diagram can be seen as a limit case, valid for components scaled in geometrical proportion and weakened by a notch tip radius ρ, which tends towards zero, Figure 7.5 [78].

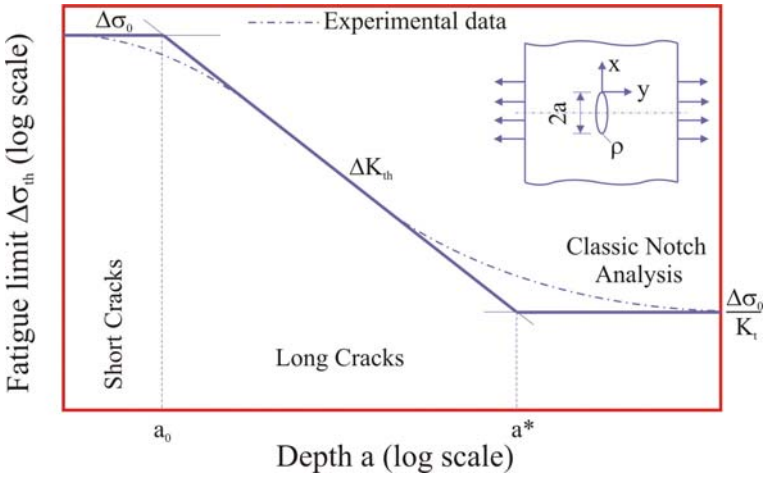

Figure 7.5: Fatigue behavior of a material weakened by notches or cracks [78].

Neuber [70] proposed an approximation solution for the mode I stress intensity factor K_I of a crack at the root of a semi-elliptical notch Figure 7.6, Eq. (7.6).

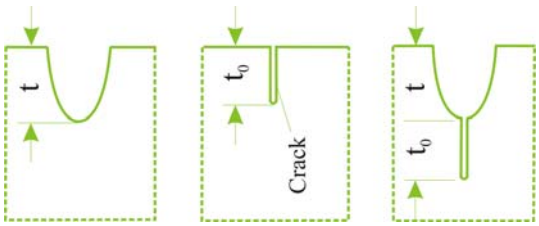

Figure 7.6: Semi-elliptical notch with crack, according to Neuber [79].

$$\frac{K_I}{K_{IL}} = s \cdot \left\{ 1 + \left[\left(K_t - 1 \right)^{-2.5} + \left(\frac{1}{s} - 1 \right)^{-2.5} \right]^{-0.4} \right\} \qquad \text{Eq. (7.6)}$$

where K_{IL} and s are the stress intensity factor for a long crack having a length of $(t + t_0)$ and geometrical factor of $\sqrt{t_0/(t_0+t)}$, respectively.

Liu [80] has developed the idea of Neuber to indicate the effect of surface profile using the surface fatigue factor F_S, Eq. (7.7).

$$F_{S,Liu} = \frac{\sigma_a}{\sigma_W} = \frac{1}{1+\left[\left(K_{t,Liu}-1\right)^{-2.5} + \left(\sqrt{1+\frac{R_{eff}}{a_0}}-1\right)^{-2.5}\right]^{-0.4}} \quad \text{Eq. (7.7)}$$

It should be noted that in Eq. (7.6) the geometrical value s is replaced by $\sqrt{a_0/\left(a_0+R_{eff}\right)}$.

This model characterizes the surface topography, besides the surface roughness R_{eff}, with the use of a surface stress concentration factor K_t and a characteristic structural length a_0. Note that the surface fatigue factor F_S exhibits the same expression as $1/K_f$.

The effect of surface finish can conveniently be characterized by the surface fatigue factor. This is the ratio of the fatigue strength σ_a for a particular surface finish to the fatigue strength σ_W (intrinsic fatigue strength) for carefully polished surfaces commonly used for laboratory specimens in which care has been taken to avoid the introduction of residual stresses or hardening or softening the surface layers.

7.2. Effect of Residual Stresses on Fatigue

The generation of residual stresses in hard machining has been investigated by many researchers. Especially important is the research showing that fatigue life is improved by inducing compressive residual stresses into the surface region [81].

It is well known that surface finish and residual stresses can significantly affect the resistance of components to failure when subjected to high cycle fatigue loads. The fatigue crack, in general, nucleates at the surface of the part, and then propagates into the bulk. As the crack extends the resistant section is reduced, and when the residual section can no longer withstand the applied load component failure occurs. Consequently, it is the state of stress at the surface, where the crack nucleates, that is of paramount importance. This state is the sum of the stress due to the applied load and of the residual stresses (or self stresses) generated during machining. If the surface residual stress is tensile and tensile stresses are applied, fatigue resistance may be significantly reduced [13].

Residual stresses can be considered identical to the stresses produced by an external force. Figure 7.7 illustrates the addition of a compressive residual stress, which exists at a point on the surface, to an externally applied tensile stress on that surface.

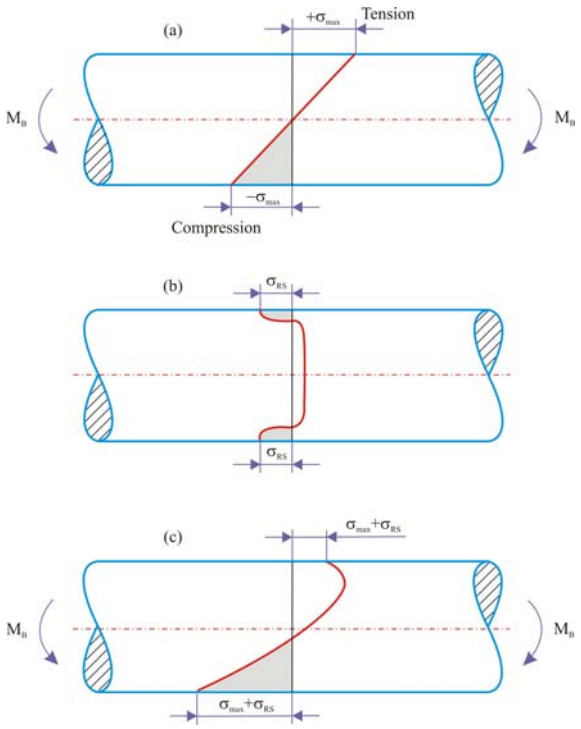

Figure 7.7: Superposition of applied and residual stresses [65].

Figure 7.7a shows the elastic stress distribution in a beam where there is no residual stress. A typical residual stress distribution, for instance, produced by shot peening is shown in Figure 7.7b. Figure 7.7c illustrates the stress distribution due to the algebraic summation of the applied bending stresses and the residual stresses. It can be seen that the peak tensile stress is displaced to a point in the interior of the specimen. Therefore, subsurface initiation of failure is possible under these conditions [65].

In general, tensile residual stresses decrease the fatigue limit and compressive residual stresses increase one. The fatigue limit in presence of residual stress can be expressed as in Eq. (7.8).

$$\sigma_a = \sigma_W - K \cdot \sigma_{RS} \qquad \text{Eq. (7.8)}$$

where σ_W is the fatigue limit in the absence of residual stresses. K is an empirical factor depending on the mechanical properties of the material. This factor ranges from 0.1 to 0.3. It should be noted that high values of K are typical for high strength metals. According to the Eq. (7.8), tensile residual stresses, which have positive sign, reduce the fatigue limit and

compressive residual stresses, which have negative sign, increase it. This effect is considerable when the tensile and compressive strengths of the metal differ significantly. Hardened high strength steels show a strong dependence of the fatigue limit on the residual stresses. On the contrary, in the ductile non-hardened steels this dependence is reduced. Figure 7.8 presents the correlation the fatigue limit with the residual stresses caused by rolling [19].

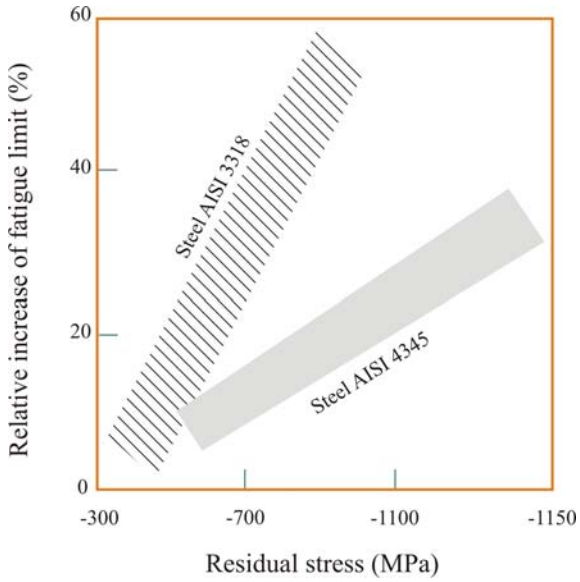

Figure 7.8: Fatigue limit increase versus residual stresses [19].

7.2.1. Calculating the Effect of Residual Stress Based on Uniaxial Fatigue

One way to take into account the influence of (macro) residual stresses on the fatigue behavior is to treat them as local mean stresses. It should be noted that there are several important differences between loading mean stresses and residual stresses. For instance, loading mean stresses are not influenced by cyclic plastic deformation while residual stresses always relax, if the cyclic loading exceeds certain threshold values [82].

Figure 7.9 illustrates a Haigh diagram for smooth and notched specimens made from a medium-strength steel.

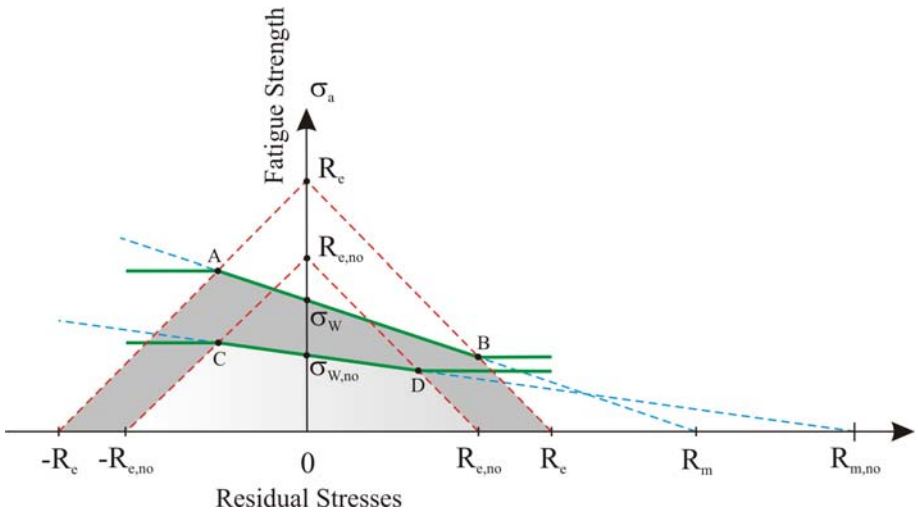

Figure 7.9: Haigh diagram of smooth and notched specimens made from a medium-strength steel versus residual stress [83].

The Goodman approximation is used to take into consideration the effect of residual stresses on the fatigue strength. If the amount of the minimum or maximum stress in smooth specimens does not exceed the critical stress amplitude $\sigma_{a,crit}$, which is a function of the cyclic yield strength, the residual stresses do not relax, and the line AB gives the effect of the residual stress on the fatigue limit. Therefore, all combinations of residual stress and stress amplitude inside the shaded area result in neither residual stress relaxation nor fatigue failure. On the contrary, if the amount of the minimum or maximum stress exceeds the critical stress amplitude, it is assumed that the residual stresses relax to the value given by the points A and B, respectively, and the fatigue strength remains constant at the value given by these points. For notched specimens, the cyclic yield strength and the notch fatigue strength are less than the respective values of smooth specimens. However, the ultimate tensile strength of notched specimens is larger than that of smooth ones in such a material state because of the triaxial stress state in the interior of the notched specimens. The Goodman relationship holds between points C and D, and residual stress relaxation occurs outside the lightly shaded area. These relationships show that the residual stress sensitivity of notched specimens is less than that of smooth specimens [82].

The calculation of residual stress based on endurance diagrams of the Haigh or Goodman type usually only allows for an estimation of the increase in fatigue strength as a function of the residuals stress. This approach uses for the combination of uniaxial stresses. Yet, the residual stresses are always multiaxil. This raises the problem of choosing a multiaxial fatigue

stress criterion. Skalli and Flavenot [84] showed that the traditional Mises and Tresca criteria can only be used in the presence of higher mean or residual stress. They also illustrated that the criteria of Crossland derived from the Mises criterion, which take into account hydrostatic pressure and the Dang Van criterion based on maximum hydrostatic pressure versus cyclic shear stress give a better correlation with experimental results.

In the case of combined and out-of-phase loading, new criteria have been developed to take the out-of-phase effect into account.

7.2.2. Calculating the Effect of Residual Stress Based on Multiaxial Fatigue

Multiaxial fatigue assessments are carried out using an appropriate rule or criterion to reduce the complex multiaxial loadings to an equivalent uniaxial loading. The multiaxial fatigue criteria are divided into three groups, i.e. stress criteria, strain criteria and energy criteria. The stress criteria can be categorized into three viewpoints, i.e. integral approaches, critical plane approaches, and empirical formulae. In the integral approach the calculation of the equivalent stress is carried out as an integral of the stresses over all cutting planes of a volume element. The critical plane approach assumes that the failure occurs in the critical plane with the maximal value of equivalent stress. The shear stress intensity hypothesis SIH and the quadratic failure criterion QVH are typical representatives for the integral method and critical plane approach, respectively.

7.2.2.1. Shear Stress Intensity Hypothesis (SIH)

This approach is based on an expression derived by Novozhilov [85] under the name of mean tangential stress. Novozhilov showed that the root mean square value of the shear stresses over all cutting planes is identical to the von Mises stress Eq. (7.9).

$$\tau_{\text{int}} = \left(\frac{1}{4\pi} \int_{\gamma=0}^{\pi} \int_{\varphi=0}^{2\pi} \tau_{\gamma\varphi}^{2} \cdot \sin\gamma \cdot d\varphi \cdot d\gamma \right)^{\frac{1}{2}} \cong \left(3I_2'\right)^{\frac{1}{2}} \qquad \text{Eq. (7.9)}$$

Simbürger [86] modified the idea of Novozhilov for application to fatigue problems under the name of effective shear stress hypothesis and has later been described by Zenner and Richter in a slightly modified form as the shear stress intensity hypothesis [87-88]. A further development of the shear stress intensity hypothesis was proposed by Liu [89-90]. In this

modification, the equivalent shear and normal stress amplitudes are evaluated as the integral of the stresses over all cutting planes, Figure 7.10.

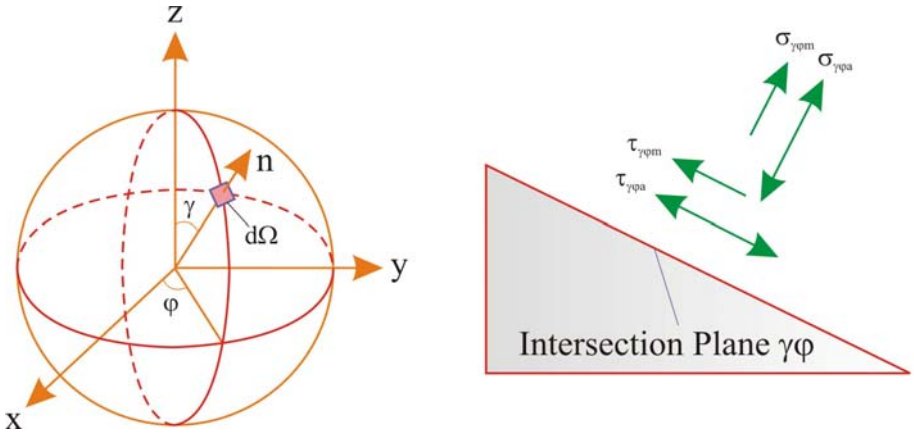

Figure 7.10: Integration domain of the SIH and stress components in the intersection plane $\gamma\varphi$ [90].

In order to obtain the mean stresses, the mean shear and normal stresses are weighted over the shear and normal stress amplitudes, respectively. Eqs. (7.10-7.13) show the simplified form of the equivalent stress for each of the four stress components in the cutting plane.

$$\tau_{va} = \left\{ \frac{15}{8\pi} \int_{\gamma=0}^{\pi} \int_{\varphi=0}^{2\pi} \tau_{\gamma\varphi a}^{2} \cdot \sin\gamma \cdot d\varphi \cdot d\gamma \right\}^{\frac{1}{2}} \qquad \text{Eq. (7.10)}$$

$$\sigma_{va} = \left\{ \frac{15}{8\pi} \int_{\gamma=0}^{\pi} \int_{\varphi=0}^{2\pi} \sigma_{\gamma\varphi a}^{2} \cdot \sin\gamma \cdot d\varphi \cdot d\gamma \right\}^{\frac{1}{2}} \qquad \text{Eq. (7.11)}$$

$$\tau_{vm} = \left\{ \frac{\int_{\gamma=0}^{\pi} \int_{\varphi=0}^{2\pi} \tau_{\gamma\varphi a}^{2} \cdot \tau_{\gamma\varphi m}^{2} \cdot \sin\gamma \cdot d\varphi \cdot d\gamma}{\int_{\gamma=0}^{\pi} \int_{\varphi=0}^{2\pi} \tau_{\gamma\varphi a}^{2} \cdot \sin\gamma \cdot d\varphi \cdot d\gamma} \right\}^{\frac{1}{2}} \qquad \text{Eq. (7.12)}$$

$$\sigma_{\mathrm{vm}} = \left\{ \frac{\int_{\gamma=0}^{\pi} \int_{\varphi=0}^{2\pi} \sigma_{\gamma\varphi a}^{2} \cdot \sigma_{\gamma\varphi m} \cdot \sin\gamma \cdot d\varphi \cdot d\gamma}{\int_{\gamma=0}^{\pi} \int_{\varphi=0}^{2\pi} \sigma_{\gamma\varphi a}^{2} \cdot \sin\gamma \cdot d\varphi \cdot d\gamma} \right\} \qquad \text{Eq. (7.13)}$$

Eq. (7.14) shows the failure condition using the combination of the equivalent shear and normal stresses.

$$a \cdot \tau_{\mathrm{va}}^{2} + b \cdot \sigma_{\mathrm{va}}^{2} + m \cdot \tau_{\mathrm{vm}}^{2} + n \cdot \sigma_{\mathrm{vm}} = \sigma_{W}^{2} \qquad \text{Eq. (7.14)}$$

where *a*, *b*, *m* and *n* are the coefficients of the shear stress intensity hypothesis [91].

7.2.2.2. Quadratic Failure Hypothesis (QVH)

The critical plane approaches to multiaxial fatigue have evolved from experimental observations of the initiation and growth of cracks during cyclic loading. Models in this class attempt to compute fatigue damage on specific planes within a test specimen or component. Troost and El-Magd [92] developed a general form of failure criterion based on the critical plane approach to predict the fatigue endurance limit under multiaxial stresses. This criterion takes account for anisotropic fatigue behavior which also occurs in the case of isotropic materials.

The QVH includes the relationship between the stress amplitude σ_A and mean stress σ_m in terms of uniaxial fatigue loading. Troost and El-Magd [93] proposed a general quadratic parabola to describe the function $\sigma_A(\sigma_m)$, Eq. (7.15).

$$\frac{\sigma_A}{\sigma_W} = 1 - p \cdot \left(\frac{\sigma_m}{R_m} \right) - (1 - p) \cdot \left(\frac{\sigma_m}{R_m} \right)^2 \qquad \text{Eq. (7.15)}$$

where *p* is a measure to evaluate the mean stress sensitivity, Eq. (7.16).

$$p = \frac{1 - \left[\frac{\sigma_{Sch}}{2 \cdot \sigma_W} + \left(\frac{\sigma_{Sch}}{2 \cdot R_m} \right)^2 \right]}{\frac{\sigma_{Sch}}{2 \cdot R_m} \cdot \left(1 - \frac{\sigma_{Sch}}{2 \cdot R_m} \right)} \qquad \text{Eq. (7.16)}$$

Figure 7.11 demonstrates the correlation between the stress amplitude σ_A with the mean stress σ_m for different values of p with reference to Haigh diagram.

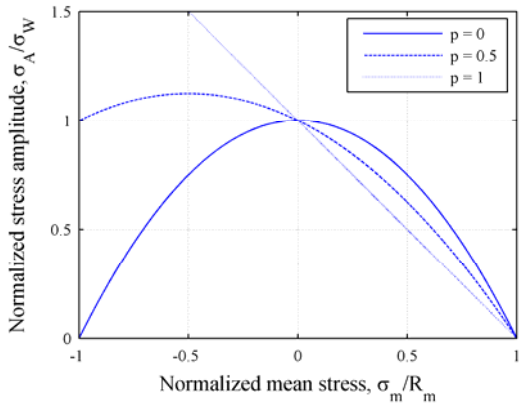

Figure 7.11: Stress amplitude vs. mean stress under uniaxial fatigue loading.

The straight line (p = 1) on the normalized plot was proposed by Goodman [94] and is called the Goodman line. The solid curve (p = 0) as illustrated in Figure 7.11 represents the Gerber parabola and the dashed curve (p = 0.5) refers to Dietmann parabola [95-96].

The stress components σ_x* and σ_y* for the stress state investigated in publication III are given by equation, Eq. (7.17).

$$\begin{aligned} \sigma_x^* &= \sigma_{xm}^* + \sigma_{xa}^* \cdot \sin \omega t \\ \sigma_y^* &= \sigma_{ym}^* \\ \tau_{xy}^* &= 0 \end{aligned} \qquad \text{Eq. (7.17)}$$

The same state of plane stress can be described on any other coordinate system, such as x-y (Figure 7.12). This system is related to the original one by an angle of rotation δ, and the values of the stress components change to σ_x and σ_y in the new coordinate system.

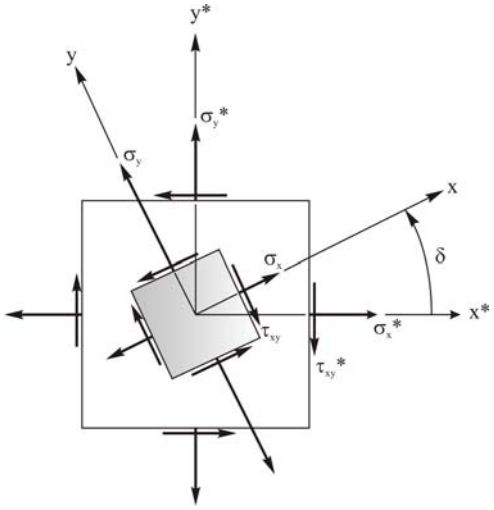

Figure 7.12: State of plane stress dependent on the rotation angle δ.

The stress components dependent on the angle δ are described as in Eqs. (7.18-7.19):

$$\begin{aligned} \sigma_{xm} &= \sigma^*_{xm} \cdot \cos^2\delta + \sigma^*_{ym} \cdot \sin^2\delta \\ \sigma_{ym} &= \sigma^*_{xm} \cdot \sin^2\delta + \sigma^*_{ym} \cdot \cos^2\delta \\ \tau_{xym} &= \left(\sigma^*_{xm} - \sigma^*_{ym}\right) \cdot \sin\delta \cdot \cos\delta \end{aligned} \qquad \text{Eq. (7.18)}$$

$$\begin{aligned} \sigma_{xa} &= \sigma^*_{xa} \cdot \cos^2\delta \\ \sigma_{ya} &= \sigma^*_{xa} \cdot \sin^2\delta \\ \tau_{xya} &= \sigma^*_{xa} \cdot \sin\delta \cdot \cos\delta \end{aligned} \qquad \text{Eq. (7.19)}$$

Eq. (7.20) shows the failure criterion proposed by Troost and El-Magd [97] based on stress state investigated in the publication III.

$$\left(\frac{\sigma_{xa}}{\sigma_{Ax}}\right)^2 + \left(\frac{\sigma_{ya}}{\sigma_{Ay}}\right)^2 - \frac{\sigma_{xa} \cdot \sigma_{ya}}{\sigma_{Ax} \cdot \sigma_{Ay}} + \left(\frac{\tau_{xya}}{\sigma_{Axy}}\right)^2 = 1 \qquad \text{Eq. (7.20)}$$

σ_{Ax}, σ_{Ay} and σ_{Axy} are the stress amplitudes as a function of mean stress in terms of uniaxial fatigue loading according to [97] given by equations, Eqs. (7.21-7.23).

$$\sigma_{Ax} = \sigma_W \cdot \left[1 - p \cdot \left(\frac{\sigma_{xm}}{R_m} \right) - (1 - p) \cdot \left(\frac{\sigma_{xm}}{R_m} \right)^2 \right] \qquad \text{Eq. (7.21)}$$

$$\sigma_{Ay} = \sigma_W \cdot \left[1 - p \cdot \left(\frac{\sigma_{ym}}{R_m} \right) - (1 - p) \cdot \left(\frac{\sigma_{ym}}{R_m} \right)^2 \right] \qquad \text{Eq. (7.22)}$$

$$\sigma_{Axy} = \frac{\sigma_W}{\sqrt{3}} \cdot \frac{\left[1 - (1-p) \cdot \left(\frac{\tau_{xym}}{R_m} \right)^2 \right]^2 - p^2 \cdot \left(\frac{\tau_{xym}}{R_m} \right)^2}{\sqrt{\left[1 - (1 - p) \cdot \left(\frac{\tau_{xym}}{R_m} \right)^2 \right]^2 + \left(\frac{p^2}{3} \right) \cdot \left(\frac{\tau_{xym}}{R_m} \right)^2}} \qquad \text{Eq. (7.23)}$$

Troost and El-Magd [92, 97] justified that the failure condition is fulfilled by the orientation angles at either $\delta = 0°$ or $\delta = 45°$ with respect to considered stress state. These angles are called critical orientations.

7.2.3. Influence of Surface Layer on Fatigue (Strain Hardening)

The condition of metal structure in the surface layer has a large impact on the fatigue life of a part. During processing the workpiece, cutting force and friction induce the plastic deformation in the surface layer. The plastic deformation of the metal alters its strength, hardness, elasticity, ductility and creep. An increase of the plastic deformation causes an increase of the strength properties such as yield point, fatigue strength, hardness up to a certain level and the elasticity modul changes. The ductility properties such as area reduction and elongation decrease.

Strain hardening of the surface layer is defined by parameters such as strain-hardening depth, strain-hardening rate and strain-hardening gradient. Measurement of microhardness and X-ray analysis methods are employed to determine these parameters. The rate of strain hardening ranges from 10 to 20 percent for hard metals, 20 to 40 percent for structural steels and 30 to 70 percent for high-temperature resistant alloys and stainless steel [19].

The effect of surface layer on fatigue strength is illustrated in Figure 7.13, where S/N curves are compared for steel specimens produced by two different kinds of turning processes.

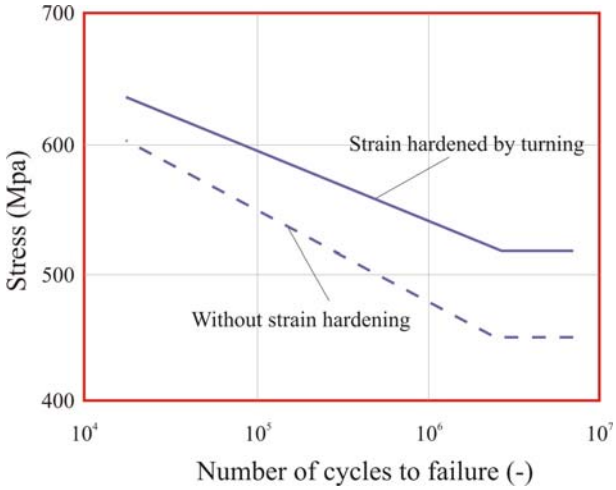

Figure 7.13: S/N curves for AISI 4335 [19].

Figure 7.13 shows that specimens in strain-hardened condition have a higher fatigue limit. This means that an increase in surface layer hardness makes it possible to increase the fatigue limit. It should be noted that the strain-hardened surface layer blocks propagation of fatigue cracks and resists formation of the new ones.

Figure 7.14 illustrates the effects of strain-hardened layer thickness and rate of strain hardening on the fatigue limit of the AISI 1045 carbon steel.

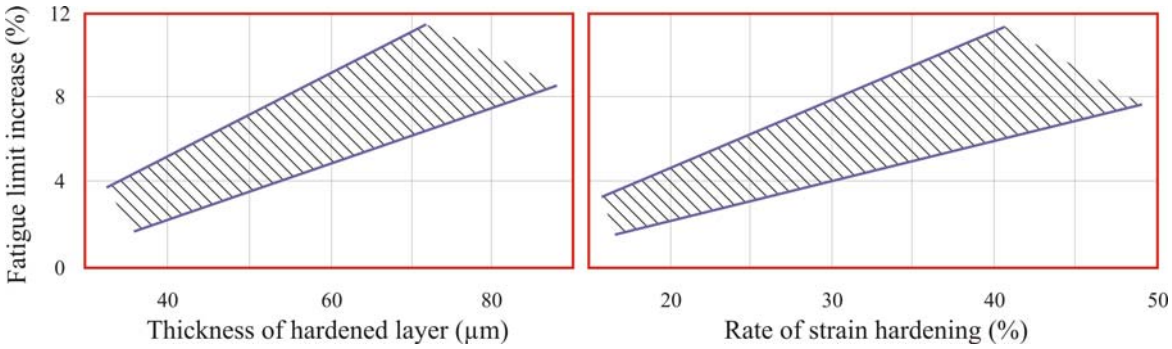

Figure 7.14: Increase of fatigue limit versus thickness of hardened surface layer and rate of strain hardening of AISI 1045 steel after turning [19].

It can be seen that the fatigue limit increases in direct proportion to the thickness of the strain hardened layer.

The magnitude of strain hardening depends on the structural condition of the metal. The martensite and ferrite steels show a higher magnitude of strain hardening in comparison with the steels with sorbite structure, Figure 7.15.

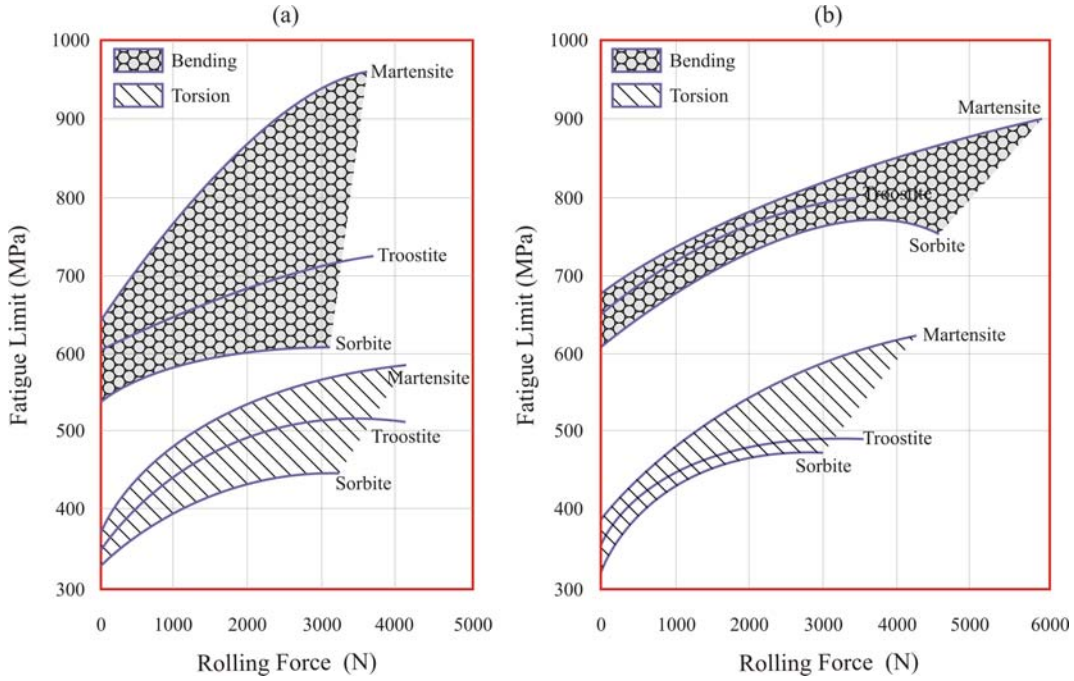

Figure 7.15: Fatigue limit versus rolling force for different structural conditions, (a) steel AISI 3318 and (b) steel AISI 4345 [19].

8. Material and Testing Methods

8.1. Material

Properties such as hardness, strength, ductility and toughness are dependent on the microstructural products that are present in steel. Heat treating of the various steel processing methods has the greatest overall impact on control of microstructure, properties, residual stresses and dimensional control. Heat treatment processes can be divided into hardening and annealing processes. The traditional route to high strength in steels is by quenching to form martensite which is subsequently reheated or tempered at an intermediate temperature, increasing the toughness of the steel without a great loss in strength [98-99].

For the optimum development of strength, the first step in the transformation process is to heat the steel to its austenitizing temperature. The steel is then cooled rapidly to avoid the formation of pearlite, which is a relatively soft transformation product, to maximize the formation of martensite, a relatively hard transformation product, and to achieve the desired as-quenched hardness. The effectiveness of the quench depends primarily on two factors: the geometry of the specimen and the composition of the steel. The addition of common alloying elements such as Cr, Mo, V and W leads to a reduction in the critical rate of cooling needed to make a steel specimen fully martensitic [99]. The most common transformational products that may be formed from austenite in quench-hardenable steels are, in order of formation with decreasing cooling rate: martensite, bainite, perlite, ferrite and cementite. The transformation products formed are typically illustrated with the use of transformation diagrams, which show the time-temperature dependence of the microstructure formation process for the alloy being study [98-99].

Figure 8.1 shows the time-temperature-transformation diagram (TTT-diagram) for a 34CrNiMo6 steel. This diagram demonstrates how the microstructure is affected by the occurring cooling and quenching conditions. In this case the austenitizing temperature is 850 °C, where austenite transformation structure is completely formed. The temperature AC_1 is where transformation to austenite begins and temperature AC_3 is where the transformation to austenite is complete.

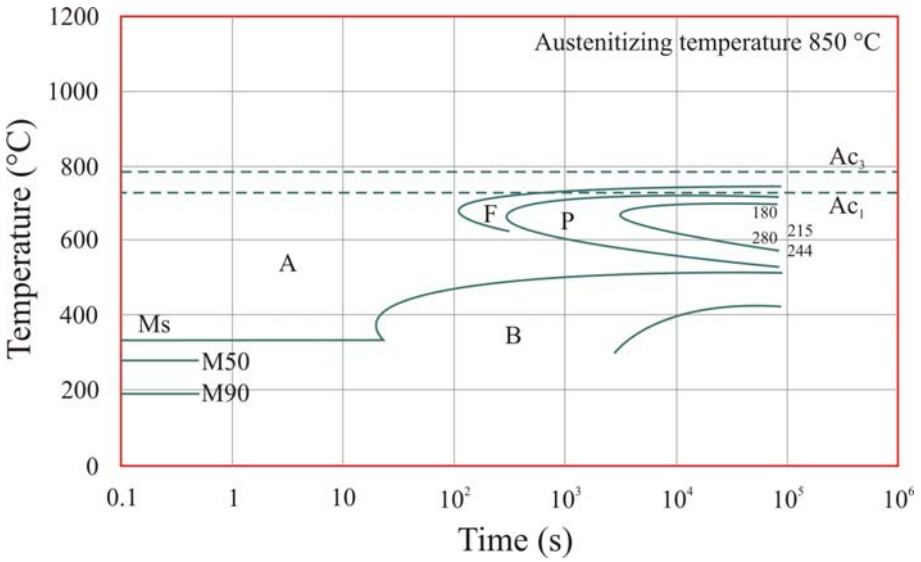

Figure 8.1: Time-temperature-transformation diagram of 34CrNiMo6 steel.

The recommended process parameters for the heat treatment of the steel 34CrNiMo6 are shown in Table 8.1. The specimens used in this thesis were quenched down from 840 °C in oil and annealed at a temperature between 650 and 680 °C.

Quenched and tempered steel 34CrNiMo6		
Quenching temperature	Quenching agent	Annealing temperature
830 - 860 °C	Oil	650 - 680 °C

Table 8.1: Heat treatment process parameters for 34CrNiMo6 according to DIN EN 10083-1.

To improve the resulting material strength, hardened materials are often tempered. This leads to an increased ductility with only a small decrease in tensile and yield strength [98-99]. Figure 8.2 shows the influence of the tempering temperature on the mechanical properties of the quenched and tempered 34CrNiMo6 steel.

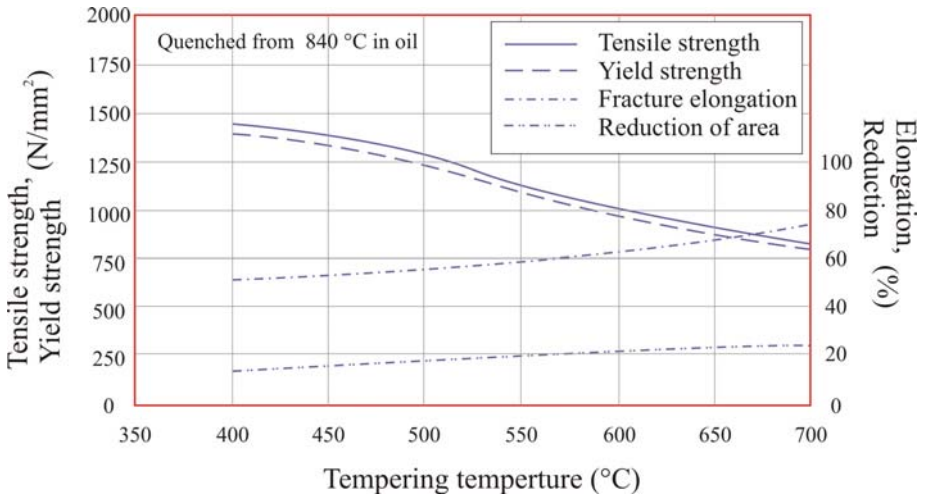

Figure 8.2: Mechanical properties of the quenched and tempered 34CrNiMo6 steel.

As expected, both the tensile strength and the yield strength decrease with increasing tempering temperature. The fracture elongation increases with increasing tempering temperature.

8.2. Testing Methods

In order to characterize the material behavior, testing methods were carried out, that are briefly described in the following.

8.2.1. Uniaxial Tension Testing

The basic principle of the tension test is quite simple. The tension test is accomplished by gripping opposite ends of a test item within the load frame of a test machine. A tensile force is applied by the machine, resulting in the gradual elongation and eventual fracture of the test item. During this process, force-extension data, a quantitative measure of how the test item deforms under the applied tensile force, usually are monitored and recorded. Figure 8.3 shows the testing machine employed in this work.

Figure 8.3: A 100 kN servohydraulic test machine and load frame.

There are various tensile testing specifications from several standards organizations. These specifications define requirements for the test apparatus, test specimens and test procedures. Figure 8.4 illustrates the standard geometry for the tensile specimens. Dimensions for the specimen are taken form ASTM.

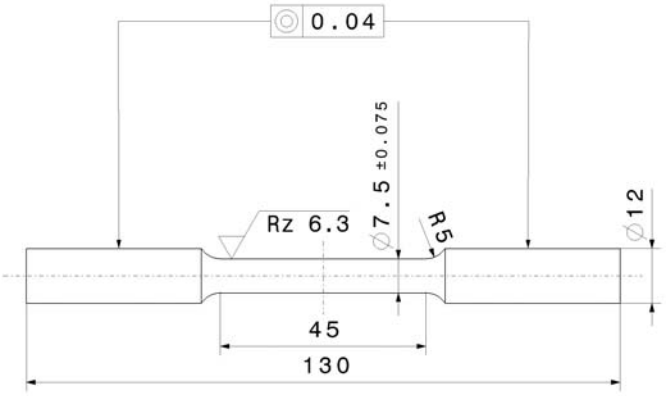

Figure 8.4: Geometry of tension test specimen per DIN EN 10002.

Appendix C shows the results of uniaxial tension testing.

8.2.2. Uniaxial Fatigue Testing

In order to characterize the fatigue strength, a constant-moment fatigue testing machine was used, Figure 8.5.

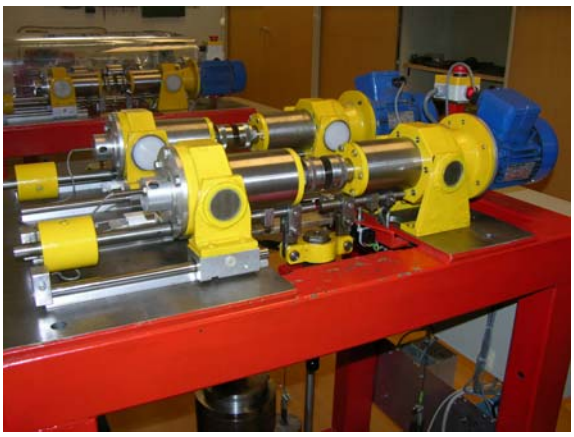

Figure 8.5: Rotating-bending testing machine.

A rotating test specimen is subjected to a constant bending moment over its entire length, Figure 8.6.

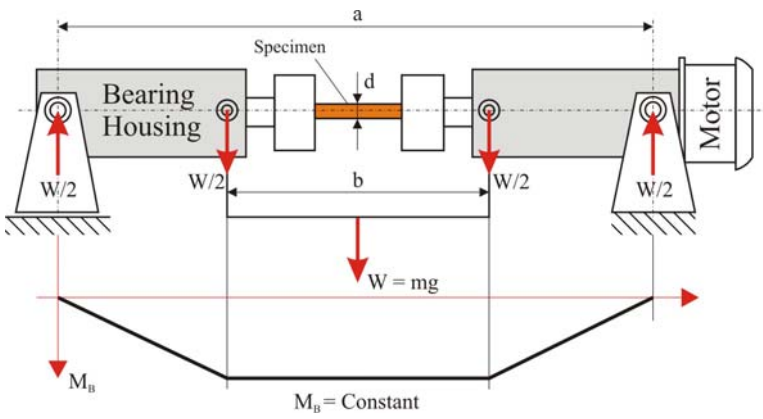

Figure 8.6: Schematic of a rotating-bending fatigue testing machine.

This machine works in accordance with the rotating bending principle that, as the specimen rotates around its bent axis, it is subjected to cyclic stresses of a constant amplitude. The specimen experiences a stress which alternates with time between maximum and minimum. At each half revolution it changes from tension to an equal compression. The cycle

is repeated at the frequency of rotation. A substantial number of specimens are tested at different stress amplitudes to register the failure point.

Figure 8.7 illustrates the geometry of rotating bending test specimen employed for the fatigue testing.

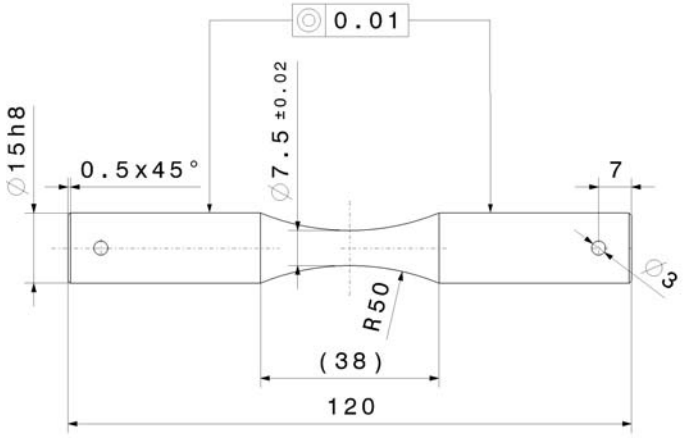

Figure 8.7: Rotating bending test specimen.

The results of fatigue testing for different surface conditions are given in Appendix D.

9. Conclusions

The major conclusions regarding the turning process parameters, surface integrity and fatigue performance are summarized in this chapter and put into perspective using a flow chart model.

A study of the effect of cutting parameters on the conditions of the subsurface microstructure of machined surfaces shows that a very thin localized plastic deformation zone of about 3-4 μm is generated after machining using different feed rates and tool nose radii. The microhardness analyses reveal that there is no significant variation in hardness beneath the machined surface produced by different cutting conditions.

The observations of the generated residual stresses reveal that the residual stresses are in tension at the surface in all the turning conditions and tend to become in compression inside the material. The main reason for this stress gradient is the high temperature attained during the cutting process. The machined surface is submitted to quenching due to the very important and fast increase/decrease of local temperature. The heat generation is mainly due to the formation of the tertiary shear zone. Contrary to the turned specimens, ground and peened specimens only show compressive residual stresses. In the case of turned specimens, residual stresses are dominated by the process parameters feed rate and tool nose radius. An increase in feed rate and nose radius leads to an increase in residual stresses in both axial and circumferential directions.

Tests on the achievable surface finish at different feed rates and tool nose radii show that the actual surface roughness does not match the theoretical surface roughness due to tool vibration and chip adhesion in surface finishing process. The analysis of surface texture reveals that the surface roughness at the same feed rate becomes higher when a small nose radius is used.

The observation of fatigue behavior of different surface conditions confirms that the surface topography and residual stresses are the key parameters that control fatigue performance after machining. Therefore, these parameters must be simultaneously taken into account in the evaluation of fatigue strength.

A reasonable agreement between the predicted and experimental fatigue strength is obtained using the proposed models indicating the surface fatigue factor and surface residual stress factor. A proposal model to predict the fatigue strength based on surface alterations after machining is illustrated below:

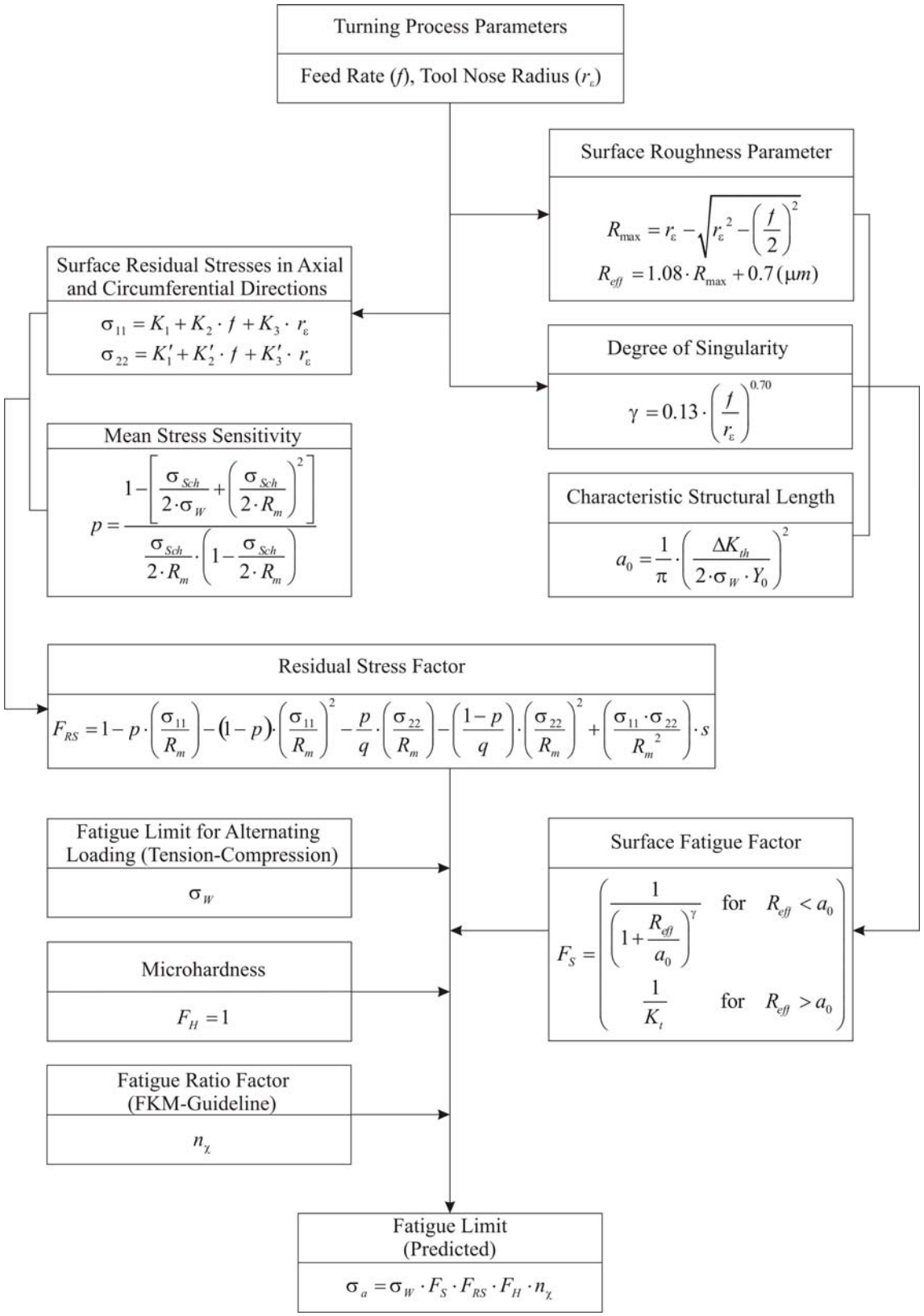
Turning Process Parameters
Feed Rate (f), Tool Nose Radius (r_ε)
Surface Roughness Parameter
$R_{\max} = r_\varepsilon - \sqrt{r_\varepsilon^2 - \left(\frac{f}{2}\right)^2}$
$R_{eff} = 1.08 \cdot R_{\max} + 0.7\,(\mu m)$
Surface Residual Stresses in Axial and Circumferential Directions
$\sigma_{11} = K_1 + K_2 \cdot f + K_3 \cdot r_\varepsilon$
$\sigma_{22} = K_1' + K_2' \cdot f + K_3' \cdot r_\varepsilon$
Degree of Singularity
$\gamma = 0.13 \cdot \left(\frac{f}{r_\varepsilon}\right)^{0.70}$
Mean Stress Sensitivity
$p = \frac{1 - \left[\frac{\sigma_{Sch}}{2 \cdot \sigma_W} + \left(\frac{\sigma_{Sch}}{2 \cdot R_m}\right)^2\right]}{\frac{\sigma_{Sch}}{2 \cdot R_m} \cdot \left(1 - \frac{\sigma_{Sch}}{2 \cdot R_m}\right)}$
Characteristic Structural Length
$a_0 = \frac{1}{\pi} \cdot \left(\frac{\Delta K_{th}}{2 \cdot \sigma_W \cdot Y_0}\right)^2$
Residual Stress Factor
$F_{RS} = 1 - p \cdot \left(\frac{\sigma_{11}}{R_m}\right) - (1-p) \cdot \left(\frac{\sigma_{11}}{R_m}\right)^2 - \frac{p}{q} \cdot \left(\frac{\sigma_{22}}{R_m}\right) - \left(\frac{1-p}{q}\right) \cdot \left(\frac{\sigma_{22}}{R_m}\right)^2 + \left(\frac{\sigma_{11} \cdot \sigma_{22}}{R_m^2}\right) \cdot s$
Fatigue Limit for Alternating Loading (Tension-Compression)
σ_W
Surface Fatigue Factor
$F_S = \begin{cases} \frac{1}{\left(1 + \frac{R_{eff}}{a_0}\right)^\gamma} & \text{for } R_{eff} < a_0 \\ \frac{1}{K_t} & \text{for } R_{eff} > a_0 \end{cases}$
Microhardness
$F_H = 1$
Fatigue Ratio Factor (FKM-Guideline)
n_χ
Fatigue Limit (Predicted)
$\sigma_a = \sigma_W \cdot F_S \cdot F_{RS} \cdot F_H \cdot n_\chi$

10. Appendix

10.1. Appendix A: Nomenclature

A	elongation to failure
B	spacing between two notches
F_{RS}	residual stress factor
F_S	surface fatigue factor
K	empirical coefficient
K^*_t	critical value of stress concentration factor
K_f	fatigue notch factor
K_I	mode I stress intensity factor
K_t	stress concentration factor
L	reference length
M, M_τ	mean stress sensitivity
N_f	number of cycles to failure
R	stress ratio
R^2	regression coefficient
R_a	average roughness
R_e	yield strength
R_{eff}	effective surface roughness
R_m	tensile strength
R_p	maximum peak height
R_v	maximum valley depth
R_y, R_{max}	peak-to-valley height
R_z	10-point surface height
VB	tool wear
V_c	cutting speed
Y_0	geometric correction factor
a,b,m,n	coefficients of SIH
a	notch or crack size
a_0	characteristic structural length

a_p	cutting depth
b	notch pitch
d_0	specimen diameter at test zone
f	feed rate
l_0	integral length
n	stress state
n_χ	fatigue ratio factor
p	mean stress sensitivity according to QVH
q,s	empirical parameter of EMP
r_ε	tool nose radius
s	geometrical factor
t	height of surface irregularities
t_0	crack length
$z(x)$	profile height distribution
ΔK	stress intensity factor range
ΔK_0	threshold stress intensity factor
σ_a, τ_a	stress amplitude
γ	degree of singularity
δ	rotating angle
λ	ratio between spacing and height
ρ	notch root radius
ρ^*	material constant
σ_{11}	axial residual stress
σ_{22}	circumferential residual stress
σ_A	stress amplitude in uniaxial fatigue loading according to QVH
σ_{bW}	fatigue limit for alternating axial loading (bending)
σ_m, τ_m	mean stress
σ_{RS}	residual stress
σ_{Sch}	fatigue limit for pulsating axial loading
σ_{va}, τ_{va}	equivalent stress amplitude
σ_{vm}, τ_{vm}	equivalent mean stress
σ_W	fatigue limit for alternating axial loading (tension-compression)
τ_{Sch}	fatigue limit for pulsating torsional loading
τ_W	fatigue limit for alternating torsional loading
φ	notch opening angle

10.2. Appendix B: Microhardness and Residual Stresses

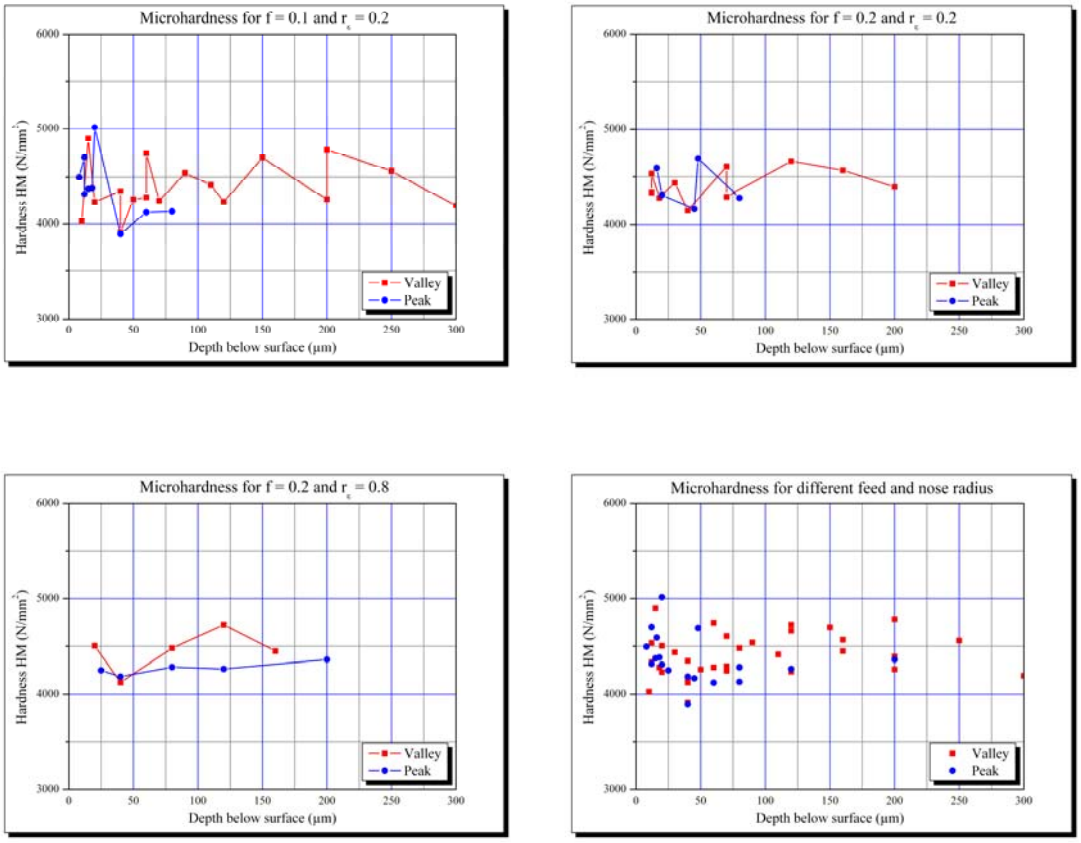

Figure 10.1: Microhardness variations beneath the machined surface.

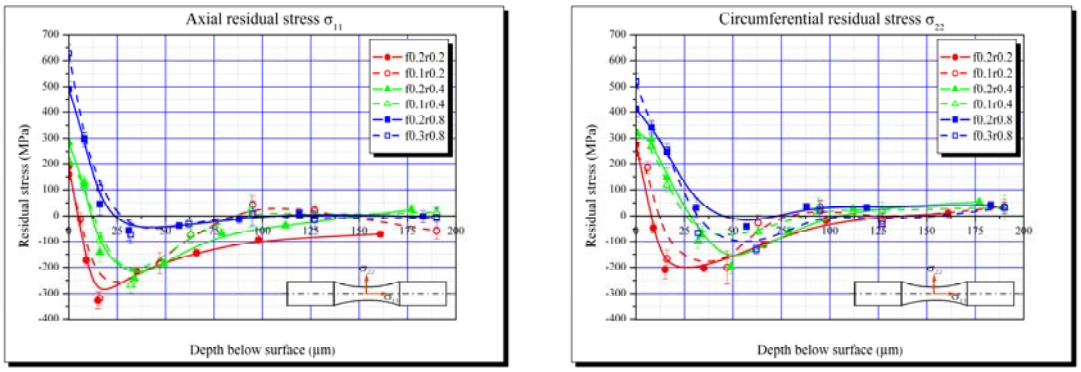

Figure 10.2: Residual stress distributions obtained by different feed rates and nose radii.

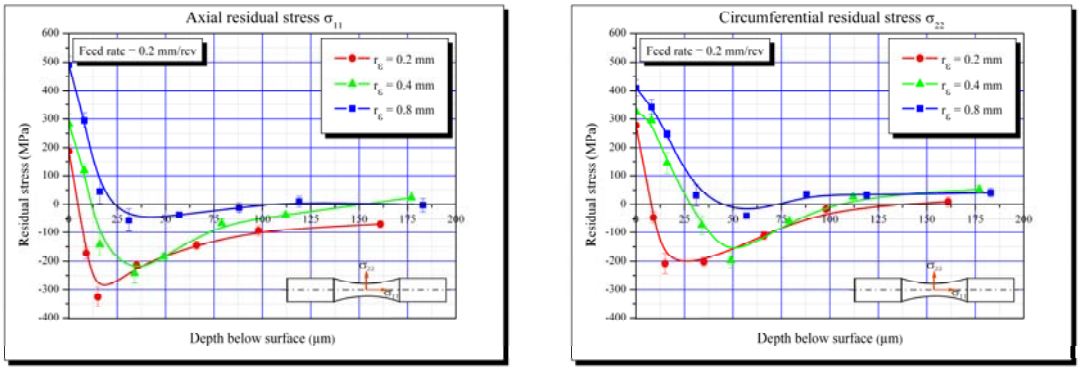

Figure 10.3: Residual stress distributions in turned surface at the same feed rate.

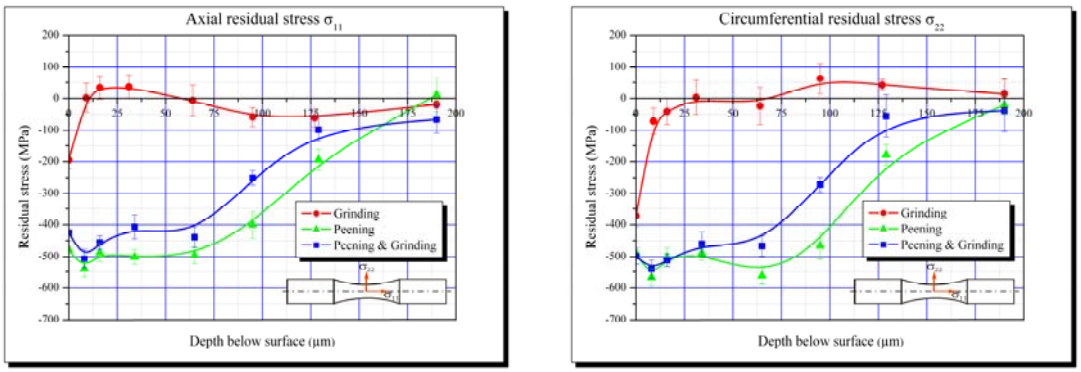

Figure 10.4: Residual stress distributions of ground and peened specimens.

10.3. Appendix C: Uniaxial Tension Testing

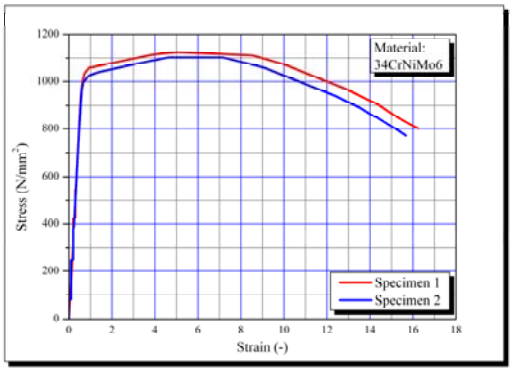

Figure 10.5: Tension stress-strain curve for 34CrNiMo6 steel.

Mechanical Properties			
E	R_e	R_m	A
GPa	MPa	MPa	(%)
205	1045	1115	15.0

Table 10.1: Mechanical properties of 34CrNiMo6 steel.

10.4. Appendix D: Rotating-Bending Fatigue Testing

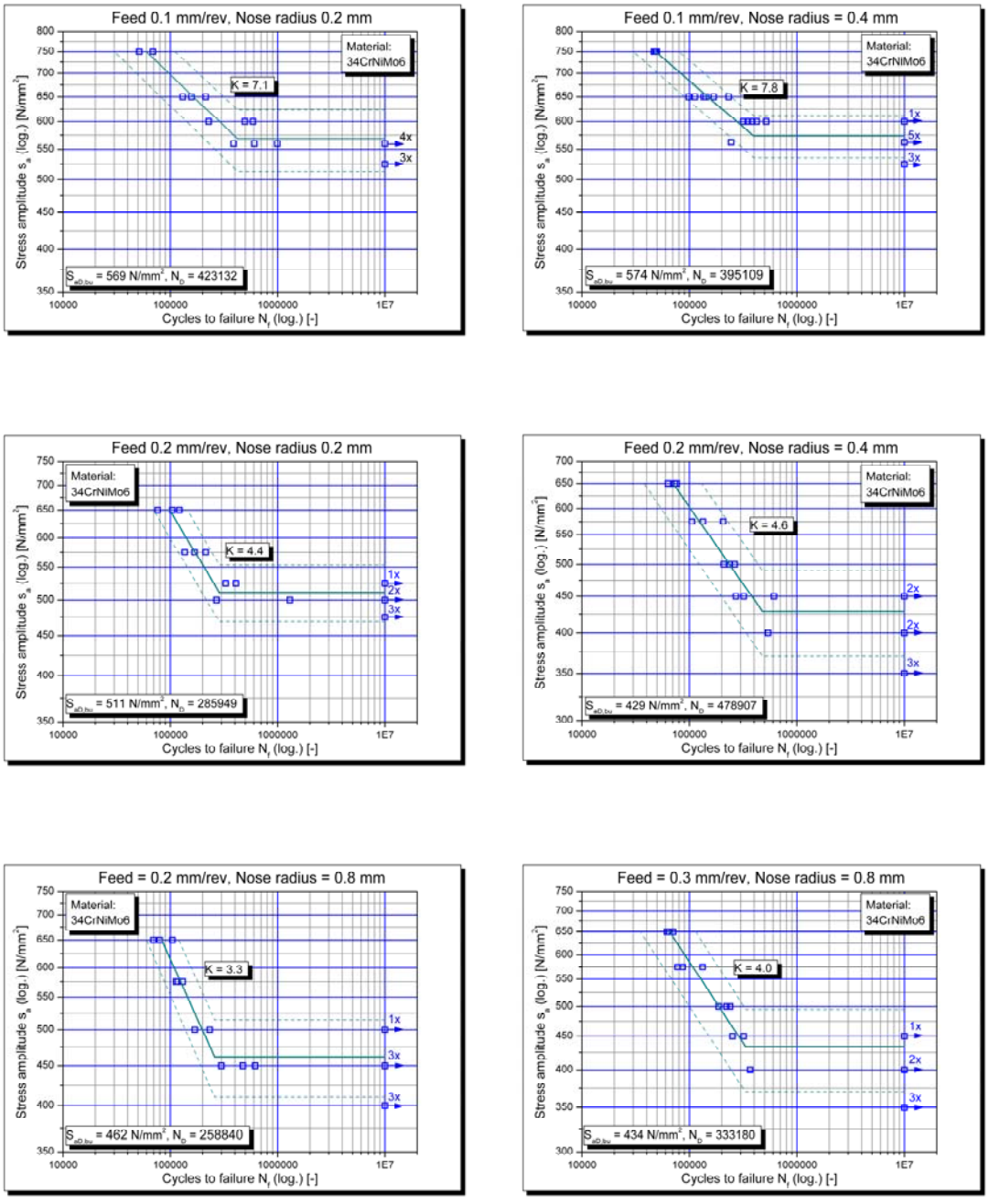

Figure 10.6: Fatigue life of turned specimens with different nose radii and feed rates.

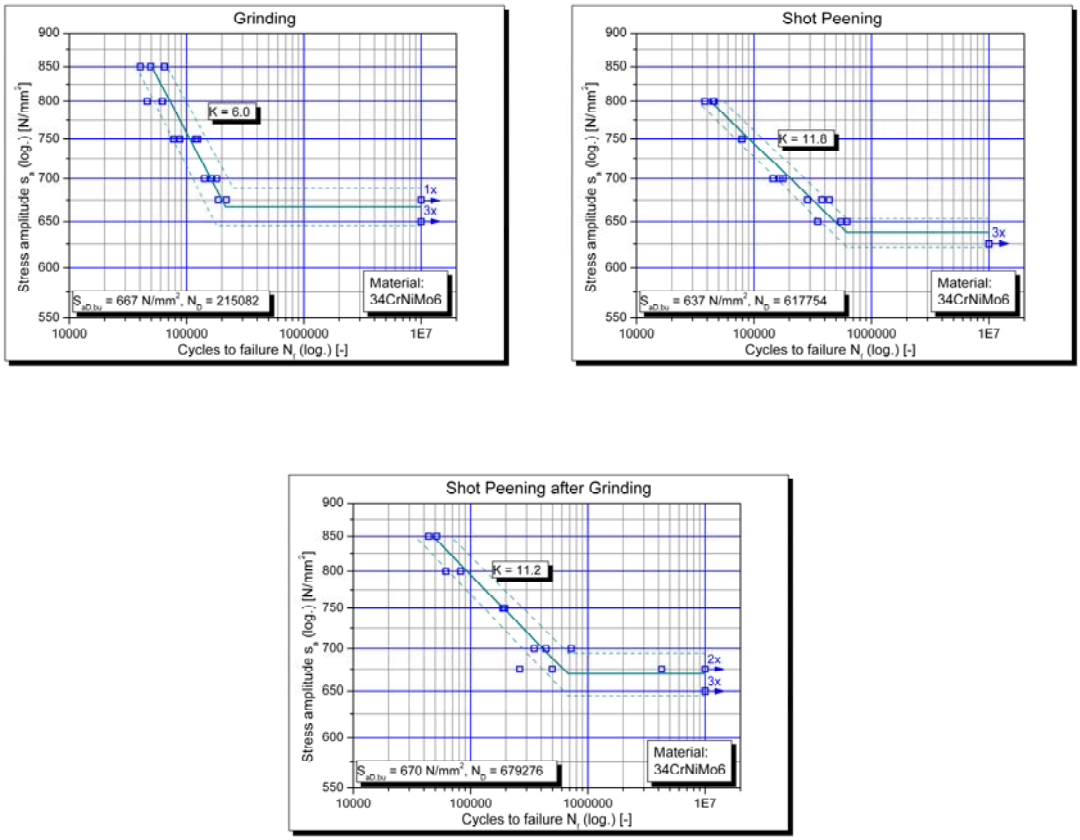

Figure 10.7: Fatigue life of ground and peened specimens.

11. References

[1] M. Field, J.F. Kahles and W.P. Koster, Surface finish and surface integrity, ASM Handbook, Machining, 16 (1989) 19-36.

[2] M. Field and J. Kahles, Review of surface integrity of machined components, Ann. CIRP, 20 (1971) 153-163.

[3] G. Bellows and D.N. Tishler, Introduction to surface integrity, Technical Report TM 70-976, General Electric Company, 1970.

[4] E. Capello, Residual stresses in turning Part I: Influence of process parameters, Journal of Materials Processing Technology, 160 (2005) 221-228.

[5] K.H. Fuh and C.F. Wu, A proposed statistical model for surface quality prediction in end-milling of Al alloy, Int. J. Mash. Tools Manufact., 35(8) (1995) 1187-1200.

[6] R.K. Morton, Topography of surfaces, ASM Handbook, Surface Engineering, 5 (1994) 136-138.

[7] B. Griffiths, Manufacturing surface technology, Surface integrity and functional performance, Penton Press, London, 2001, ISBN 1 8571 8029 1.

[8] J. Peters, P. Vanherck and M. Sastrodinoto, Assessment of surface typology analysis techniques, Ann. CIRP, 28(2) (1979) 539-554.

[9] J.D. Thiele and S.N. Melkote, Effect of cutting edge geometry and workpiece hardness on surface generation in the finish hard turning of AISI 52100 steel, Journal of Materials Processing Technology, 94 (1999) 216-226.

[10] Y.K. Chou and C.J. Evans, Microstructural effects in precision hard turning, Manufacturing Science and Engineering, ASME Bound Volume, MED-Vol., 4 (1996) 237-242.

[11] Y.K. Chou and C.J. Evans, Finish hard turning of powder metallurgy M50 steel, Trns. NAMRI/SME, 25 (1997) 81-86.

[12] D.J. Whitehouse, Handbook of surface metrology, Institute of Physics Publishing, Bristol, 1994.

[13] E. Capello, P. Davoli, G. Bassanini and A. Bisi, Residual stresses and surface roughness in turning, Transactions of the ASME, 121 (1999) 346-351.

[14] H. Sasahara, The effect on fatigue life of residual stress and surface hardness resulting from different cutting conditions of 0.45%C steel, Int. Journal of Machine Tools and Manufacture, 45 (2005) 131-136.

[15] E. Brinksmeier, J.T. Cammett, W. König, P. Leskovar, J. Peters and H.K. Tönshoff, Residual stresses-Measurement and causes in machining processes, Annals of the CIRP, 31(2) (1982) 491-510.

[16] K. Jacobus, R.E. DeVor and S.G. Kapoor, Machining-Induced residual stress-Experimentation and modeling, J. Manufacturing Science and Engineering Transactions of the ASME, 122 (2000) 20-31.

[17] E. Macherauch and K.H. Kloss, Proceedings of the international conference on residual stresses, Garmisch-Partenkirchen, FRG, (1986) 167-174.

[18] M.E. Fitzpatrick and A. Lodini, Analysis of residual stress by diffraction using neutron and synchrotron radiation, Taylor & Francis, London, 2003, ISBN 0 415 30397 4.

[19] E. Zahavi and V. Torbilo, Fatigue Design - Life Expectancy of Machine Parts, CRC Press, Boca Raton, 1996, ISBN 0 8493 8970 4.

[20] M. Tricard, Residual effects of finishing methods, ASM Handbook, Surface Engineering, 5 (1994) 144-151.

[21] F. Gunnberg, M. Escursell and M. Jacobson, The influence of cutting parameters on residual stresses and surface topography during hard turning of 18MnCr5 case carburised steel, Journal of Materials Processing Technology, 174 (2006) 82-90.

[22] P.J. Withers and H.K.D.H. Bhadeshia, Residual stress Part 1 - Measurement techniques, Materials Science and Technology, 17 (2001) 355-365.

[23] G.S. Schajer, Measurement on non-uniform residual stresses using the hole-drilling method, Part I - stress calculation procedures, Journal of Engineering Materials and Technology, Transactions of the ASME, 110 (1988) 338-343.

[24] ASTM standard E837-01, Standard test method for determining residual stresses by the hole-drilling strain gauge method, 2002.

[25] P.V. Grant, J.D. Lord and P.S. Whitehead, The measurement of residual stresses by the incremental hole-drilling technique, Measurement Good Practice Guide No. 53, 2002.

[26] W. Soete and R. Van Crombrugge, An industrial method for the determination of residual stresses, Proceeding SESA, 8(1) (1950) 17-28.

[27] R.A. Kelsey, Measuring non-uniform residual stresses by the hole-drilling method, Proceeding SESA, 14(1) (1956) 181-194.

[28] M. Bijak-Zochowski, A Semidestructive method of measuring residual stresses, VDI-Berichte, 313 (1978) 469-476.

[29] G.S. Schajer, Application of finite element calculations to residual stress measurements, ASME Journal of Engineering Materials and Technology, 103 (1981) 157-163.

[30] A. Niku-Lari, J. Lu and J.F. Flavenot, Measurement of residual stress distribution by the incremental hole-drilling method, Experimental Mechanics, 25(6) (1985) 175-185.

[31] W.E. Nickola, Practical subsurface residual stress evaluation by the hole-drilling method, Proceedings of the Spring Conference on Experimental Mechanics, New Orleans, (1986) 47-58.

[32] M.T. Flaman, B.E. Mills and J.M. Boag, Analysis of stress-variation-with-depth measurement procedures for the residual stress measurement center-hole method of residual stress measurement, Experimental Techniques, 11(6) (1987) 35-37.

[33] G.S. Schajer, Measurement of non-uniform residual stresses using the hole-drilling method. Part II - Practical application of the integral method, ASME Journal of Engineering Materials and Technology, 110 (1988) 344-349.

[34] L.F. Andersen, Residual stresses and deformations in steel structures, PhD thesis, Technical University of Denmark, 2000.

[35] L.F. Andersen, Experimental method for residual stress evaluation through the thickness of a plate, Journal of Engineering Materials and Technology, 124 (2002) 428-433.

[36] I.C. Noyan and J.B. Cohen, Residual stress - Measurement by diffraction and interpretation, Springer Verlag, New York, 1987, ISBN 0 387 96378 2.

[37] W.H. Bragg, W.L. Bragg, Proceedings of the Royal Society of London, Series A, Containing Papers of a Mathematical and Physical Character 88(605) (1913) 443-454.

[38] B.D. Cullity, Elements of X-Ray diffraction, Addison-Wesley Publishing Company Inc., 1978, ISBN 0 201 01174 3.

[39] S.H. Yeo and S.H. Ong, Assessment of the thermal effects on chip surfaces, Journal of Materials Processing Technology, 98(3) (2000) 317-321.

[40] P. Dahlman, F. Gunnberg and M. Jacobson, The influence of rake angle, cutting feed and cutting depth on residual stresses in hard turning, J. Mater. Process. Technol., 147 (2004) 181-184.

[41] B. Scholtes, Residual stresses introduced by machining, Advances in Surface Treatments, 4 (1987) 59–71.

[42] P. Leskovar and J. Peklenik, Influences affecting surface integrity in the cutting process, Annals of the CIRP, 31(1) (1982) 447-450.

[43] R.E. Smallman and R.I. Bishop, Modern physical metallurgy and materials engineering, 6th Edition, Butterworth Heinemann, Oxford, 1999.

[44] A. Cavaleiro and J.T.M. De Hosson, Nanostructured coatings, Springer Science and Business Media, LLC, New York, 2006, ISBN 0 387 25642 3.

[45] W.C. Oliver and G.M. Pharr, Improved technique for determining hardness and elastic modulus using load and displacement sensing indentation experiments, Journal Mater. Res., 7(6) (1992) 1564-1583.

[46] Metallic materials – Instrumented indentation test for hardness and materials parameters, Part 1-3, DIN EN ISO 14577, 2002.

[47] Fischerscope H100C, Operating Manual.

[48] H.H. Behncke, Härte-Technische Mitteilungen 48, 1993.

[49] H.K. Tönshoff, C. Arendt and B. Amor, Cutting of hardened steel, Annals of the CIRP, 49(2) (2000) 547-566.

[50] Y.K. Chou and C.J. Evans, White layers and thermal modeling of hard turned surfaces, Journal of Machine Tools and Manufacture, 39 (1999) 1863-1881.

[51] R. Snoeys, M. Maris and J. Peters, Thermally induced damage in grinding, Annals of the CIRP, 27(2) (1978) 571–581.

[52] W.J. Tomlinson, L.A. Blunt and S. Spraggett, White layers on surface of ground EN24 steel, Surface Engineering, 5(3) (1989) 229–233.

[53] M.C. Shaw and A. Vyas, Heat-affected zones in grinding steel, Annals of the CIRP, 43(1) (1994) 279–282.

[54] P. Kruth, L. Stevens, L. Froyen and B. Lauwers, Study of the white layer of a surface machined by die-sinking electro-discharge machining, Annals of the CIRP, 44(1) (1995) 169–172.

[55] B.J. Griffiths, White layer formations at machined surfaces and their relationship to white layer formations at worn surfaces, Transactions of the ASME, Journal of Tribology, 107(1985) 165–171.

[56] W. König, R. Komanduri, H.K. Tönshoff and G. Ackershott, Machining of hard materials, Annals of the CIRP, 39 (1990) 417–427.

[57] Y. Matsumoto, C.R. Liu and M.M. Barash, Residual stress in the machined surface of hardened steel, High Speed Machining Conference, ASME WAM, (1984) 193–204.

[58] M. Ogata, Einsatz von PCBN-Werkzeugen in der Produktion, VDI Berichte, 762 (1989) 217–279.

[59] H. Tönshoff, H.G. Wobker and D. Brandt, Tribological aspects of hard turning with ceramic tools, Journal of the Society of Tribologists and Lubrication Engineers, 51(2) (1995) 163–168.

[60] H. Tönshoff, H.G. Wobker and D. Brandt, Hard turning - influences on the workpieces properties, Transactions of the NAMRI of SME, 23 (1995) 215–220.

[61] A.M. Abrao and D.K. Aspinwall, The surface integrity of turned and ground hardened bearing steel, Wear, 196 (1996) 279–284.

[62] W. König, A. Berktold and K.F. Koch, Turning vs. grinding, Annals of the CIRP, 42(1) (1993) 39–43.

[63] S. Suresh, Fatigue of materials, Cambridge University Press, Cambridge, 2001, ISBN 0 521 57046 8.

[64] W.A. Wood, Formation of fatigue cracks, Philosophical Magazine, 3 (1958) 692-699.

[65] G.E. Dieter, Mechanical metallurgy, SI Metric Edition, McGraw-Hill Book Company, London, 1988, ISBN 0-07-100406-8.

[66] W.P. Koster and M. Field, Effects of machining variables on the surface and structural integrity of titanium, Proceedings of the North American Manufacturing Research Conference, SME, 2 (1973) 67-87.

[67] E. Siebel and M. Gaier, Influence of surface roughness on the fatigue strength of steels and non-ferrous alloys, A. Ver. Dtsch. Ing., 98 (1956) 1715.

[68] B. Syren, Der Einfluss spanender Bearbeitung auf das Biegewechselverformungsverhalten von Ck 45 in verschiedenen Wärmebehandlungszuständen, PhD Thesis, TU Karlsruhe, 1975.

[69] W.D. Pilkey, Peterson's stress concentration factors, John Wiley & Sons, 1997.

[70] H. Neuber, Kerbspannungslehre, Springer-Verlag, Berlin 1937, 1958 u. 1985 (1., 2. u. 3. Aufl.), engl. Ausgabe: Theory of notch stresses, J.S. Edwards, A. Arbor, Mich., 1946.

[71] P. Kuhn and H.F. Hardraht, An engineering method for estimating the notch-size effect in fatigue tests on steel, NACA Tech. Note 2805, Langley Aeronautical Laboratory, Washington, 1952.

[72] J. Schijve, Fatigue of structures and materials, Kluwer Academic Publishers, Dordrecht, 2001, ISBN 0-7923-7013-9.

[73] R.A. Smith and K.J. Miller, Fatigue cracks at notches, Int. J. Mech. Sci., 19 (1977) 11-22.

[74] N.E. Frost, K.J. Marsh and L.P. Pook, Metal fatigue, Oxford University Press, London, 1974.

[75] R.A. Smith and K.J. Miller, Prediction of fatigue regimes in notched components, Int. J. Mech. Sci., 20 (1978) 201-206.

[76] L. Pook, Metal Fatigue - What it is, why it matters, Springer, London, 2007, ISBN 978-1-4020-5596-6.

[77] H. Kitagawa and S. Takahashi, Applicability of fracture mechanics to very small cracks or the cracks in the early stages, Proc. 2th Int. Conf. Mech. Behav. Mater., Boston, (1976) 627-639.

[78] B. Atzori, P. Lazzarin and G. Meneghetti, Fracture mechanics and notch sensitivity, Fatigue Fract. Engng. Mater. Struct., 26 (2003) 257-267.

[79] D. Radaj, Ermüdungsfestigkeit, Grundlagen für Leichtbau, Maschinen- und Stahlbau, Springer, Berlin, 2003, ISBN 3-540-44063-1.

[80] J. Liu, Dauerfestigkeitsberechnung metallischer Bauteile, Habilitationsschrift TU Clausthal, 2001.

[81] Y. Matsumoto, F. Hashimoto and G. Lahoti, Surface integrity generated by precision hard turning, Annals of the CIRP, 48(1) (1999) 59-62.

[82] D. Löhe, K.H. Lang and O. Vöhringer, Residual stresses and fatigue behavior , ASM Handbook of Residual Stress and Deformation of Steel, Ohio, 2002, ISBN 0-87170-729-2.

[83] B. Scholtes, Residual stresses generated by mechanical surface treatments, DGM Informationsgesellschaft, in German, Oberursel, 1990, ISBN 3-88355-170-8.

[84] J.F. Flavenot and N. Skalli, A comparison of multiaxial fatigue criteria incorporating residual stress effects, Biaxial and Multiaxial Fatigue, EGF 3 (Edited by M.W. Brown and K.J. Miller), Mechanical Engineering Publications, London, (1989) 437-457.

[85] V.V. Novozhilov, Theory of elasticity, (Translated from Russian by J.K. Lusher), Pergamon Press, London, 1961, ISBN 0-486-40684-9.

[86] A. Simbürger, Festigkeitsverhalten zäher Werkstoffe bei einer mehrachsigen phasenverschobenen Schwingbeanspruchung mit körperfesten und veränderlichen Hauptspannungsrichtungen, LBF-Bericht Nr. FB-121, Laboratorium für Betriebsfestigkeit, Darmstadt, 1975.

[87] H. Zenner, R. Heidenreich and I. Richter, Schubspannungsintensitätshypothese, Erweiterung und experimentelle Abstützung einer neuen Festigkeitshypothese für schwingende Beanspruchung, Konstruktion, 32 (1980) 143-152.

[88] H. Zenner and I. Richter, Eine Festigkeitshypothese für die Dauerfestigkeit bei beliebigen Beanspruchungskombinationen, Konstruktion, 29 (1977) 11-18.

[89] J. Liu, Beitrag zur Verbesserung der Dauerfestigkeitsberechnung bei mehrachsiger Beanspruchung, PhD thesis, Technical University of Clausthal, 1991.

[90] J. Liu and H. Zenner, Fatigue limit of ductile metals under multiaxial loading, Proc. of the 6th Int. Conf. on Biaxial/Multiaxial Fatigue and Fracture, Lisbon, (2001) 147-164.

[91] J. Liu, Weakest link theory and multiaxial criteria, Proc. of the 5th Int. Conf. on Biaxial/Multiaxial Fatigue and Fracture, Cracow, (1997) 45-62.

[92] A. Troost and E. El-Magd, Allgemeine quadratische Versagensbedingung für metallische Werkstoffe bei mehrachsiger schwingender Beanspruchung, Metall, 31. Jahrgang, 7 (1977) 759-764.

[93] A. Troost and E. El-Magd, Allgemeine Formulierung der Schwingfestigkeitsamplitude in Haighscher Darstellung, Materialprüfung, 17(2) (1975) 47-49.

[94] J. Goodman, Mechanics applied to engineering, Longmans, Green & Co., New York, 1899.

[95] W. Gerber, Bestimmung der zulässigen Spannungen in Eisenkonstruktionen, Z. d. Bayerischen Architekten u. Ingenieurvereins, 6(6) (1874) 101-110.

[96] H. Dietmann, Festigkeitsberechnung bei mehrachsiger Schwingbeanspruchung, Konstruktion, 25(5) (1973) 181-189.

[97] E. El-Magd and S. Mielke, Dauerfestigkeit bei überlagerter zweiachsiger statischer Beanspruchung, Konstruktion, 29(7) (1977) 253-257.

[98] G.E. Totten, M. Narazaki, R.R. Blackwood and L.M. Jarvis, Failures related to heat treating operations, ASM Handbook, Failure Analysis and Prevention, 11 (2002) 192-223.

[99] H.K.D.H. Bhadeshia and R.W.K. Honeycombe, Steels - Microstructure and properties, 2006, ISBN 978-0-750-68084-4.

12. Publications

I. The effect of machining on the surface integrity and fatigue life
Ataollah Javidi, Ulfried Rieger, Wilfried Eichlseder
International Journal of Fatigue 30 (2008) 2050–2055

II. Estimating the surface fatigue factor of different surface finishes to predict the fatigue strength
Ataollah Javidi, Ulfried Rieger, Wilfried Eichlseder
Submitted for Publication

III. Fatigue strength prediction of different surface finishes in the presence of residual stresses
Ataollah Javidi, Ulfried Rieger, Wilfried Eichlseder
Submitted for Publication

Publication I

THE EFFECT OF MACHINING ON THE SURFACE INTEGRITY AND FATIGUE LIFE

Ataollah Javidi, Ulfried Rieger, Wilfried Eichlseder

International Journal of Fatigue 30 (2008) 2050–2055

THE EFFECT OF MACHINING ON THE SURFACE INTEGRITY AND FATIGUE LIFE

Ataollah Javidi, Ulfried Rieger, Wilfried Eichlseder

Department of Mechanical Engineering, University of Leoben, Franz-Josef-Straße 18, 8700 Leoben, Austria

Abstract

Steel components often have to be machined after heat treatment in order to obtain the correct shape as well as the required surface finish. Surface quality influences characteristics such as fatigue strength, wear rate, corrosion resistance, etc. Hard turning allows manufacturers to simplify their processes and still achieve the desired surface finish quality. There are various parameters such as cutting speed, feed rate, and tool nose radius that are known to have a large impact on surface quality. This paper describes how feed rate and nose radius affect the surface integrity and fatigue life in turning. The results show that the effect of residual stress on fatigue life is more pronounced than the effect of surface roughness. The goal of this work is to identify a relationship between surface quality, turning process parameters and fatigue behavior of 34CrNiMo6.

Keywords: Surface integrity, Machining, Fatigue life

1. Introduction

The fatigue life of a machined part depends strongly on its surface condition. It has long been recognized that fatigue cracks generally initiate from free surfaces. This is due to the fact that surface layers experience the highest load and are exposed to environmental effects. Stress concentration, oxidation, and burning out of alloy elements (at high operational temperatures) are the factors acting upon the surface layers that contribute to crack initiation. Crack initiation and propagation, in most cases, can be attributed to surface integrity produced by machining [1]. The surface of a part has two important aspects that must be defined and controlled. The first aspect are geometric irregularities on the surface, and secondly the

metallurgical alterations of the surface and the surface layer. This second aspect has been termed surface integrity. Field and Kahles [2] describe surface integrity as the relationship between surface geometric values and the physical properties such as residual stress, hardness and microstructure of the surface layers. Surface integrity influences the quality of the machined surface and subsurface, which both become extremely significant when manufacturing structural components that have to withstand high static and dynamic stresses. Tönshoff et al. [3] and several other authors [4–12] have reported how hard turning influences the surface integrity of a machined part [13]. Surface integrity was suggested to indicate the surface characteristics (microstructure, hardness, surface roughness, residual stress) that influence the part functionality. Among these characteristics, residual stresses play a key role. The residual stresses left by the turning operation depend both on the type of material being machined and on turning parameters [14]. There are various parameters such as cutting speed, feed rate, and tool nose radius that are known to have a large impact on surface quality [15-17]. Therefore it is important to gain better understanding how the finishing process affects the functional behavior of the machined parts. The goal of this work is to identify a relationship between surface integrity, turning process parameters and fatigue behavior of 34CrNiMo6.

2. Material and experimental set-up

The material used for the cutting and fatigue life tests was a 0.34% carbon steel. Steel bars of the type 34CrNiMo6 (quenched and tempered) used in this investigation had been heat treated to obtain a tensile strength of 1100 MPa. The micrograph of the bar feedstock (cross-section A-A, Fig. 3) is presented in Fig. 1, which shows that the microstructure is composed of bainite.

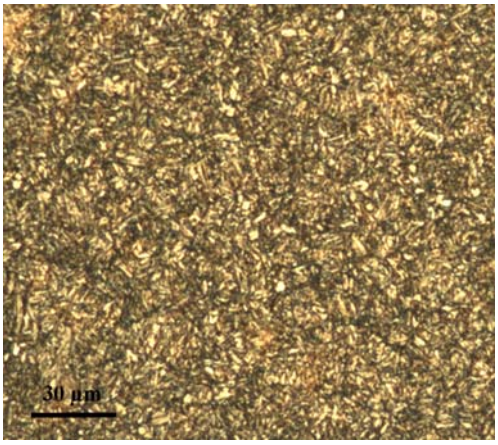

Fig. 1: Confocal scanning laser micrograph of the bar feedstock.

The chemical composition and mechanical properties of this steel are given in Tab. 1.

Steel	Chemical composition (%)					Mechanical properties		
	C	Mn	Cr	Ni	Mo	R_e	R_m	A
34CrNiMo6	0.36	0.64	1.52	1.44	0.15	1085	1100	17.0

Tab. 1: Chemical composition and mechanical properties of 34CrNiMo6.

The test specimens were machined by turning in wet condition. Turning was performed using inserts DCMT 11 T3 02, 04, 08 4025 from Sandvik. The three inserts differ from each other in nose radius r_ε. An ordinary stable two-axes CNC lathe (Mori Seiki SL 25 2001) was used for longitudinal turning of the specimens. The cutting conditions employed for the samples are shown in Tab. 2.

Feed rate (mm/rev.)	0.05, 0.1, 0.2, 0.3, 0.4
Nose radius (mm)	0.2, 0.4, 0.8
Depth of cut (mm)	0.5
Cutting speed (m/min.)	80

Tab. 2: Cutting conditions.

Residual stresses were measured by means of the blind hole drilling method. The basic hole drilling procedure involves drilling a small hole into the surface of a component, at the center of a strain gauge rosette and measuring the relieved strains. The residual stresses originally present at the hole location are calculated from these strain values. In the hole

drilling procedure, a three-element residual stress strain gauge rosette (EA-06-062RE-120 of MM series) is bonded to the surface of the specimen. The strain gauges are then connected to a suitable strain indicator. A hole drilling rig, which is shown in Fig. 2, was used for this purpose.

Fig. 2: Hole drilling rig.

It uses a small milling tool (about 1.6 mm diameter) mounted on an air turbine reaching a rotational speed of about 300000 r/min. The drilling device is equipped with an optical microscope to accurately center the hole in the middle of the rosette. Depth increments of 127 μm were used in the near-surface layer. For each incremental step, the strains were acquired until the variation with depth become constant. The holes were drilled to a depth of about
1.27 mm.

Nose radius of the tool and feed rate were varied for this investigation. The microhardness, surface roughness and residual stress of the specimens were measured before the fatigue life test. Fig. 3 shows the configuration of the bar feedstock and fatigue test specimen before and after test.

Fig. 3: Bar feedstock and fatigue test specimen.

3. Results and discussion

3.1. Metallographic examination of machined surface

Machining influences the conditions of the subsurface microstructure, which was examined under a confocal scanning laser microscope (LEXT) in etched condition. Selections of the etched subsurface microstructures generated during cutting are illustrated in Fig. 4 and Fig. 5. Fig. 4 illustrates the LEXT longitudinal-sectional viewgraph (marked as B-B, in Fig. 3) with a very thin localized plastic deformation zone of about 3 – 4 µm while using different feeds and nose radii with the same cutting speed as given in Tab. 2.

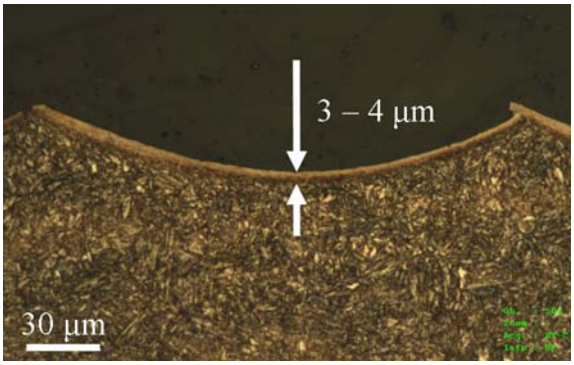

Fig. 4: Localized plastic deformation zone beneath machined surface.

A scanning electron microscope image (SEM, Fig. 5) of the layer underneath the machined surface shows that the grain boundaries tend to deform in the direction of feed due to the high temperature and force generated during hard turning. Region A indicates that the original grains are no longer discernible.

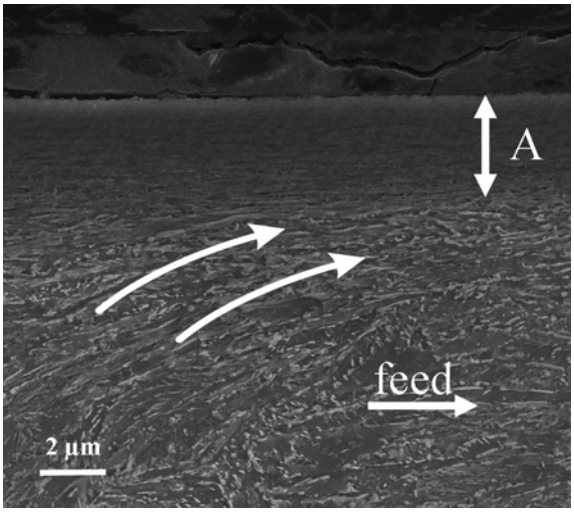

Fig. 5: SEM image of the layer underneath the machined surface.

Clearly, the above observations indicate that high plastic deformation was generated after machining.

3.2. Microhardness analysis of the produced surface

In order to identify more clearly the extent of the alterations in the subsurface microstructure, the change of the subsurface microhardness was measured with an automated microhardness tester (Fischerscope® H100C) equipped with a Vickers indenter and a

continuously applied load of 100 mN. The device measures the universal hardness according to ISO 14577. Fig. 6 shows the indentation arrangement at different positions beneath the machined surface.

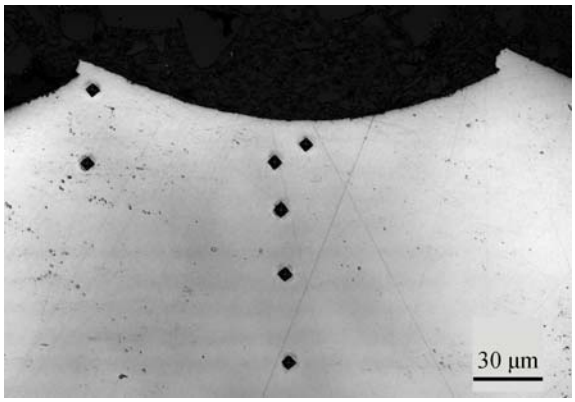

Fig. 6: Indentation arrangement beneath the machined surface (f = 0.2, r_ε = 0.2).

Fig. 7 details the variation of the microhardness with the depth beneath the machined surface produced by different cutting conditions as shown in Tab.2. The analysis of the results presented in Fig. 7 shows that there is no significant variation in hardness.

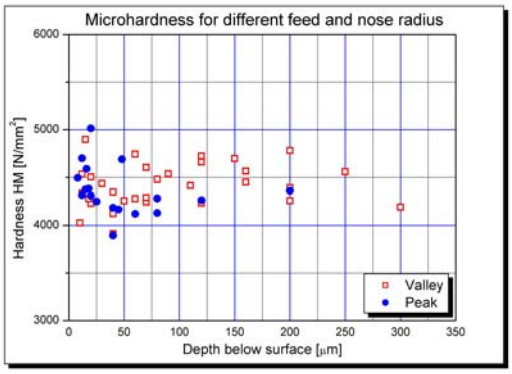

Fig. 7: Microhardness variations beneath the machined surface.

3.3. Surface roughness measurements

The surface roughness of the machined part is largely determined by the feed and tool nose radius. A large feed will give shorter cutting times but a poor surface finish. A large nose radius will generate a better surface finish but an excessively large nose radius can lead to

vibration tendencies, unsatisfactory chipbreaking and shorter tool-life because of insufficient cutting edge engagement. In practice, therefore, the size of the insert nose radius and the feed may be limited in an operation. The geometric contribution of tool nose radius and tool feed, shown in Fig. 8, is also called theoretical surface roughness.

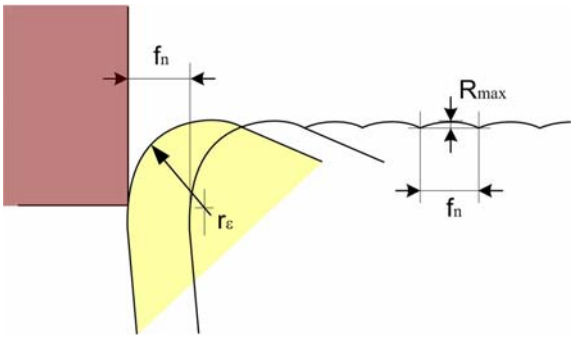

Fig. 8: Illustration of roughness on the finished surface.

A basic theoretical model for surface roughness is approximated by the following Eq. (1):

$$R_{\max} = \frac{f^2}{8 \times r_\varepsilon} \qquad \text{Eq. (1)}$$

where f is feed rate (mm / rev.) and r_ε is the tool nose radius (mm).
According to this model, one needs only to decrease the feed rate or to increase the tool nose radius to improve desired surface roughness. Tool vibration and chip adhesion are such effects that lead to the degradation of surface roughness in this model.

After the turning operation, the part surface finish was measured using laser scanning microscopy. Fig. 9 shows a 3D topographic map of the machined surface.

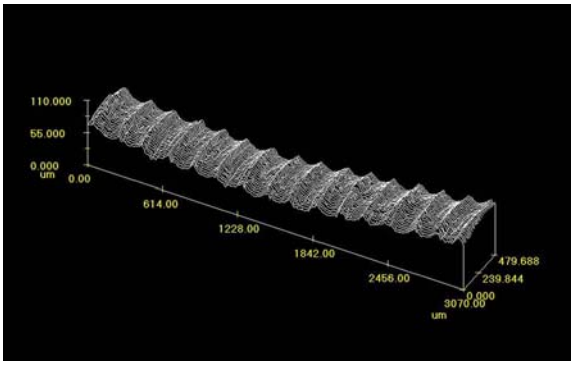

Fig. 9: 3D topographic map of machined surface.

In this investigation, the part surface finish was assessed by means of the surface roughness parameter R_{max}. A schematic description of this parameter for an arbitrary machined surface is shown in Fig. 10.

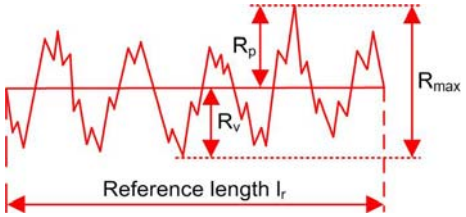

Fig. 10: A schematic illustration of surface roughness parameter, R_{max}.

Note that R_{max} (the maximum height of roughness) describes the sum of the maximum peak height R_p and the maximum valley depth R_v of the contour curve at the reference length. The experimental investigation was performed using different nose radii and feed rates. The surface roughness measurements were repeated at least 5 times for each specimen. Fig. 11 shows that the actual surface roughness does not match the theoretical surface roughness and Eq. (2) describes the relationship between real and theoretical surface roughness for the cutting conditions from Tab. 2.

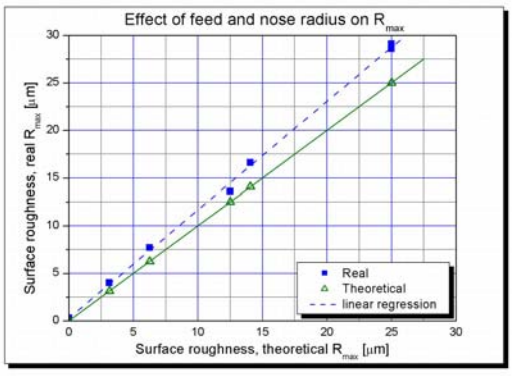

Fig. 11: Real and theoretical surface roughness.

$$R_{\max(\text{Real})} = 1.14 \times R_{\max(\text{Theoretical})} + 0.3 \qquad \text{Eq. (2)}$$

Fig. 12 illustrates the effect of the nose radius on the surface roughness for the cutting condition employed for the fatigue test (f = 0.2, r_ε = 0.2, 0.4, 0.8).

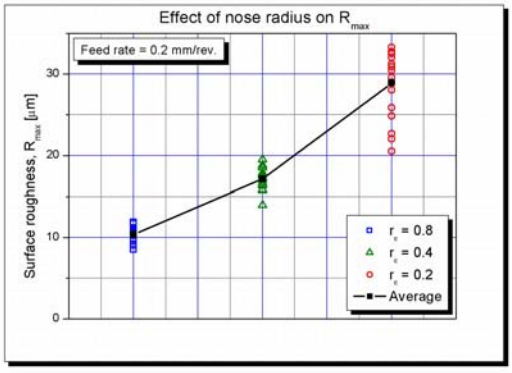

Fig. 12: Effect of nose radius on R_{max}, feed rate = 0.2 mm/rev.

The results present that the value of R_{max} parameter obtained for the samples increases with decreasing the nose radius r_ε.

3.4. Residual stress measurements

After the turning operation, the residual stresses were measured using the blind hole drilling method. The machining of round samples was carried out with different feed rates f and nose radii r_ε. Fig. 13 shows the distribution of the residual stress of the machined surface

measured by this method. Measurements were taken along the circumference and axial directions. Residual stress along the axial direction was expected to affect the rotating bending fatigue life of the specimens.

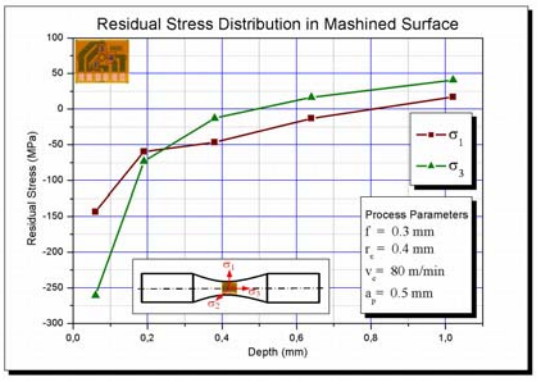

Fig. 13: Residual stress distribution in machined surface.

In this study, the integral method is examined as a procedure for determining non-uniform residual stress fields using strain relaxation data from the hole drilling method. In the integral method, the contributions of the total measured strain relaxations at all depths are considered simultaneously and this provides an evaluation of residual stress within each increment of depth. A description of this method can be found in Schajer [18]. Fig. 14 and Fig. 15 show the average value of stresses over a depth range from 0 to 0.127 mm for specimens with different process parameters. All occurring stresses are compressive.

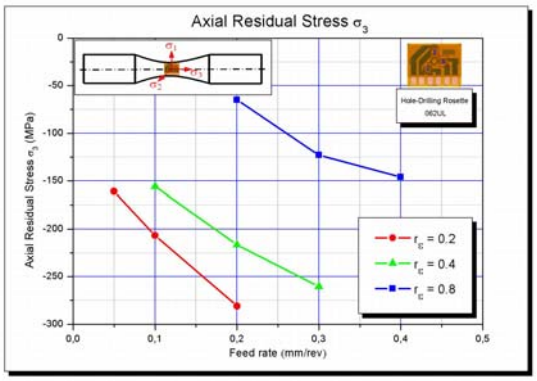

Fig. 14: Axial residual stress σ_3 versus feed rate.

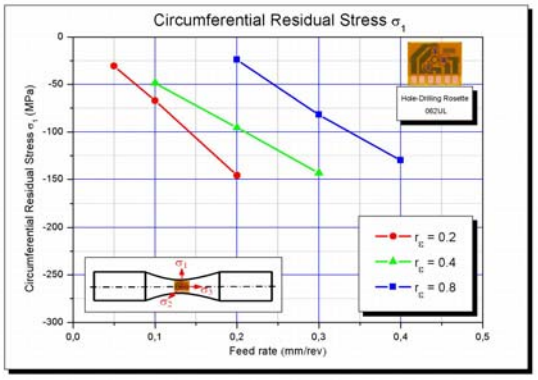

Fig. 15: Circumferential residual stress σ_1 versus feed rate.

It can be seen that an increase of feed rate causes an increase of compressive stresses in both directions. On the other hand, an increase of the nose radius of the insert causes a decrease of the compressive residual stresses.

4. Influences on fatigue life

The rotating bending fatigue tests that were performed on the test specimens as per the cutting conditions shown in Tab. 3.

Feed rate (mm/rev.)	0.2
Nose radius (mm)	0.2, 0.4, 0.8
Depth of cut (mm)	0.5
Cutting speed (m/min.)	80

Tab. 3: Cutting condition employed for fatigue test.

Rotation speed was 3800 rev/min. At least sixteen specimens were used to verify the fatigue life for every combination of feed and nose radius. When the number of rotation exceeded 10^7 the test was stopped, which means the test specimen will not break under that condition (test-piece run out). Fig. 16 shows the relationship between cutting condition and fatigue life.

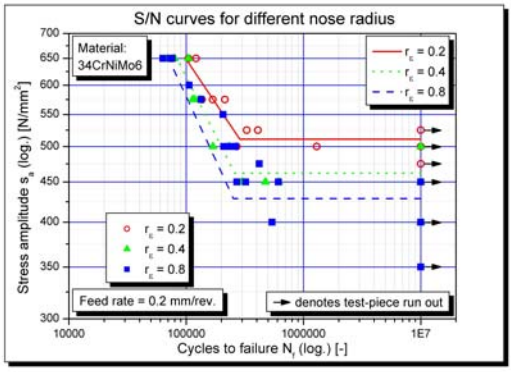

Fig. 16: Fatigue life of turned specimens with different nose radius.

Although the surface roughness of specimens with r_ε = 0.2 is higher than turned specimens with r_ε = 0.4 and 0.8, the results show that the specimens with a nose radius of r_ε = 0.2, have a higher fatigue life than specimens with 0.4 and 0.8 mm nose radius. That means a higher compressive residual stress causes a higher fatigue life and the effect of residual stress on fatigue life is more than the effect of surface roughness.

5. Conclusion

This work presents an experimental study on the relationship between surface integrity, turning process parameters and fatigue behavior of 34CrNiMo6. The following conclusions can be drawn:

1. The plastic deformation of the grain boundaries was found at the first 3 – 4 μm of the subsurface layer after machining.

2. No significant variation in hardness was observed beneath the machined surface produced by different cutting conditions.

3. Surface roughness at the same feed rate becomes higher when a small nose radius is used.

4. The residual stress induced by the turning process tends to become more compressive as the feed rate increases. On the other hand, an increase of the nose radius of the insert

causes a decrease of the compressive residual stresses. Thus it is evident that the feed rate and nose radius are the key parameters that control residual stress in turning.

5. It can be seen that an increase of compressive residual stress causes an increase of fatigue life.

Acknowledgements

This work was supported by the Austrian Aeronautics Research. The authors would like to thank Robert Schreiber and his team (Pankl Drivetrain Systems GmbH) for the support in sample machining.

References

[1] Zahavi E., Torbilo V., Fatigue design - Life expectancy of machine parts, CRC Press, 1996.

[2] Field M., Kahles J., Review of surface integrity of machined components, Ann. CIRP 20 (1971) 153–163.

[3] Tönshoff H.K., Arendt C., Ben Amor R., Cutting of hardened Steel, Ann. CIRP 49 (2) (2000) 547–566.

[4] Liu C.R., Mittal S., Optimal pre-stressing the surface of a component by superfinish hard turning for maximum fatigue life in rolling contact, Wear 219 (1998) 128–140.

[5] Matsumoto Y., Hashimoto F., Lahoti G., Surface integrity generated by precision hard turning, Ann. CIRP 48 (1999) 59–62.

[6] Jacobson M., Surface integrity of hard-turned M50 steel, in: Proceedings of the Institution of Mechanical Engineers, Part B, J. Eng. Manuf. 216 (1) (2002) 47–54.

[7] Jacobson M., Patrik D., Fredrik G., Cutting speed influence on surface integrity of hard turned bainite steel, J. Mater. Proc. Technol. 128 (1–3, 6) (2002) 318–323.

[8] Thiele J.D., Melkote S.N., Effect of cutting edge geometry and workpiece hardness on surface generation in the finish hard turning of AISI 52100 steel, J. Mater. Proc. Technol. 94 (1999) 216–226.

[9] Brinksmeier E., Cammett J.J., Leskovar P., Peters J., Tönshoff H.K., Residual stresses-measurements and causes in machining processes, Ann. CIRP 31 (1982) 491–510.

[10] Vomacka P., Walburger H., Residual stresses due to hardmachining industrial experiences, in: Proceedings of the 5th European Conference on Residual stresses, Switzerland, 2000, pp. 592–597.

[11] König W., Berktold A., Koch K-F., Turning versus grinding: a comparison of surface integrity aspects and attainable accuracies, Ann. CIRP 42 (1993) 39–43.

[12] Tönshoff H.K., Wobker H.-G., Brandt D., Potential and limitation of hard turning, SME Tech. Papers (1995) MR95–MR215.

[13] Gunnberg F., Escursell M., Jacobson M., The influence of cutting parameters on residual stresses and surface topography during hard turning of 18MnCr5 case carburised steel, J. Mater. Proc. Technol. 174 (2006) 82-90.

[14] Capello E., Residual stresses in turning Part I: Influence of process parameters, J. Materials Processing Technology 160 (2005) 221-228.

[15] Dahlman P., Gunnberg F., Jacobson M., The influence of rake angle, cutting feed and cutting depth on residual stresses in hard turning, J. Materials Processing Technology 147 (2004) 181-184.

[16] Arola D., Williams C.L., Estimating the fatigue stress concentration factor of machined surface, International Journal of Fatigue 24 (2002) 923-930.

[17] Sasahara H., The effect on fatigue life of residual stress and surface hardness resulting from different cutting conditions of 0.45%C steel, J. Machine Tools and Manufacture 45 (2005) 131-136.

[18] Schajer G.S., Measurement of non-uniform residual stresses using the hole drilling method, part I – Stress calculation procedures, ASME Journal of Engineering Materials and Technology 110 (1988) 338-343.

Publication II

ESTIMATING THE SURFACE FATIGUE FACTOR OF DIFFERENT SURFACE FINISHES TO PREDICT THE FATIGUE STRENGTH

Ataollah Javidi, Ulfried Rieger, Wilfried Eichlseder

Submitted for Publication

ESTIMATING THE SURFACE FATIGUE FACTOR OF DIFFERENT SURFACE FINISHES TO PREDICT THE FATIGUE STRENGETH

Ataollah Javidi, Ulfried Rieger, Wilfried Eichlseder

Department of Mechanical Engineering, University of Leoben, 8700 Leoben, Austria

Abstract

In this study the effect of surface topography on the fatigue strength of a quenched and tempered steel was evaluated in terms of the surface stress concentration, the effective surface roughness and the surface stress singularity. In order to produce a range of surface topography, test specimens were given a variety of surface conditions using different types of surface finish methods. The surface topography resulting from manufacturing processes was characterized using a confocal scanning laser microscope (LEXT) and the Liu model was used to estimate the surface fatigue factor for different surface finishes. A modification of the Liu model is proposed by the authors to take into account the influence of surface stress singularity. The specimens were subjected to rotating bending fatigue to failure and changes in the fatigue strength limit resulting from the surface topography were assessed throughout the stress-life regime ($10^3 \leq N_f \leq 10^7$cycles). It was found that the fatigue life is surface topography dependent and the effect of residual stress introduced by the finishing processes for the evaluation of the fatigue strength must be examined.

Keywords: Fatigue notch factor, Surface topography, Fatigue strength

Nomenclature

A	elongation to failure	a	notch or crack size
B	spacing between two notches	a_0	characteristic structural length
F_S	surface fatigue factor	b	notch pitch
K_f	fatigue notch factor	f	feed rate
K_I	mode I stress intensity factor	n	stress state
K_t	stress concentration factor	r_ε	tool nose radius
L	reference length	s	geometrical factor
N_f	number of cycles to failure	t	height of surface irregularities
R	stress ratio	t_0	crack length
R^2	regression coefficient	$z(x)$	profile height distribution
R_a	average roughness	ΔK	stress intensity factor range
R_e	yield strength	ΔK_{th}	threshold stress intensity factor
R_{eff}	effective surface roughness	γ	degree of singularity
R_m	tensile strength	λ	ratio between spacing & height
R_p	maximum peak height	ρ	notch root radius
R_v	maximum valley depth	ρ^*	material constant
R_y,R_{max}	Peak-to-valley height	σ_a	stress amplitude
R_z	10-point surface height	σ_W	intrinsic fatigue strength
Y_0	geometric correction factor	φ	notch opening angle

1. Introduction

The calculation of the fatigue strength for the development of structural components has become more important in recent years. In order to save time and cost, it is attempted to limit the experimental strength testing and to calculate the fatigue strength from material data. The fatigue strength of smooth, polished material specimens can be estimated or obtained from the corresponding fatigue charts with high accuracy. However, the results of fatigue strength determinations on material specimens cannot be directly applied to real components. This is because there are various parameters such as geometry and size, mean stress, type of load, multiaxiality, surface layer/integrity (surface topography, residual stresses, hardness, microstructure), temperature, corrosive media, etc that have a large impact on fatigue strength of structural components [1-5]. The effect of these parameters on the fatigue strength of components is complex and causes difficulty in its evaluation with respect to the fatigue strength of material specimens. In this study the effect of surface topography on the high cycle fatigue life of 34CrNiMo6 was examined using a variety of surface finishes. The fatigue strength for the different surface finishes was estimated by means of experimental results from the rotating bending fatigue tests.

2. Background

As fatigue cracks mostly initiate at the free surface of a component, the condition of the surface resulting from manufacturing process is an important consideration in controlling the fatigue strength. The effect of surface finish has been studied by many researchers and it has been recognized that the most significant parameter categorizing the quality of a machined surface from the fatigue point of view is the maximum depth of the surface irregularities which can be obtained from the surface profile scan [6-20]. Siebel and Gaier [21], for instance, compared fatigue strength with the maximum depth of surface irregularities, measured by a surface roughness scan, and found a critical depth below which there was no change in fatigue strength and above which there was a linear fall in fatigue strength. The effect of surface roughness on the fatigue strength is considered by the appropriate factor to correct the endurance limit [22-24]. The surface correction factor is often represented by surface roughness parameters such as R_a (the roughness average) and R_y or R_{max} (peak-to-valley height roughness) of the component surface topography. These parameters are defined with reference to the profile height distribution $z(x)$ recorded over an assessment length L. Eq. (1) shows the definition of R_a.

$$R_a = \frac{1}{L}\int_0^L \left| z(x) \right| dx \qquad \text{Eq. (1)}$$

A schematic description of this parameter for a machined surface is shown in Fig. 1.

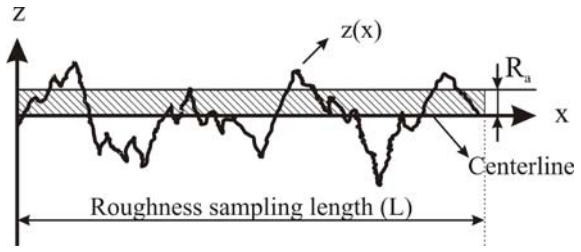

Fig. 1: Arithmetical average roughness, R_a.

Although the standard surface roughness parameters provide a simple and useful means of quantifying profile height distributions, which are important for estimating fatigue strength, they are, however, relatively insensitive to specific features of the surface height distribution.

This problem was investigated by Syren [25] and the results of his work show that not only the maximum depth of surface irregularity but also the whole surface topography influences the fatigue strength (Fig. 2, Tab. 1).

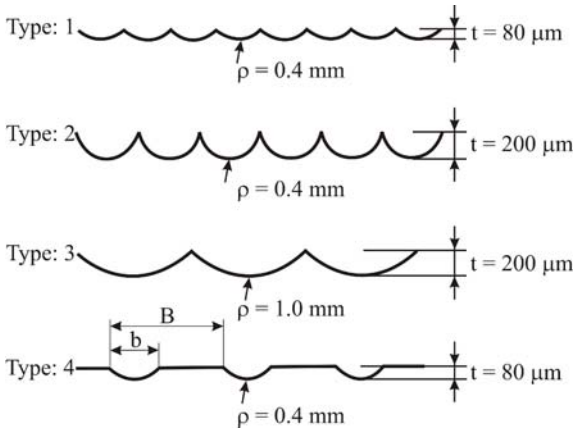

Fig. 2: The influence of surface topography on the fatigue strength, according to Syren [25].

Type	ρ [mm]	t [µm]	t/ρ	B/b	$K_{t,\,Liu}$	σ_a [MPa]
1	0.4	80	0.2	1	1.45	210
2	0.4	200	0.5	1	1.71	185
3	1.0	200	0.2	1	1.45	205
4	0.4	80	0.2	>>1	1.90	170

Tab. 1: Fatigue results according to Syren [25], K_t has been estimated by Eq. (8).

Tab. 1 shows that the turned surface profiles for type 1 and 2 have the same profile valley radii ρ and different height amplitudes t whilst the fatigue strength σ_a decreases with an increase of the surface roughness. It can also be seen that the turned surface profiles for type 2 and 3 have the same height amplitudes but the type 2 profile is much more detrimental to fatigue life due to the small profile valley radius. This means that the standard surface roughness parameters should not be used on an individual basis for evaluating the effect of surface finish on fatigue strength. Therefore it is necessary to express the relationship between surface topography and fatigue strength with other parameters such as the fatigue strength reduction factor of the notched specimen, K_f. This factor plays a key role in predicting the fatigue strength or fatigue life.

Kuhn et al. [26] explained K_f as the ratio of the fatigue strength of a smooth specimen to the fatigue strength of a notched specimen under the same experimental conditions and the same number of cycles. The limiting condition proposed for K_f is explained as $1 \leq K_f \leq K_t$.

The fatigue notch factor is dependent on many parameters such as size and geometry, stress gradient, material properties and loading type.

Weixing et al. [27] have reviewed the expressions for the fatigue notch factor and classified them into three types: the average stress model, the fracture mechanics model and the stress field intensity model. These expressions were compared based on the fatigue mechanism and experimental results. Neuber [28], Peterson [29] and Heywood [30] have proposed classical approaches for defining K_f based on the average stress model instead of the peak stress. Eq. (2) shows the proposed formulation for K_f by Neuber [28] where ρ^* is a material constant correlated experimentally to the ultimate tensile strength.

$$K_f = 1 + \frac{K_t - 1}{1 + \sqrt{\frac{\rho^*}{\rho}}} \qquad \text{Eq. (2)}$$

Note that the material constant ρ^* is dependent only on the ultimate strength and does not include fracture mechanics constants. In order to make a connection between fatigue limit and fracture mechanics constants such as fatigue threshold, El-Haddad et al. [31] proposed an asymptotic solution that is able to explain the transition between fatigue limit towards fatigue threshold by means of defining the material constant a_0 Eq. (9).

Ciavarella et al. [32] showed that the classical formulation for K_f has limitations when their asymptotic behavior is considered and thus presented the modified equations for K_f to include the fatigue threshold dependence Eq. (3).

$$K_f = 1 + \frac{K_t - 1}{1 + \frac{K_t - 1}{\sqrt{\frac{a}{a_0}}}} \quad \text{(Neuber modification)} \qquad \text{Eq. (3)}$$

They also showed that only the Neuber formula has a correct functional form in the entire range of notch sizes and shapes (Fig. 3).

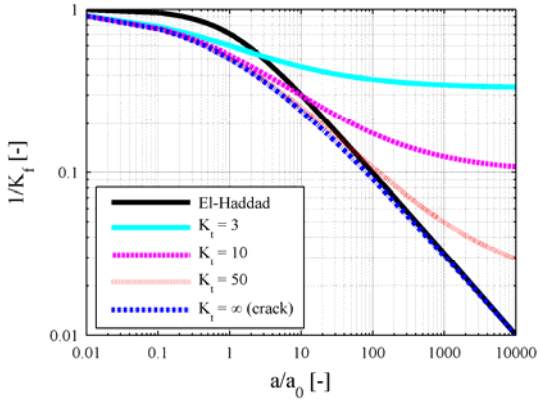

Fig. 3: Prediction of fatigue behavior according to Eq. (3).

Fig. 3 shows that Neuber modified formula is conservative in the short cracks/short notches region in comparison with El-Haddad.

Taylor [33] has proposed a unifying theoretical model and applied Neuber's idea to short cracks. He showed that the average stress range evaluated over the distance from the crack tip to $2a_0$ is equal to the plain fatigue limit when $\Delta K = \Delta K_{th}$ and the expression below for K_f holds true Eq. (4).

$$K_f = \left(1 + \frac{a}{a_0}\right)^{0.5} \qquad \text{Eq. (4)}$$

Neuber [28] proposed an approximation solution for the mode I stress intensity factor K_I of a crack at the root of a semi-elliptical notch Fig. 4, Eq. (5).

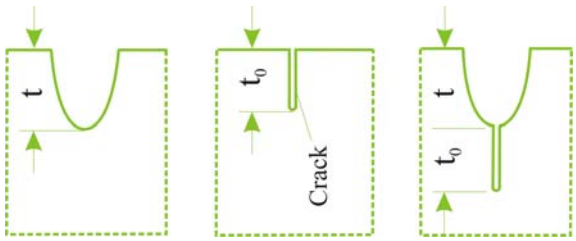

Fig. 4: Semi-elliptical notch with crack, according to Neuber [28].

$$\frac{K_I}{K_{IL}} = s \cdot \left\{1 + \left[\left(K_t - 1\right)^{-2.5} + \left(\frac{1}{s} - 1\right)^{-2.5}\right]^{-0.4}\right\} \qquad \text{Eq. (5)}$$

where K_{IL} and s are the stress intensity factor for a long crack having a length of ($t + t_0$) and geometrical factor of $\sqrt{t_0/(t_0+t)}$, respectively.

Liu [34] has developed the idea of Neuber to indicate the effect of surface profile using the surface fatigue factor F_S Eq. (6).

$$F_{S,Liu} = \frac{\sigma_a}{\sigma_W} = \frac{1}{1+\left[\left(K_{t,Liu}-1\right)^{-2.5} + \left(\sqrt{1+\frac{R_{eff}}{a_0}}-1\right)^{-2.5}\right]^{-0.4}} \qquad \text{Eq. (6)}$$

It should be noted that in Eq. (6) the geometrical value s is replaced by $\sqrt{a_0/(a_0+R_{eff})}$.

This model characterizes the surface topography, besides the surface roughness R_{eff}, with the use of a surface stress concentration factor K_t and a characteristic structural length a_0. Note that the surface fatigue factor F_S exhibits the same expression as $1/K_f$.

The effect of surface finish can conveniently be characterized by the surface fatigue factor. This is the ratio of the fatigue strength σ_a for a particular surface finish to the fatigue strength σ_W (intrinsic fatigue strength) for carefully polished surfaces commonly used for laboratory specimens in which care has been taken to avoid the introduction of residual stresses or hardening or softening the surface layers. σ_W has been measured as 625 MPa for polished specimens employed in this investigation when R = -1 (load case: rotating bending). The surface fatigue factor is normally, as would be expected, less than 1.

2.1. Surface stress concentration factor

The surface stress concentration factor K_t characterizes the stress at the edge of a hole or at a notch root of the surface topography [35]. This factor indicates the surface topography employed by different manufacturing processes as sharp or blunt. The theoretical dependency between the stress concentration factor and the size of surface grooves is defined by the Neuber rule [28]. Neuber recognized that the features of surface topography are more indicative of successive adjacent notches that promote a lower degree of stress concentration than that for a single notch (Fig. 5).

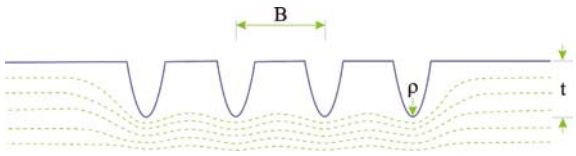

Fig. 5: Near-notch stress trajectories for multiple surface notches.

In application to the surface roughness, the stress concentration factor can be expressed in the empirical form as Eq. (7).

$$K_t = 1 + n\sqrt{\lambda \frac{R_z}{\rho}} \qquad \text{Eq. (7)}$$

where R_z and ρ are the 10-point surface height and the notch root radius, respectively. Coefficient n depends on the kind of stresses: $n = 1$ in shear and $n = 2$ in tension and bending. Coefficient λ depends on the ratio of spacing and height of surface irregularities. With reference to the profile in Fig. 5, $\lambda = B/t$. An alternative expression for the stress concentration factor imposed by surface texture was proposed by Liu [34]. This expression for the stress state in tension and bending is given by Eq. (8)

$$K_{t,Liu} = 1 + \left(2 - \frac{b}{B}\right) \cdot \sqrt{\frac{t}{\rho}} \qquad \text{Eq. (8)}$$

where B and b are the spacing between two successive adjacent notches and the notch pitch, respectively (Fig 6).

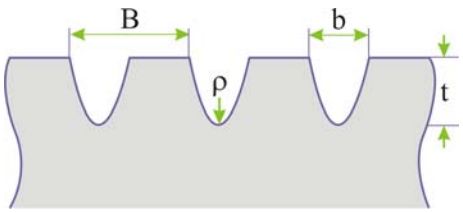

Fig. 6: Multiple surface notches.

Fig. 7 demonstrates the correlation between the stress concentration factor K_t with the features of surface topography in a double logarithmic diagram.

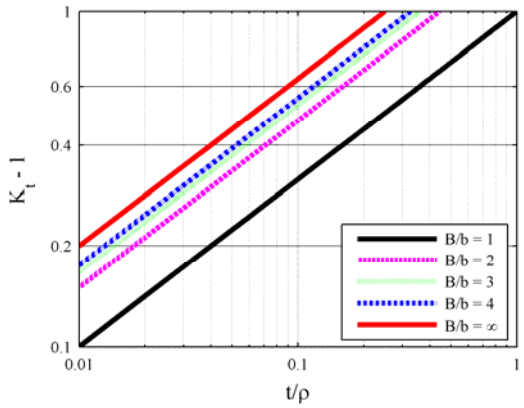

Fig. 7: K_t according to Liu [34], (load case: tension or bending).

2.2. Characteristic structural length

The characteristic structural length represents a material dependent value. This length is defined as the largest non-damaging crack at the fatigue limit which will not grow [36-37]. The characteristic structural length is calculated from the fatigue strength of the material and the threshold value for macroscopic crack propagation. This expression is given by Eq. (9).

$$a_0 = \frac{1}{\pi} \cdot \left(\frac{\Delta K_{th}}{2 \cdot \sigma_W \cdot Y_0} \right)^2 \qquad \text{Eq. (9)}$$

where ΔK_{th} and σ_W are the threshold stress intensity factor range and fatigue limit stress, respectively. For the material employed in this investigation, ΔK_{th} has been assumed as 12 MPa $m^{1/2}$ when R = -1. σ_W is a limiting value where the maximum fatigue limit is achieved and no further reduction in crack depth has any effect. The value of Y_0, which is geometry dependent, is approximately 1.12. The calculated value of a_0 is 22 µm.

2.3. Effective surface roughness

The conventional relationship in turning is for the surface finish to be directly related to the tool feed rate f and the size of the nose radius r_ε. A large feed rate will give shorter cutting times but a poor surface finish. A large nose radius will generate a better surface finish but an excessively large nose radius can lead to vibration tendencies, unsatisfactory chipbreaking and shorter tool-life because of insufficient cutting edge engagement. In practice, therefore, the size of the insert nose radius and the feed rate should be limited in an operation. The

geometric contribution of tool nose radius and tool feed rate, shown in Fig. 8, is also called theoretical surface roughness.

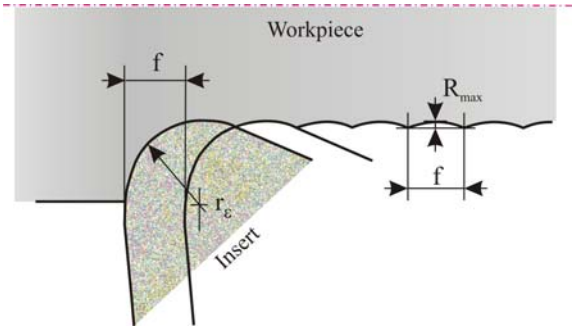

Fig. 8: Illustration of roughness on the finished surface.

A basic theoretical model (Theorem of Pythagoras) for surface roughness is given by the following Eq. (10):

$$R_{\max} = r_\varepsilon - \sqrt{r_\varepsilon^{\,2} - \left(\frac{f}{2}\right)^2} \qquad \text{Eq. (10)}$$

where f is the feed rate (mm/rev.) and r_ε is the tool nose radius (mm).
Note that R_{max} (the maximum height of roughness) describes the sum of the maximum peak height R_p and the maximum valley depth R_v of the contour curve at the reference length. A schematic description of this parameter for an arbitrary machined surface is shown in Fig. 9.

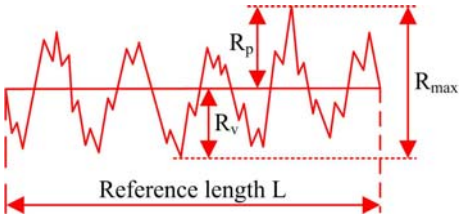

Fig. 9: Schematic illustration of R_{max}.

According to this model, one needs only decrease the feed rate or increase the tool nose radius to improve desired surface roughness. Tool vibration and chip adhesion are such effects that lead to the degradation of surface roughness in this model. Hence the actual surface roughness does not match the theoretical surface roughness.

The effective surface roughness R_{eff} is represented in terms of the peak-to-valley height roughness of the specimen surface topography.

The surface fatigue factor F_S is plotted against the effective surface roughness for various stress concentration factors at the same characteristic structural length (a_0 = 22 µm) in a double logarithmic diagram in Fig. 10.

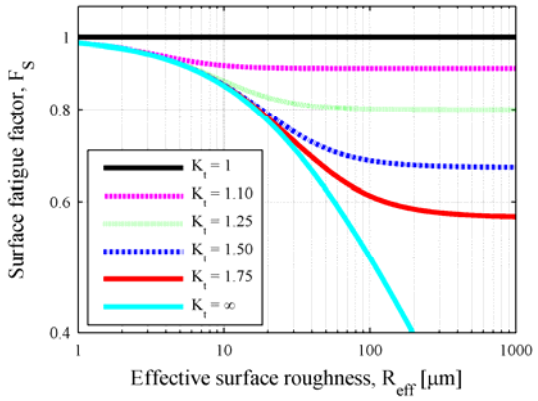

Fig. 10: Surface fatigue factor for different K_t, a_0 = 22 µm.

It can be seen that the influence of surface increases when the stress concentration factor increases. The same effect can be recognized when also the effective surface roughness increases. Fig. 10 also shows that a surface topography with high values of K_t which has small height amplitudes of surface irregularity would be much more detrimental to fatigue life in comparison with a surface topography with small values of K_t which has large height amplitudes.

Fig. 11 presents the correlation between the surface fatigue factor F_S with the effective surface roughness for various characteristic structural lengths at the same stress concentration factor (K_t = 1.5) in a double logarithmic diagram.

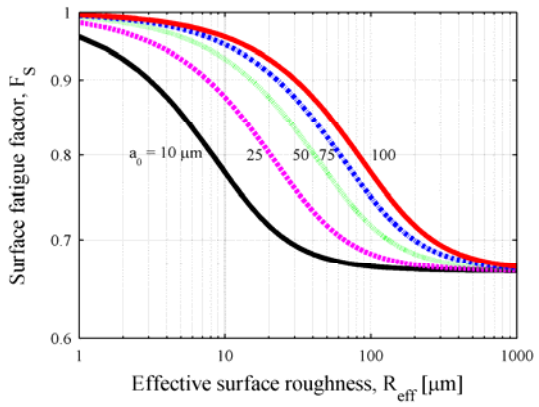

Fig. 11: Surface fatigue factor for different a_0, K_t = 1.5.

Fig. 11 demonstrates that the influence of the surface decreases when the characteristic structural length increases. This means that the high strength materials which are more sensitive to the specific features of the surface are more notch sensitive.

3. Proposing a modified model

Geometrical discontinuities in mechanical components and structures such as notches and cracks cause localized perturbations of the stress distributions in the neighborhood of these stress raisers. Analytical, numerical and experimental methods were used to evaluate these stress fields by several authors. Some reported that the stress distribution in such fields depends on the opening angle of notches [38-41].

Machining parameters such as feed rate f and nose radius r_ε affect the notch opening angle φ, Fig. 12.

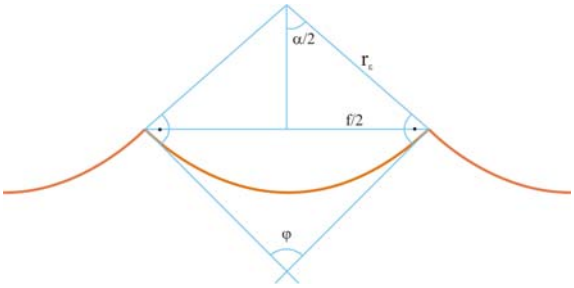

Fig. 12: Illustration of notch opening angle and machining parameters.

Eq. (11) shows the relationship between φ and machining parameters.

$$\varphi = 2 \cdot \arccos\left(\frac{f}{2 \cdot r_\varepsilon}\right) \qquad \text{Eq. (11)}$$

Since these parameters affect the opening angle and influence the stress field, the authors of the present work carried out finite element analyses using ABAQUS® to evaluate the stress distribution caused by a different combination of machining parameters Tab. 3.

Multiple surface notches were simulated based on different feed rates and nose radii and the maximum principle stress was plotted against the distance from the notch tip in a double logarithmic diagram, Fig.13.

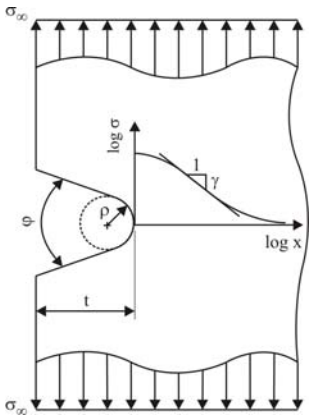

Fig. 13: Singularity degree γ of the stress field at the notch bottom.

Note that the notch root radius ρ is equal to the tool nose radius r_ε.

The results of FE-analyses show that the degree of singularity γ of the asymptotic stress solution is no longer 0.5 according to linear elastic fracture mechanics but changes from case to case depending on the machining parameters, Tab. 5. This is not surprising, as the degree of singularity of the linear elastic stresses is related to the machining parameter which is a function of f and r_ε Eq. (15).

The authors propose a slight modification to Liu's formula [34] which has been applied to Eq. (12).

$$F_S = \frac{1}{1+\left[\left(K_{t,Liu}-1\right)^{-2.5}+\left(\left(1+\frac{\mathrm{R}_{eff}}{a_0}\right)^{\gamma}-1\right)^{-2.5}\right]^{-0.4}} \qquad \text{Eq. (12)}$$

The modification lies in the proposed parameter γ which takes into account the influence of the surface stress singularity.

Further analysis shows that the surface fatigue factor F_S has a range as demonstrated in Eq. (13).

$$F_S = \begin{cases} \dfrac{1}{\left(1+\dfrac{R_{eff}}{a_0}\right)^{\gamma}} & \text{for} \quad R_{eff} < a_0 \\ \dfrac{1}{K_t} & \text{for} \quad R_{eff} > a_0 \end{cases} \qquad \text{Eq. (13)}$$

4. Experimental details

4.1. Material and surface conditions

The material used for machining and fatigue testing was a 0.34% carbon steel in the form of rolled cylindrical bars of 20 mm diameter. Steel was used in this investigation because steel is very commonly used for mechanical parts with balanced strength/weight ratio with respect to cost. Steel bars of the type 34CrNiMo6 (quenched and tempered) with the material number 1.6582 had been heat treated to obtain a tensile strength R_m of 1100 MPa. The micrograph of the bar feedstock is presented in Fig. 14, which shows that the microstructure is composed of bainite.

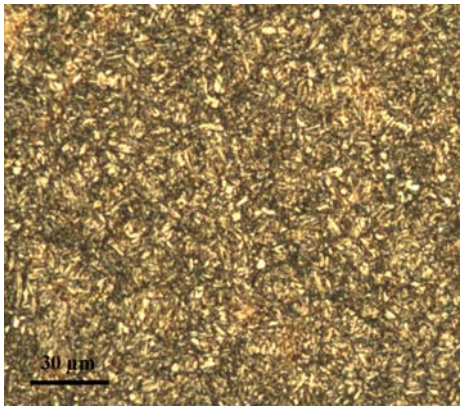

Fig. 14: Confocal scanning laser micrograph of the bar feedstock.

The chemical composition and mechanical properties of this steel are given in Tab. 2, where R_e and A are the yield strength and elongation to failure, respectively.

Steel	Chemical composition					Mechanical properties		
	C	Mn	Cr	Ni	Mo	R_e	R_m	A
34CrNiMo6	(wt%)					MPa	MPa	(%)
	0.36	0.64	1.52	1.44	0.15	1045	1115	15.0

Tab. 2: Chemical composition and mechanical properties of 34CrNiMo6.

In order to produce a range of surface topography, test specimens were given a variety of surface conditions. The following types of surface finish were produced using the methods explained below:

(a) Turning: a series of regular grooves were produced, perpendicular to the long axis of the specimens (longitudinal turning) using an ordinary stable two-axes CNC lathe (Mori Seiki SL 25 2001) at various feed rates f. The test specimens were machined by turning in wet conditions. Turning was performed using inserts DCMT 11 T3 02, 04, 08 4025 from Sandvik. The three inserts differ from each other in nose radius r_ε. The depth of cut and the cutting speed for all specimens was 0.5 mm and 80 m/min, respectively. A new cutting tool was used for each specimen. The cutting conditions employed for these samples are shown in Tab. 3.

Feed rate (mm/rev.)	0.1, 0.2, 0.3
Nose radius (mm)	0.2, 0.4, 0.8
Depth of cut (mm)	0.5
Cutting speed (m/min.)	80

Tab. 3: Cutting condition employed for turned specimens.

Two series of turned specimens produced by cutting condition f = 0.1 mm/rev and r_ε = 0.2 mm were used to produce the other surface finishes using the following methods:

(b) Grinding: using normal workshop practice.

(c) Shot peening: was performed by means of an injector-type system. Steel shot 0.35 mm in diameter (SD-G3) were used. All peening was done at full coverage. The intensity achieved was 0.21mmA.

(d) Grinding after shot peening: One series of shot peened specimens were ground using normal workshop practice.

The specimens produced by the aforementioned methods have the configuration as in Fig.15.

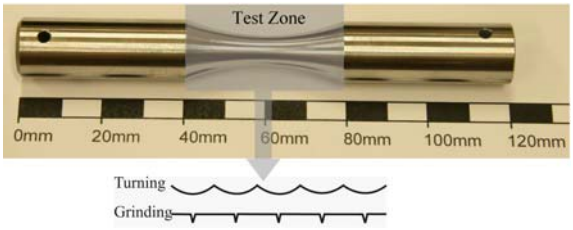

Fig. 15: Configuration of the test specimens.

4.2. Surface roughness measurement

After the machining process, measurement of the surface roughness, using laser scanning microscopy, was carried out in the longitudinal direction in the middle of specimen. Fig. 16 shows the machined surface using the scanning technique for the cutting condition f = 0.2 mm/rev and r_ε = 0.2 mm.

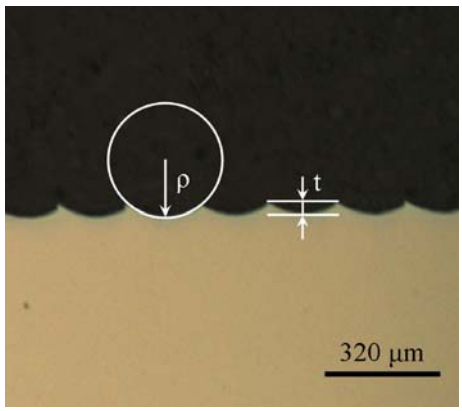

Fig. 16: Longitudinal section at the test zone of a turned specimen.

The parameters t and ρ can be defined approximately as R_{eff} and r_ε, respectively.

4.3. Fatigue testing

A rotating bending fatigue testing machine of the uniform bending moment type with a rotation speed of 3800 rpm was used to carry out the fatigue tests. The fatigue program was conducted on test specimens in this bending mode in air at room temperature under constant amplitude loading conditions. The fatigue limit is defined as the nominal bending stress under

which a specimen endured 10^7 cycles. When the number of rotations exceeded 10^7 the test was stopped, which meant the test specimen would not break under that condition (test-piece run out). At least sixteen specimens were used to verify the fatigue life for every type of surface finish. The design of the fatigue specimens was demonstrated in Fig. 15.

5. Results

Surface profiles of the machined specimens were used to determine the effective surface roughness of each surface finish. The measurement of surface roughness using scanning laser microscopy was repeated at least 5 times for each surface finish. The surface roughness of the turned specimens was also calculated by means of Eq. (10). The measured (real) and calculated (theoretical) surface roughness for each combination of feed rate and nose radius for the turned specimens is listed in Tab. 4.

Surface finish	Cutting condition		Measured	Calculated	Predicted
	f [mm]	r_ε [mm]	R_{max} [µm]	R_{max} [µm]	R_{max} [µm]
Turning	0.1	0.2	7.70	6.35	7.56
	0.1	0.4	4.00	3.14	4.09
	0.2	0.2	29.13	26.79	29.64
	0.2	0.4	13.62	12.70	14.42
	0.2	0.8	4.79	6.27	7.48
	0.3	0.8	16.60	14.19	16.02
	0.4	0.8	28.60	25.40	28.14

Tab. 4: Measured and calculated surface roughness for turned specimens.

Tab. 4 shows that the actual surface roughness does not match the theoretical surface roughness and Eq. (14) describes the relationship between real and theoretical surface roughness using a regression analysis to obtain a least squares fit for the data of the cutting conditions from Tab. 4.

$$R_{\max(\text{measured})} = 1.08 \times R_{\max(\text{calculated})} + 0.7\,[\mu\text{m}] \qquad \text{Eq. (14)}$$

Eqs. (10) and (14) can be used to predict the effective surface roughness. Fig. 17 reports the predicted surface roughness versus that of the measured.

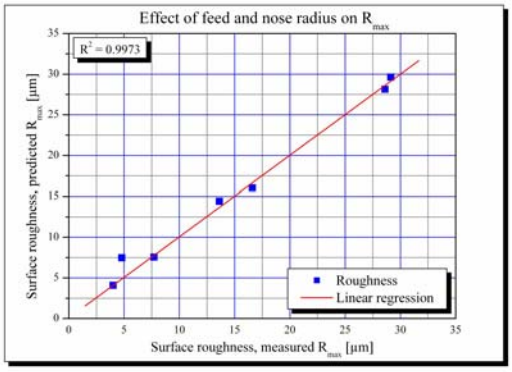

Fig. 17: Predicted vs. measured surface roughness for turned specimens.

There is a fairly good agreement between predicted and measured values as can be derived. Surface profiles of the ground and shot peened specimens were recorded by confocal scanning laser microscope (LEXT) and used to determine the effective surface roughness and profile valley radii at the test zone. The longitudinal sections at the test zone of ground and shot peened specimens are shown in Fig. 18 and Fig. 19, respectively.

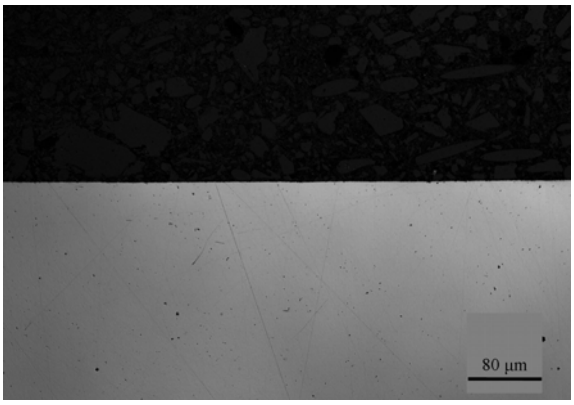

Fig. 18: Longitudinal section at the test zone of a ground specimen.

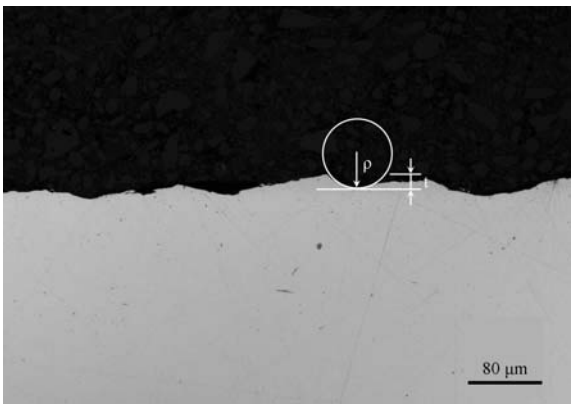

Fig. 19: Longitudinal section at the test zone of a shot peened specimen.

The effective surface roughness, stress concentration factor, degree of singularity and surface fatigue factor for each type of surface finish are listed in Tab. 5.

Surface finish	f [mm]	r_ε [mm]	R_{eff} [µm]	K_t	γ	Fs
Turning	0.1	0.2	7.56	1.194	0.08	0.977
	0.1	0.4	4.09	1.101	0.04	0.993
	0.2	0.2	29.64	1.385	0.13	0.897
	0.2	0.4	14.42	1.190	0.08	0.961
	0.2	0.8	7.48	1.097	0.04	0.988
	0.3	0.8	16.02	1.142	0.06	0.968
Grinding		0.0001	1.50	2.0	0.4	0.974
Peening		0.038	14.00	1.4	0.2	0.907
Peening & Grinding		0.0001	1.50	2.0	0.4	0.974

Tab. 5: Results of surface topography and surface fatigue factor for different surface finishes.

Eq. (15) shows an analytical expression based on the experimental results obtained in turning.

$$\gamma = 0.13 \cdot \left(\frac{f}{r_\varepsilon} \right)^{0.70} \qquad \text{Eq. (15)}$$

Fig. 20 demonstrates the correlation between the surface fatigue factor F_S with the effective surface roughness for various degrees of singularity for the same characteristic structural length and stress concentration factor (a_0 = 22 µm, K_t = 2.5) as given by the double logarithmic diagram.

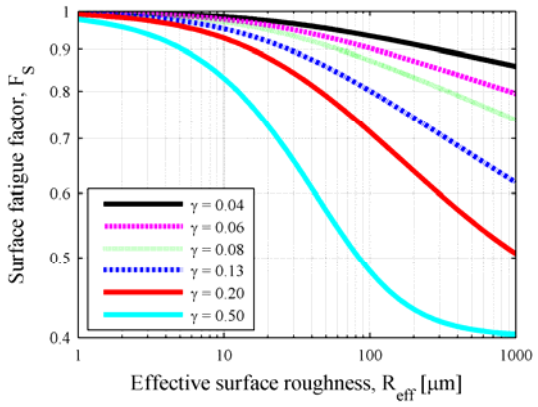

Fig. 20: Surface fatigue factor for different γ at a_0 = 22 µm and K_t = 2.5.

The surface fatigue factor F_S is plotted for the data investigated in this study at the characteristic structural length (a_0 = 22 µm) in Fig. 21.

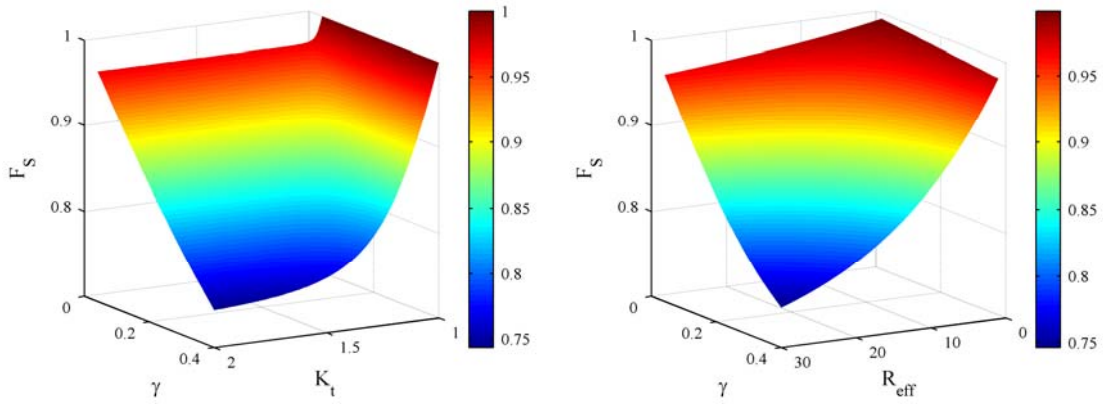

Fig. 21: Surface fatigue factor of different surface finishes at a_0 = 22 µm.

Fig. 21 shows that the variation of K_t and R_{eff} has no large impact on the surface fatigue factor provided γ is small whereas when γ is large, the variation of K_t and R_{eff} influences the surface fatigue factor dramaticaly.

The results indicate that the data investigated in this study can be described in the same terms as short crack data, using a Kitagawa [42] diagram in which the crack length axis is replaced by effective surface roughness and the surface fatigue factor can be estimated according to Eq. (16).

$$F_S = \left(1 + \frac{R_{eff}}{a_0}\right)^{-\gamma} \qquad \text{Eq. (16)}$$

The results of the rotating bending fatigue test conducted with an R value of -1 are plotted in Tab. 6.

Surface finish	f [mm]	Fs	σa ,Measured	σa,Predicted
Turning	0.1	0.977	569	610
	0.1	0.993	574	621
	0.2	0.897	511	561
	0.2	0.961	429	601
	0.2	0.988	462	618
	0.3	0.968	434	605
Grinding		0.974	667	609
Peening		0.907	637	567
Peening & Grinding		0.974	670	609

Tab. 6: Measured and predicted fatigue endurance data.

Fig. 22 reports the predicted fatigue endurance versus the measured for the steel investigated.

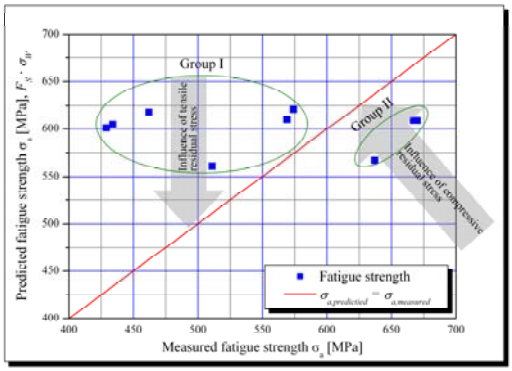

Fig. 22: Predicted vs. measured fatigue strength.

As expected, there is no agreement between predicted and measured values of the fatigue results. This means that surface topography is not the only factor which affects the fatigue strength. Fig. 22 shows that the additional effect of residual stress introduced by the machining process would interfere with the effect of surface topography. Two groups of surface finishes that exhibit two different kind of residual stresses can be recognized in Fig. 22. Group I includes specimens with a high level of tension residual stress produced by turning. The second group demonstrates ground and shot peened specimens with compressive residual stresses. This leads to the fact that tensile residual stress decreases and compressive residual stress increases the fatigue strength. It can also be seen that the tensile residual stress reduces the fatigue limit greatly whilst the compressive residual stress improves the fatigue strength only marginally.

6. Discussion

It can clearly be seen from the results plotted in Fig. 22 that the residual stress produced by surface finish process has a marked effect on the fatigue behavior. To understand the effect of surface topography, residual stresses were eliminated by some research studies [43-44] but it should be noted that a stress relief treatment may alter the metallurgical condition of the material. It has been well known that both of these factors act together and affect fatigue strength in a complex manner [45]. Therefore they must be simultaneously taken into consideration in the evaluation of fatigue strength. Despite the great volume of work done on the influence of surface finish on fatigue strength, no reliable quantitative models have been developed to describe this effect. A model that would be able to predict the fatigue strength must include two factors namely the surface fatigue factor and the residual stress factor respectively. Surface fatigue factor represents the effect of surface topography on the fatigue strength and the model presented in this paper can be used to indicate this effect. In the next part of this paper the influence of residual stress on fatigue strength will be analyzed and discussed. Furthermore a predictive model will be proposed that can be used to estimate the residual stress factor for different surface finishes.

7. Conclusion

From an investigation into the effect of surface finish on the fatigue strength of a quenched and tempered steel the following conclusions have been formed.

1. The standard surface roughness parameters should not be used on an individual basis for evaluating the effect of surface topography on fatigue strength and the model proposed in this paper can be used to estimate the surface fatigue factor for different surface finishes.

2. Due to tool vibration and chip adhesion in surface finishing process, the actual surface roughness does not match the theoretical surface roughness.

3. The surface fatigue factor generally decreases when the stress concentration factor and the effective surface roughness increase.

4. The degree of singularity of the stress distribution at the notch root is a function of machining parameters such as feed rate and tool nose radius.

5. A reasonable agreement between the predicted and experimental fatigue strength can only be obtained, when the effect of residual stress in addition to surface topography is taken into consideration.

Acknowledgements

This work was supported by Austrian Aeronautics Research. The authors would also like to thank Robert Schreiber and his team at Pankl Racing Systems Group for their support in sample machining.

References

[1] S. Suresh, Fatigue of materials, Cambridge University Press, 1998.

[2] S. Petinov, Fatigue analysis of ship structures, Backbone Publishing Company, 2003.

[3] E. Zahavi and V. Torbilo, Fatigue design – Life expectancy of machine parts, CRC Press, 1996.

[4] E. Haibach, Betriebsfestigkeit, Springer, 2002.

[5] D. Radaj, Ermüdungsfestigkeit, Springer, 2003.

[6] G.M. Sinclair, H.T. Corten and T.J. Dolan, Effect of surface finish on the fatigue strength of titanium alloys RC130B and Ti 140A, Trans. ASME, 79(1) (1957) 89-96.

[7] P.G. Forest, Fatigue of metals, Pergamon Press, Oxford, 1962.

[8] R.W. Suhr, The effect of surface finish on high cycle fatigue of a low alloy steel, Edited by K.J. Miller and E.R. de los Rios, The behavior of short fatigue cracks, EGF Publ., Mechanical Engineering Publications, London, (1986) 69-86.

[9] B. Cina, The effect of surface finish on fatigue, Metallurgia, 53 (1957) 11-19.

[10] Y. Murakami, Metal fatigue, Effects of small defects and nonmetallic inclusions, Elsevier Science, 2002.

[11] H.F. Moore and J.B. Kommer, The fatigue of metals, McGraw-Hill, New York, (1927) 201.

[12] M. Kawamoto, K. Nishioka, T. Inui and F. Tsuchiya, The influence of surface roughness of specimens on fatigue strength under rotating-beam test, J. Soc. Mater. Sci. Jpn., 4(19) (1954) 42-48.

[13] D.N. Cledwyn-Davies, Effect of grinding on the fatigue strength of steels, Proc. Instn. Mech. Engrs, 169 (1955) 83-91.

[14] L.P. Tarasov and H.J. Grover, Effects of grinding and other finishing processes on the fatigue strength of hardened steel, Proc. Am. Soc. Test. Mater., 50 (1950) 668-687.

[15] U. Kleemann and H. Zenner, Structural component surface and fatigue strength, Investigations on the effect of the surface layer on the fatigue strength of structural steel components, Mat.-Wiss. u. Werkstofftech., 37(5) (2006) 349-373.

[16] A. Sigwart, Bauteilrandschicht und Schwingfestigkeit, Diss. TU Clausthal, 1994.

[17] L. Pook, Metal fatigue, What it is, Why it matters, Springer, 2007.

[18] F.H. Vitovec and H.F. Binder, Effects of specimen preparation on fatigue, Wright air development department, Tech. Rep., 56 (1956) 289-305.

[19] B.C. Hanley and T.J. Dolan, Surface finish, Metals engineering-design, Soc. Mech. Engrs., (1953) 100.

[20] W.N. Thomas, Effect of scratches and of various workshop finishes upon the fatigue strength of steel, Engineering, 116 (1923) 449-485.

[21] E. Siebel and M. Gaier, Influence of surface roughness on the fatigue strength of steels and non-ferrous alloys, A. Ver. Dtsch. Ing., 98 (1956) 1715.

[22] N.E. Frost, K.J. Marsh and L.P. Pook, Metal fatigue, Carendon Press, Oxford, 1974.

[23] N.E. Dowling, Mechanical behavior of materials, Engineering methods for deformation, Fracture and fatigue, Prentice Hall, Englewood Cliffs, NJ, 1993.

[24] D. Arola and C.L. Williams, Estimating the fatigue stress concentration factor of machined surfaces, Int. J. Fatigue, 24 (2002) 923-930.

[25] B. Syren, Der Einfluss spanender Bearbeitung auf das Biegewechselverformungsverhalten von Ck 45 in verschiedenen Wärmebehandlungszuständen, Dissertation TU Karlsruhe, 1975.

[26] P. Kuhn and H.F. Hardraht, An engineering method for estimating the notch-size effect in fatigue tests on steel, NACA Tech. Note 2805, Langley Aeronautical Laboratory, Washington, 1952.

[27] Y. Weixing, X. Kaiquan and G. Yi, On the fatigue notch factor, K_f, Int. J. Fatigue, 17(4) (1995) 245-251.

[28] H. Neuber, Kerbspannungslehre, Springer-Verlag, Berlin 1937, 1958 u. 1985 (1., 2. u. 3. Aufl.), engl. Ausgabe: Theory of notch stresses, J.S. Edwards, A. Arbor, Mich., 1946.

[29] R.E. Peterson, Notch sensitivity, In: G. Sines and J.L. Waisman, Editors, Metal fatigue, McGraw-Hill, New York, (1959) 293-306.

[30] R.E. Heywood, Designing against fatigue, Chapman and Hall, London, 1962.

[31] M.H. El Haddad, T.H. Topper and K.N. Smith, Prediction of non propagating cracks, Eng. Fract. Mech., 11 (1979) 573-584.

[32] M. Ciavarella and G. Meneghetti, On fatigue limit in the presence of notches: classical vs. recent unified formulations, International Journal of Fatigue, 26 (2004) 289-298.

[33] D. Taylor, Geometrical effects in fatigue: a unifying theoretical model, International Journal of Fatigue, 21 (1999) 413-420.

[34] J. Liu, Dauerfestigkeitsberechnung metallischer Bauteile, Habilitationsschrift TU Clausthal, 2001.

[35] W.D. Pilkey, Peterson's stress concentration factors, John Wiley & Sons, 1997.

[36] D.L. Du Quesnay, M.T. Yu and T.H. Topper, An analysis of notch-size effects at the fatigue limit, Journal of Testing and Evaluation, 16 (1988) 375-386.

[37] P. Lukas, L. Kunz, B. Weiss and R. Stickler, Notch size effect in fatigue, Fatigue Fract. Engng. Mater. Struct., 12 (1989) 175-186.

[38] M.L. Williams, Stress singularities resulting from various boundary conditions in angular corners of plates in extension, J. Appl. Mech., 19 (1952) 526-528.

[39] B. Atzori, P. Lazzarin and G. Meneghetti, A unified treatment of the mode I fatigue limit of components containing notches or defects, International Journal of Fracture, 133 (2005) 61-87.

[40] P. Lazzarin and R. Tovo, A unified approach to the evaluation of linear elastic stress fields in the neighborhood of cracks and notches, International Journal of Fracture, 78 (1996) 3-19.

[41] P. Lazzarin, R. Tovo and S. Filippi, Elastic stress distributions in finite size plates with edge notches, International Journal of Fracture, 91 (1998) 269-282.

[42] H. Kitagawa and S. Takahashi, Applicability of fracture mechanics to very small cracks or the cracks in the early stages, Proc. 2th Int. Conf. Mech. Behav. Mater., Boston, (1976) 627-639.

[43] D. Taylor and O.M. Clancy, The fatigue performance of machined surfaces, Fatigue Fract. Engng. Mater. Struct., 14 (1991) 329-336.

[44] P. Greenfield and D.H. Allen, The effect of surface finish on the high cycle fatigue strength of materials, GEC Journal of Research, 5 (1987) 129-140.

[45] A. Javidi, U. Rieger and W. Eichlseder, The effect of machining on the surface integrity and fatigue life, International Journal of Fatigue, Int. J. of Fatigue, 30 (2008) 2050–2055.

Publication III

FATIGUE STRENGTH PREDICTION OF DIFFERENT SURFACE FINISHES IN THE PRESENCE OF RESIDUAL STRESSES

Ataollah Javidi, Ulfried Rieger, Wilfried Eichlseder

Submitted for Publication

FATIGUE STRENGTH PREDICTION OF DIFFERENT SURFACE FINISHES IN THE PRESENCE OF RESIDUAL STRESSES

Ataollah Javidi, Ulfried Rieger, Wilfried Eichlseder

Department of Mechanical Engineering, University of Leoben, 8700 Leoben, Austria

Abstract

Manufacturing processes induce residual stresses in components. These residual stresses can considerably modify the fatigue performance of mechanical structures. Residual stresses are superimposed on the load applied to the component and influence the mean stress during cyclic loading. The state of stress resulting from applied service loading can be uniaxial, but the nature of residual stresses is always multiaxial. In order to evaluate the fatigue strength in the presence of residual stresses, a multiaxial fatigue criterion is required. In this paper, an empirical multiaxial fatigue model is presented to predict the fatigue strength of different surface finishes in the presence of residual stresses. Furthermore, a comparison is made between the proposed empirical model, shear stress intensity hypothesis and quadratic failure criterion, using results from fatigue tests and measurements of residual stresses on cylindrical specimens from a quenched and tempered steel 34CrNiMo6.

Keywords: Surface residual stress, Multiaxial stress state, Fatigue strength

Nomenclature

A	elongation to failure	p	mean stress sensitivity according to QVH
F_{RS}	residual stress factor	q,s	empirical parameter of EMP
F_S	surface fatigue factor	r_ε	tool nose radius
K	empirical coefficient	γ	degree of singularity
K_t	stress concentration factor	δ	rotating angle
M,M_τ	mean stress sensitivity	σ_{11}	axial residual stress
R	stress ratio	σ_{22}	circumferential residual stress
R^2	regression coefficient	σ_A	stress amplitude in uniaxial fatigue loading according to QVH
R_e	yield strength	σ_a,τ_a	stress amplitude
R_{eff}	effective surface roughness	σ_m,τ_m	mean stress
R_m	tensile strength	σ_{RS}	residual stress
a,b,m,n	coefficients of SIH	σ_{Sch}	fatigue limit for pulsating axial loading
a_0	characteristic structural length	σ_{va},τ_{va}	equivalent stress amplitude
d_0	specimen diameter at test zone	σ_{vm},τ_{vm}	equivalent mean stress
f	feed rate	σ_W	fatigue limit for alternating axial loading (tension-compression)
l_0	integral length	τ_{Sch}	fatigue limit for pulsating torsional loading
n_χ	fatigue ratio factor	τ_W	fatigue limit for alternating torsional loading

1. Introduction

Residual stresses are the dominant factor affecting the fatigue behavior of materials. They are superimposed on the load applied to the component and thus alter the fatigue resistance. Many researchers reported that the residual stresses are equivalent to the mean stresses in their effect [1-6]. Therefore the effect of residual stresses in fatigue behavior is evaluated using Haigh diagram, in which the mean stress in a fatigue cycle is replaced by $\sigma_m + \sigma_{RS}$, as is shown in Fig. 1.

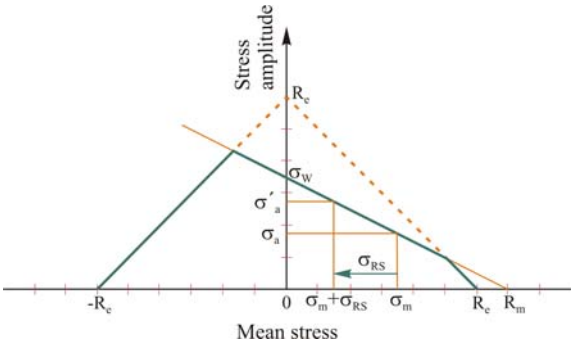

Fig. 1: Haigh diagram to evaluate the fatigue limit in the presence of residual stress [7].

The fatigue limit in the presence of residual stress can be expressed as in Eq. (1).

$$\sigma_a = \sigma_W - M \cdot \left(\sigma_m + \sigma_{RS}\right) \qquad \text{Eq. (1)}$$

where M is a constant, which depends on the mechanical properties of the material, and is called the mean stress sensitivity.

The Haigh diagram provides a very simple means of predicting the effect of residual stress on fatigue strength, but the multiaxial nature of the residual stresses is neglected. This problem raises the question of selecting a multiaxial fatigue criterion to evaluate the effect of residual stresses [7]. Due to the prediction of the endurance limit under multiaxial loading, many multiaxial criteria have been developed in recent years [8-12]. Multiaxial fatigue assessments are carried out using an appropriate rule or criterion to reduce the complex multiaxial loadings to an equivalent uniaxial loading. The multiaxial fatigue criteria are divided into three groups, i.e. stress criteria, strain criteria and energy criteria. The stress criteria can be categorized into three viewpoints, i.e. integral approaches, critical plane approaches, and empirical formulae. In the integral approach the calculation of the equivalent stress is carried out as an integral of the stresses over all cutting planes of a volume element. The critical plane approach assumes that the failure occurs in the critical plane with the maximal value of equivalent stress. The shear stress intensity hypothesis SIH and the quadratic failure criterion QVH typically represent the integral method and critical plane approach, respectively.

In this paper, a simple plane stress state with an alternating normal stress and two static biaxial normal stresses was studied, Fig. 2.

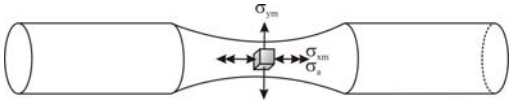

Fig. 2: Investigated stress state.

This state of stress is of special practical importance when the effect of biaxial residual stresses is evaluated. Many mechanical components such as shafts, axles, con-rods, etc. experience this kind of stress state where biaxial residual stresses at their surface superimpose on the alternating normal stress resulting from the applied loading. These residual stresses are introduced by manufacturing operations and their nature is multiaxial.

In this study the shear stress intensity hypothesis and quadratic failure criterion are first discussed briefly and then an empirical formula is proposed. Furthermore, a comparison is made between these criteria using results from fatigue tests and measurements of residual

stresses on cylindrical specimens from a quenched and tempered steel 34CrNiMo6. In addition, the validation of the proposed empirical model is verified by means of experimental data reported in the literature.

1.1. Shear Stress Intensity Hypothesis (SIH)

This approach is based on an expression derived by Novozhilov [13] under the name of mean tangential stress. Novozhilov showed that the root mean square value of the shear stresses over all cutting planes is identical to the von Mises stress, as given in Eq. (2).

$$\tau_{\text{int}} = \left(\frac{1}{4\pi} \int_{\gamma=0}^{\pi} \int_{\varphi=0}^{2\pi} \tau_{\gamma\varphi}^{2} \cdot \sin\gamma \cdot d\varphi \cdot d\gamma \right)^{\frac{1}{2}} \cong \left(3I_2'\right)^{\frac{1}{2}} \qquad \text{Eq. (2)}$$

Simbürger [14] modified the idea of Novozhilov for application to fatigue problems under the name of effective shear stress hypothesis which was later been described by Zenner and Richter in a slightly modified form as the shear stress intensity hypothesis [15-16]. A further development of the shear stress intensity hypothesis was proposed by Liu [17-18]. In this modification, the equivalent shear and normal stress amplitudes are evaluated as the integral of the stresses over all cutting planes. In order to obtain the mean stresses, the mean shear and normal stresses are weighted over the shear and normal stress amplitudes, respectively. Eqs. (3)-(6) show the simplified form of the equivalent stress for each of the four stress components in the cutting plane.

$$\tau_{\text{va}} = \left\{ \frac{15}{8\pi} \int_{\gamma=0}^{\pi} \int_{\varphi=0}^{2\pi} \tau_{\gamma\varphi a}^{2} \cdot \sin\gamma \cdot d\varphi \cdot d\gamma \right\}^{\frac{1}{2}} \qquad \text{Eq. (3)}$$

$$\sigma_{\text{va}} = \left\{ \frac{15}{8\pi} \int_{\gamma=0}^{\pi} \int_{\varphi=0}^{2\pi} \sigma_{\gamma\varphi a}^{2} \cdot \sin\gamma \cdot d\varphi \cdot d\gamma \right\}^{\frac{1}{2}} \qquad \text{Eq. (4)}$$

$$\tau_{\mathrm{vm}} = \left\{ \frac{\int_{\gamma=0}^{\pi} \int_{\varphi=0}^{2\pi} \tau_{\gamma\varphi a}^{2} \cdot \tau_{\gamma\varphi m}^{2} \cdot \sin\gamma \cdot d\varphi \cdot d\gamma}{\int_{\gamma=0}^{\pi} \int_{\varphi=0}^{2\pi} \tau_{\gamma\varphi a}^{2} \cdot \sin\gamma \cdot d\varphi \cdot d\gamma} \right\}^{\frac{1}{2}} \quad \text{Eq. (5)}$$

$$\sigma_{\mathrm{vm}} = \left\{ \frac{\int_{\gamma=0}^{\pi} \int_{\varphi=0}^{2\pi} \sigma_{\gamma\varphi a}^{2} \cdot \sigma_{\gamma\varphi m} \cdot \sin\gamma \cdot d\varphi \cdot d\gamma}{\int_{\gamma=0}^{\pi} \int_{\varphi=0}^{2\pi} \sigma_{\gamma\varphi a}^{2} \cdot \sin\gamma \cdot d\varphi \cdot d\gamma} \right\} \quad \text{Eq. (6)}$$

Eq. (7) shows the failure condition using the combination of equivalent stresses.

$$a \cdot \tau_{\mathrm{va}}^{2} + b \cdot \sigma_{\mathrm{va}}^{2} + m \cdot \tau_{\mathrm{vm}}^{2} + n \cdot \sigma_{\mathrm{vm}} = \sigma_{W}^{2} \quad \text{Eq. (7)}$$

The coefficients *a*, *b*, *m* and *n* can thus be obtained from Eqs. (8)-(11).

$$a = \frac{1}{5} \cdot \left[3 \cdot \left(\frac{\sigma_{W}}{\tau_{W}} \right)^{2} - 4 \right] \quad \text{Eq. (8)}$$

$$b = \frac{1}{5} \cdot \left[6 - 2 \cdot \left(\frac{\sigma_{W}}{\tau_{W}} \right)^{2} \right] \quad \text{Eq. (9)}$$

$$m = \frac{\sigma_{W}^{2} - \left(\frac{\sigma_{W}}{\tau_{W}} \right)^{2} \cdot \left(\frac{\tau_{Sch}}{2} \right)^{2}}{\frac{4}{7} \cdot \left(\frac{\tau_{Sch}}{2} \right)^{2}} \quad \text{Eq. (10)}$$

$$n = \frac{\sigma_W^2 - \left(\frac{\sigma_{Sch}}{2}\right)^2 - \frac{4m}{21}\cdot\left(\frac{\sigma_{Sch}}{2}\right)^2}{\frac{5}{7}\cdot\left(\frac{\sigma_{Sch}}{2}\right)} \qquad \text{Eq. (11)}$$

Liu [19] proposed an explicit solution for the endurance limit under the load case studied in this paper based on the shear stress intensity hypothesis, Eq. (12).

$$\sigma_a = \sigma_W \cdot \sqrt{1 - \frac{5n}{7}\cdot\frac{\sigma_{xm}}{\sigma_W^2} - \frac{4m}{21}\cdot\frac{\sigma_{xm}^2}{\sigma_W^2} - \frac{n}{7}\cdot\frac{\sigma_{ym}}{\sigma_W^2} - \frac{m}{7}\cdot\frac{\sigma_{ym}^2}{\sigma_W^2}} \qquad \text{Eq. (12)}$$

where σ_a refers to the fatigue endurance limit in the presence of two static normal mean stresses, σ_{xm} and σ_{ym}.

The shear stress intensity hypothesis like several other prediction criteria for fatigue evaluation requires the fatigue strength measured either in pure tension σ_W or in pure torsion τ_W as an input parameter. From the application of the von Mises criterion for static multiaxial stress evaluation, a value of $\sqrt{3}$ is predicted for the σ_W/τ_W–ratio. For SIH this ratio is measured in the range $2/\sqrt{3} \le \sigma_W/\tau_W \le \sqrt{3}$.

The material's mean stress sensitivity factor M is the next input parameter which is required to evaluate the fatigue behavior in multiaxial loading. Schütz [20] analyzed the sensitivity of a variety of materials for which the fatigue strength was available at $\sigma_m = 0$ *(R = -1)* and at $\sigma_m = \sigma_a$ *(R=0)*. Using these two values for fatigue strength, the mean stress sensitivity factor can be defined by Eq. (13).

$$M = \frac{\sigma_a\left(R=-1\right)}{\sigma_a\left(R=0\right)} - 1 \qquad \text{Eq. (13)}$$

The relationship between the alternating axial loading $\sigma_W = \sigma_a$ *(R=-1)* and the pulsating axial loading $\sigma_{Sch} = 2\sigma_a$ *(R=0)* is given in Eq. (14).

$$\sigma_{Sch} = \frac{2}{1+M}\cdot\sigma_W \qquad \text{Eq. (14)}$$

For the pulsating torsional strength, the value of mean stress sensitivity factor M_τ is approximately estimated by $M_\tau = M/2$ [21], Eq. (15).

$$\tau_{Sch} = \frac{2}{1+\frac{1}{2}\cdot M}\cdot \tau_W \qquad \text{Eq. (15)}$$

Since the effect of the residual stresses are equivalent to the mean stresses, Eq. (12) can be applied to evaluate the effect of residual stress based on SIH, Eq. (16).

$$F_{RS} = \sqrt{1-\frac{5n}{7}\cdot\frac{\sigma_{xm}}{\sigma_W^2}-\frac{4m}{21}\cdot\frac{\sigma_{xm}^2}{\sigma_W^2}-\frac{n}{7}\cdot\frac{\sigma_{ym}}{\sigma_W^2}-\frac{m}{7}\cdot\frac{\sigma_{ym}^2}{\sigma_W^2}} \qquad \text{Eq. (16)}$$

Residual stress factor F_{RS} is the ratio of the fatigue endurance limit σ_a for a particular surface finish with respect to the fatigue strength σ_W (intrinsic fatigue strength) for carefully polished surfaces commonly used for laboratory specimens in which care has been taken to avoid the introduction of residual stresses or the hardening or softening the surface layers Eq. (17).

$$F_{RS} = \frac{\sigma_a}{\sigma_W} \qquad \text{Eq. (17)}$$

This factor can be used as an appropriate factor to predict the endurance limit of different surface finishes produced by the various manufacturing processes.

1.2. Quadratic Failure Hypothesis (QVH)

The critical plane approaches to multiaxial fatigue have evolved from experimental observations of the initiation and growth of cracks during cyclic loading. These types of models attempt to compute fatigue damage on specific planes within a test specimen or component. Troost and El-Magd [22] developed a general form of failure criterion based on the critical plane approach to predict the fatigue endurance limit under multiaxial stresses.

This criterion takes account of anisotropic fatigue behavior which also occurs in the case of isotropic materials.

The QVH includes the relationship between the stress amplitude σ_A and mean stress σ_m in terms of uniaxial fatigue loading. Troost and El-Magd [23] proposed a general quadratic parabola to describe the function $\sigma_A(\sigma_m)$, Eq. (18).

$$\frac{\sigma_A}{\sigma_W} = 1 - p \cdot \left(\frac{\sigma_m}{R_m}\right) - (1 - p) \cdot \left(\frac{\sigma_m}{R_m}\right)^2 \qquad \text{Eq. (18)}$$

where p is a measure to evaluate the mean stress sensitivity, Eq. (19).

$$p = \frac{1 - \left[\frac{\sigma_{Sch}}{2 \cdot \sigma_W} + \left(\frac{\sigma_{Sch}}{2 \cdot R_m}\right)^2\right]}{\frac{\sigma_{Sch}}{2 \cdot R_m} \cdot \left(1 - \frac{\sigma_{Sch}}{2 \cdot R_m}\right)} \qquad \text{Eq. (19)}$$

Fig. 3 demonstrates the correlation between the stress amplitude σ_A with the mean stress σ_m for different values of p with reference to the Haigh diagram.

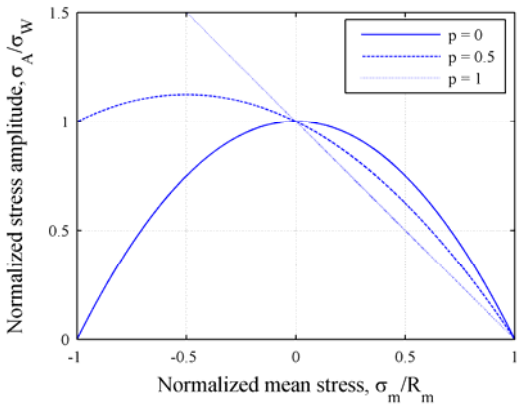

Fig. 3: Stress amplitude vs. mean stress under uniaxial fatigue loading.

The straight line (p = 1) on the normalized plot was proposed by Goodman [24] and is called the Goodman line. The solid curve (p = 0) as illustrated in Fig. 3 represents the Gerber parabola and the dashed curve (p = 0.5) refers to Dietmann parabola [25-26].

The stress components σ_x* and σ_y* for the stress state investigated in this paper (Fig. 4) are given by equation, Eq. (20).

$$\begin{aligned} \sigma_x^* &= \sigma_{xm}^* + \sigma_{xa}^* \cdot \sin \omega t \\ \sigma_y^* &= \sigma_{ym}^* \\ \tau_{xy}^* &= 0 \end{aligned} \qquad \text{Eq. (20)}$$

The same state of plane stress can be described on any other coordinate system, such as x-y (Fig. 4). This system is related to the original one by an angle of rotation δ, and the values of the stress components change to σ_x and σ_y in the new coordinate system.

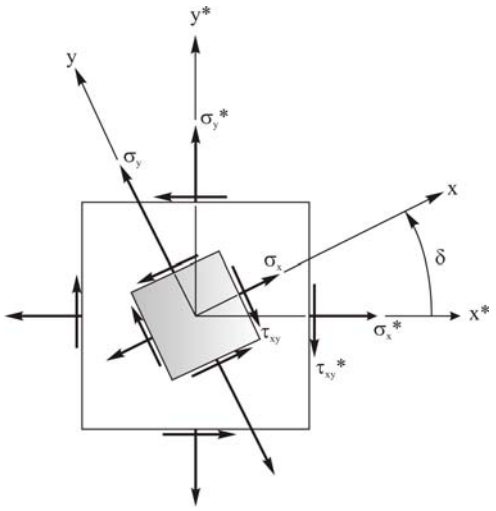

Fig. 4: State of plane stress dependent on the rotation angle δ [22].

The stress components dependent on the angle δ are as described in Eqs. (21)-(22):

$$\begin{aligned} \sigma_{xm} &= \sigma_{xm}^* \cdot \cos^2 \delta + \sigma_{ym}^* \cdot \sin^2 \delta \\ \sigma_{ym} &= \sigma_{xm}^* \cdot \sin^2 \delta + \sigma_{ym}^* \cdot \cos^2 \delta \\ \tau_{xym} &= \left(\sigma_{xm}^* - \sigma_{ym}^*\right) \cdot \sin \delta \cdot \cos \delta \end{aligned} \qquad \text{Eq. (21)}$$

$$\begin{aligned} \sigma_{xa} &= \sigma_{xa}^* \cdot \cos^2 \delta \\ \sigma_{ya} &= \sigma_{xa}^* \cdot \sin^2 \delta \\ \tau_{xya} &= \sigma_{xa}^* \cdot \sin \delta \cdot \cos \delta \end{aligned} \qquad \text{Eq. (22)}$$

Eq. (23) shows the failure criterion proposed by Troost and El-Magd [27] based on the stress state investigated in this study.

$$\left(\frac{\sigma_{xa}}{\sigma_{Ax}}\right)^2 + \left(\frac{\sigma_{ya}}{\sigma_{Ay}}\right)^2 - \frac{\sigma_{xa} \cdot \sigma_{ya}}{\sigma_{Ax} \cdot \sigma_{Ay}} + \left(\frac{\tau_{xya}}{\sigma_{Axy}}\right)^2 = 1 \qquad \text{Eq. (23)}$$

σ_{Ax}, σ_{Ay} and σ_{Axy} are the stress amplitudes as a function of mean stress in terms of uniaxial fatigue loading according to [27] and are given by Eqs. (24)-(26).

$$\sigma_{Ax} = \sigma_W \cdot \left[1 - p \cdot \left(\frac{\sigma_{xm}}{R_m}\right) - (1 - p) \cdot \left(\frac{\sigma_{xm}}{R_m}\right)^2\right] \qquad \text{Eq. (24)}$$

$$\sigma_{Ay} = \sigma_W \cdot \left[1 - p \cdot \left(\frac{\sigma_{ym}}{R_m}\right) - (1 - p) \cdot \left(\frac{\sigma_{ym}}{R_m}\right)^2\right] \qquad \text{Eq. (25)}$$

$$\sigma_{Axy} = \frac{\sigma_W}{\sqrt{3}} \cdot \frac{\left[1 - (1-p) \cdot \left(\frac{\tau_{xym}}{R_m}\right)^2\right]^2 - p^2 \cdot \left(\frac{\tau_{xym}}{R_m}\right)^2}{\sqrt{\left[1 - (1 - p) \cdot \left(\frac{\tau_{xym}}{R_m}\right)^2\right]^2 + \left(\frac{p^2}{3}\right) \cdot \left(\frac{\tau_{xym}}{R_m}\right)^2}} \qquad \text{Eq. (26)}$$

Troost and El-Magd [22, 27] justified that the failure condition is fulfilled by the orientation angles at either $\delta = 0°$ or $\delta = 45°$ with respect to the considered stress state. These angles are called critical orientations.

Fig. 5 shows the correlation between the stress amplitude σ_a with the orientation angle δ in the simplified form of a demonstrated stress state. The minimum values of σ_a refer to the maximum stress amplitude which can be endured by the material. In other words, the minimum values represent the fatigue endurance limit under the considered stress state and

orientation angle. The critical orientation where the failure occurs for the stress state mentioned in Fig.5 (left) is at $\delta = 0°$ and right at $\delta = 45°$ where failure occurs.

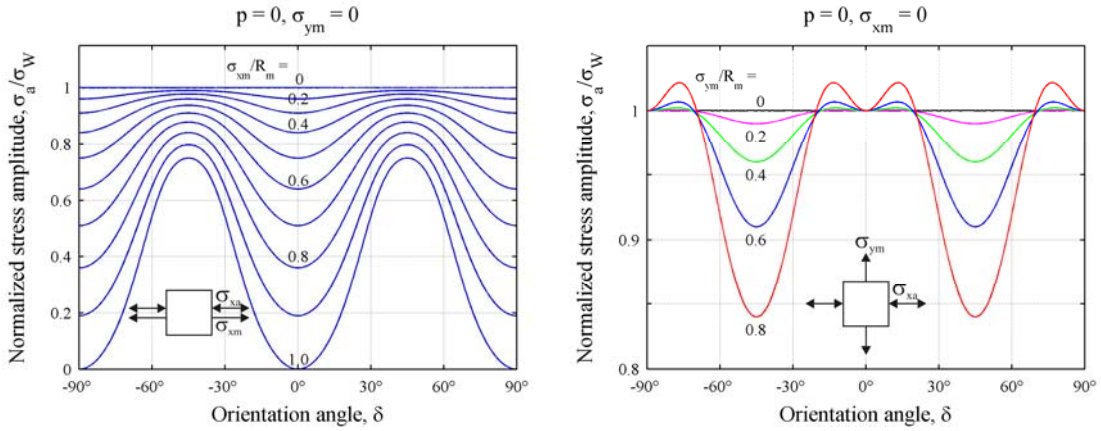

Fig. 5: Stress amplitude dependency on orientation angle and mean stress according to QVH [22, 23].

Fig. 5 also demonstrates that the maximum fatigue endurance limit is calculated by the minimum value of the residual stress factor. The residual stress factor F_{RS} is defined as in Eq. (17).

2. Experimental details

2.1. Material and surface conditions

The material used for machining and fatigue testing was a 0.34% carbon steel in the form of rolled cylindrical bars of 20 mm diameter [28]. Steel bars of the type 34CrNiMo6 (quenched and tempered) with the material number 1.6582 had been heat treated to obtain a tensile strength R_m of 1115 MPa. The chemical composition and mechanical properties of this steel are given in Table 1, where R_e and A are the yield strength and elongation to failure, respectively.

Steel	Chemical composition (wt%)					Mechanical properties		
	C	Mn	Cr	Ni	Mo	Re (MPa)	Rm (MPa)	A (%)
34CrNiMo6	0.36	0.64	1.52	1.44	0.15	1045	1115	15.0

Table 1: Chemical composition and mechanical properties of 34CrNiMo6.

Table 2 shows the material properties investigated for the test specimens.

Material	σ_W (MPa)	σ_{Sch} (MPa)	τ_W (MPa)	τ_{Sch} (MPa)
34CrNiMo6	625	932	415	728

Table 2: Material properties of test specimens.

In order to produce differentiating effects of surface topography and residual stresses, test specimens were given a variety of surface conditions. The following types of surface finish were produced using the methods explained below:

(a) Turning: a series of regular grooves were produced, perpendicular to the long axis of the specimens (longitudinal turning) using an ordinary stable two-axes CNC lathe (Mori Seiki SL 25 2001) at various feed rates *f*. The test specimens were machined by turning in a wet condition. Turning was performed using inserts DCMT 11 T3 02, 04, 08 4025 from Sandvik. The three inserts differ from each other in nose radius r_ε. The depth of cut and the cutting speed was 0.5 mm and 80 m/min. for all specimens, respectively. A new cutting tool was used for each specimen. The cutting conditions employed for these samples are shown in Table 3.

Feed rate (mm/rev.)	0.1, 0.2, 0.3
Nose radius (mm)	0.2, 0.4, 0.8
Depth of cut (mm)	0.5
Cutting speed (m/min.)	80

Table 3: Cutting condition employed for turned specimens.

Two series of turned specimens, produced by cutting condition f = 0.1 mm/rev. and r_ε = 0.2 mm, were used to produce other surface finishes using the following methods:

(b) Grinding: was applied parallel to the longitudinal axis of the test specimens using normal workshop practice. The traces were parallel with the direction of the alternating normal stress.

(c) Shot peening: was performed by means of an injector-type system. Steel shot with a shot size of 0.35 mm in diameter (SD-G3) was used. All peening was done at full coverage. The intensity achieved was 0.21mmA.

(d) Grinding after shot peening: One series of shot peened specimens were ground using normal workshop practice.

The cylindrical test specimens produced by the aforementioned methods have the configuration as shown in Fig.6.

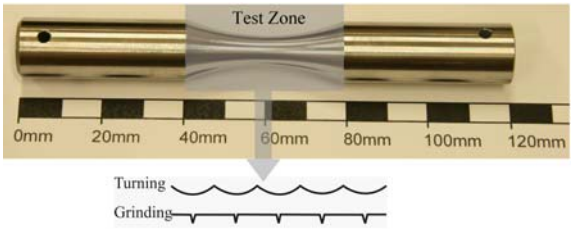

Fig. 6: Configuration of the test specimens.

The specimens were 7.5 mm in diameter at the center.

2.2. Residual stress measurement

X-ray diffraction was used to measure the residual stresses in the specimens following machining. An XSTRESS 3000 analyzer emitting CrKα at 200 W was used to locate the relaxed Fe (211) peak for residual stress measurements. In order to obtain the stress distribution by depth, the layers of specimens were removed by electrolytic polishing. The machined surface was exposed for 20 seconds. Measurements were taken at two angles of 0 deg (axial, σ_{11}) and 90 deg (circumferential, σ_{22}) for each test specimen. Standard $\sin^2\psi$ techniques were employed to determine the normal stress (strain) for each angle. Measurements of residual stresses were carried out for test specimens subjected to 10^7 fatigue cycles at a load level corresponding to the fatigue limit. These residual stresses are characterized as stabilized stresses. In other words, there is no residual stress relief at the fatigue limit level during the cyclic loading. The stabilized residual stresses are used to estimate the residual stress factor.

2.3. Surface topography measurement

The surface topography resulting from the manufacturing process was characterized using a confocal scanning laser microscope and the surface fatigue factor F_S was used as a quantitative description of the surface topography produced by different surface finishes Eq. (27).

$$F_S = \frac{1}{1+\left[\left(K_t-1\right)^{-2.5}+\left(\left(1+\frac{\mathrm{R}_{eff}}{a_0}\right)^{\gamma}-1\right)^{-2.5}\right]^{-0.4}} \qquad \text{Eq. (27)}$$

where K_t and R_{eff} are the surface concentration factor and effective surface roughness, respectively. The parameters γ and a_0 refer to the surface stress singularity and characteristic structural length.

A detailed description of this factor and how it is estimated was given by the authors in [29].

2.4. Fatigue testing

A rotating bending fatigue testing machine of the uniform bending moment type with a rotation speed of 3800 rpm was used to carry out the fatigue tests. The fatigue program was conducted on cylindrical test specimens (7.5 mm in diameter) in the bending mode in air at room temperature under constant amplitude loading conditions (R = -1). The fatigue limit is defined as the nominal bending stress under which a specimen endured 10^7 cycles. When the number of cycles exceeded 10^7 the test was stopped, which meant the test specimen would not break under that condition (test-piece run out). At least sixteen specimens were used to verify the fatigue life for every type of surface finish. The design of the fatigue specimens was demonstrated in Fig. 6.

3. Results and analysis

Machined specimens were measured for the axial σ_{11} and circumferential σ_{22} residual stresses using an X-ray diffraction technique. The measured residual stresses at the machined surface were tensile in all the turning conditions while grinding and peening processes presented compressive residual stresses. The analysis of experimental data for turned specimens investigated in this study shows that the residual stresses are dominated by the two process parameters such as feed rate f and tool nose radius r_ε. Fig. 7 shows the residual stress distribution after turning, produced by different nose radii at the same feed rate f = 0.2 mm/rev.

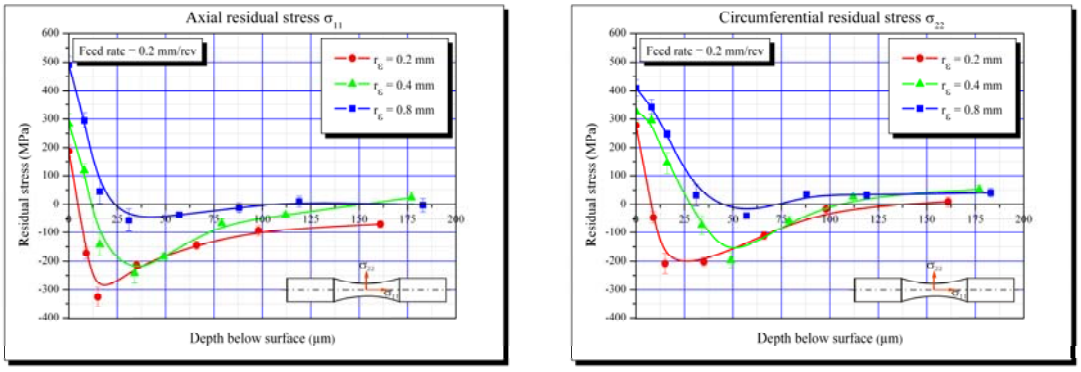

Fig. 7: Residual stress distribution at the turned surface using the same feed rate.

Results indicate that the machine tool with the nose radius r_ε = 0.8 mm causes the maximum value of the tensile residual stress at the surface while the nose radius r_ε = 0.2 mm yields the maximum compressive residual stress below the machined surface. This is not surprising, in so far as the residual compressive stresses are related to the plastic deformation. In other words, the cutting force applied on the machined surface by the cutting tool r_ε = 0.2 mm causes higher plastic compressive shear deformation than r_ε = 0.8 mm. This effect contributes to induce higher compressive residual stresses in the layers beneath the surface. Fig. 8 demonstrates the comparison between different feed rates at the same value of the tool nose radius.

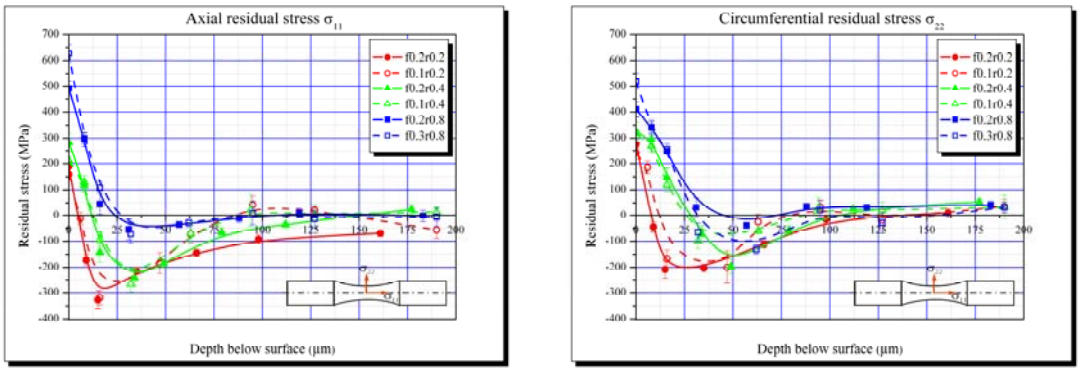

Fig. 8: Residual stress distributions obtained by different feed rates.

Results show that the higher the feed rate, the higher the induced tensile residual stress at the surface. The feed rate f = 0.3 mm/rev. demonstrates this effect well. The high value of tensile residual stress indicates a high level of heat flow into the machined surface due to the friction between the work piece and cutting tool. The maximum values of compressive residual stresses below the surface at different feed rates are of the same order as those where

an equal tool nose radius was used. The maximum compressive residual stresses in a circumferential direction in two cases r_ε = 0.8 mm and r_ε = 0.4 mm show an anomaly which can, up to now not be explained.

The measured surface residual stresses for each surface finish condition are listed in Table 4. It should be noted that the presented results in Table 4 are related to the measured residual stresses at the surface of the specimens and not the layer below the surface.

Surface finish	f [mm]	r_ε [mm]	σ_{11} [MPa]	σ_{22} [MPa]
Turning	0.1	0.2	159	241
	0.1	0.4	211	318
	0.2	0.2	188	277
	0.2	0.4	283	325
	0.2	0.8	491	410
	0.3	0.8	628	518
Grinding			-195	-372
Peening			-478	-488
Peening & Grinding			-425	-498

Table 4: Measured surface residual stresses for different surface conditions.

It is generally accepted that turning generates residual tensile stresses at the surface layers of the metal depending on the machining parameters such as feed rate and tool nose radius. Eq. (28) shows an analytical expression that fits the experimental data obtained from turning.

$$\sigma_{RS} = K_1 + K_2 \cdot f + K_3 \cdot r_\varepsilon \qquad \text{Eq. (28)}$$

where σ_{RS} is the surface residual stress in the axial or in the circumferential direction and K_1, K_2 and K_3 are empirical parameters estimated from experimental data. Table 5 shows the estimated coefficients for the residual stresses in both directions.

State	K_1	K_2	K_3
	[MPa]	[(MPa)(rev/mm)]	[MPa/mm]
σ_{11}	-70	868	508
σ_{22}	140	475	259

Table 5: Estimated empirical coefficients depending on measuring direction.

The regression coefficients of the proposed model are about R^2 = 0.98 for the axial residual stresses σ_{11} and R^2 = 0.94 for the circumferential residual stresses σ_{22}, which

demonstrate an extremely good fit. Table 6 reports the predicted versus the measured values of residual stresses for the turned specimens.

Surface finish	f [mm]	r_ε [mm]	σ_{11} [MPa]	σ_{11} [MPa]	σ_{22} [MPa]	σ_{22} [MPa]
			Measured	Predicted	Measured	Predicted
Turning	0.1	0.2	159	118	241	239
	0.1	0.4	211	220	318	291
	0.2	0.2	188	205	277	287
	0.2	0.4	283	307	325	339
	0.2	0.8	491	510	410	442
	0.3	0.8	628	597	518	490

Table 6: Measured and predicted surface residual stresses for turned specimens.

The measured values of the stabilized surface residual stresses for the peened and ground specimen (Table 4) and the predicted values of the residual stresses for the turned specimen (Table 6) are used for the calculation of the residual stress factor F_{RS}. To compare and to validate the methods of calculation, values for the stabilized residual stresses are introduced into the multiaxial fatigue criteria, discussed in this study as mean stresses.

Fig. 9 demonstrates the correlation between the residual stress factor in the z direction with residual stresses in the axial and the circumferential direction as mean stresses.

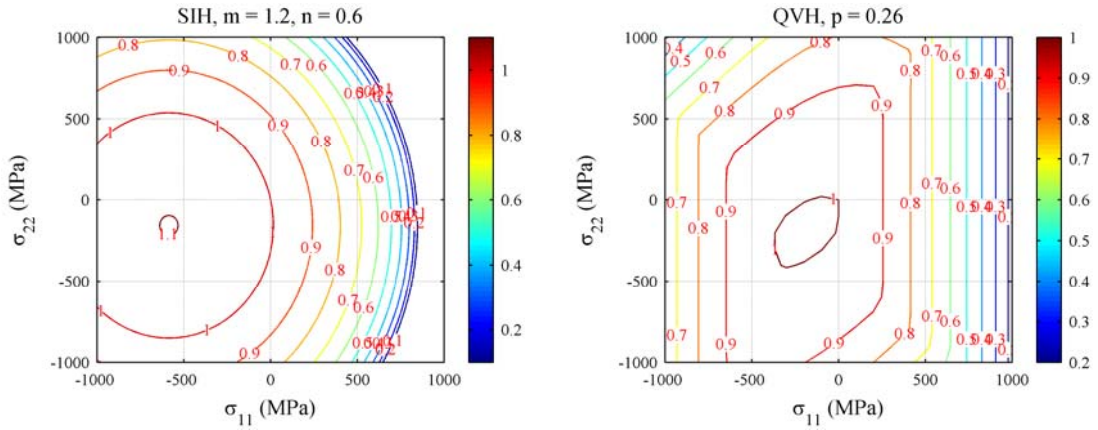

Fig. 9: Variation of residual stress factor as a function of residual stresses according to SIH and QVH.

The authors of this present work propose an empirical model (EMP) which is a stress based critical plane criterion of multiaxial fatigue to evaluate the residual stress factor Eq. (29).

$$F_{RS,EMP} = 1 - p \cdot \left(\frac{\sigma_{xm}}{R_m}\right) - (1-p) \cdot \left(\frac{\sigma_{xm}}{R_m}\right)^2 - \frac{p}{q} \cdot \left(\frac{\sigma_{ym}}{R_m}\right) - \left(\frac{1-p}{q}\right) \cdot \left(\frac{\sigma_{ym}}{R_m}\right)^2 + \left(\frac{\sigma_{xm} \cdot \sigma_{ym}}{R_m{}^2}\right) \cdot s$$

Eq. (29)

where q and s are empirical parameters estimated from experimental data. The calculated value of the parameter p is 0.26 for the material investigated in this study.

Fig. 10 displays the evaluation of fatigue limit (left) and residual stress factor (right) using the proposed empirical model.

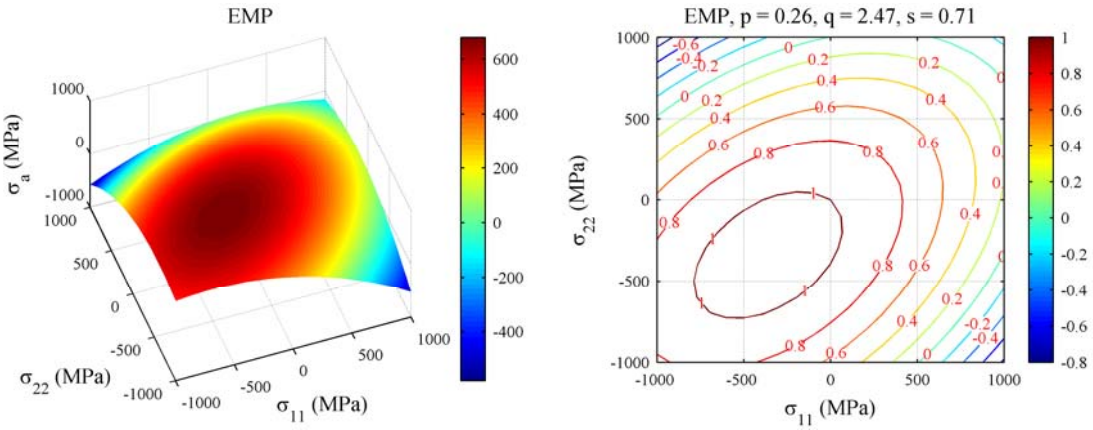

Fig. 10: Evaluation of fatigue limit and residual stress factor according to EMP.

Fig. 10 shows that the fatigue limit decreases when the tensile residual stresses increase. It can be also derived that an increase in compressive residual stress leads to an increase in fatigue limit. When the effective stress level, resulting from a combination of residual and applied stress, exceeds the yield stress, the surface layer becomes plastic and relaxation takes place. This effect causes a decrease in fatigue limit. In other words a further increase in the residual stress factor is limited when the yield stress level is exceeded.

Table 7 shows the residual stress factor calculated using SIH, QVH and EMP for different surface finishes studied in this paper. F_S denotes the surface fatigue factor [29].

Surface finish	F_S	σ_{11} [MPa]	σ_{22} [MPa]	$F_{RS,SIH}$	$F_{RS,QVH}$	$F_{RS,EMP}$
Turning	0.977	118	239	0.924	0.964	0.944
	0.993	220	291	0.862	0.920	0.909
	0.897	205	287	0.871	0.927	0.914
	0.961	307	339	0.798	0.872	0.872
	0.988	510	442	0.593	0.726	0.766
	0.968	597	490	0.458	0.649	0.712
Grinding	0.974	-195	-372	1.050	1.001	1.066
Peening	0.907	-478	-488	1.075	0.975	1.097
Peening & Grinding	0.974	-425	-498	1.070	0.992	1.100

Table 7: Residual stress factor for different surface finishes using stabilized surface residual stresses.

The surface fatigue factor and residual stress factor are used to predict the fatigue limit using an empirical formula as shown in Eq. (30).

$$\sigma_a = \sigma_W \cdot F_S \cdot F_{RS} \cdot n_\chi \qquad \text{Eq. (30)}$$

where n_χ represents the gradient effect due to the type of loading (tension-compression and bending) and called the fatigue ratio factor [30]. Fig. 11 illustrates the variation of n_χ as a function of stress gradient χ for the specimens having a diameter, d_0 = 7.5 mm according to the FKM-Guideline [31].

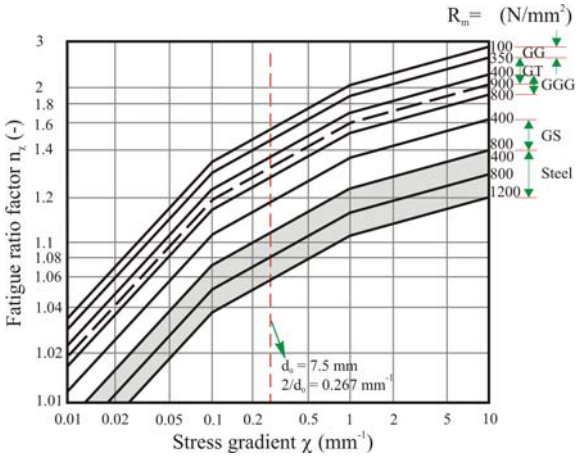

Fig. 11: Fatigue ratio factor for the specimen with diameter d_0 = 7.5 mm [31].

For the material investigated in this study (34CrNiMo6 steel quenched and tempered) the value of n_χ is 1.06. The fatigue ratio factor can also obtain from Eq. (31) according to Eichlseder [30].

$$n_\chi = 1 + \left(\frac{\sigma_b}{\sigma_W} - 1 \right) \cdot \left(\frac{\chi}{2/d_0} \right)^{K_D} \qquad \text{Eq. (31)}$$

where σ_b is the fatigue limit for alternating bending loading.

Fatigue tests under various surface conditions were performed by repeated rotating bending of test specimens with a diameter of 7.5 mm. The source of specimen failure was fatigue crack initiation from discontinuities existing at the machined surface followed by crack propagation until the flaw reached a critical length Fig. 12.

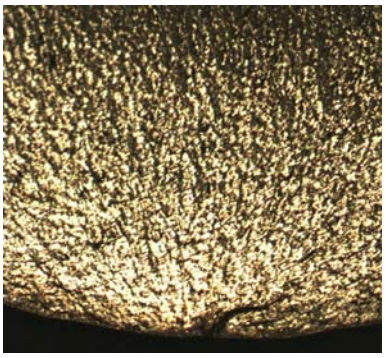

Fig. 12: Typical fatigue fracture surface of the investigated specimens.

Fig. 12 illustrates a typical micrograph found using confocal scanning laser microscopy. For all investigated specimens the origin of failure was at the surface. For the turned specimens, it is natural that the crack source comes from the surface, where the maximum tensile residual stress occurs. For the peened or ground specimens, the crack origin at the surface can be explained in this way that the high applied cyclic tensile stresses caused by loading surpass the compressive residual stress field in the low cycle fatigue region.

The results of the fatigue tests are listed in Table 8.

Surface finish	$\sigma_{a,exp}$	$(\sigma_{a,predic})_{SIH}$	$(\sigma_{a,predic})_{QVH}$	$(\sigma_{a,predic})_{EMP}$
Turning	569	564	589	576
	574	535	571	564
	511	489	520	512
	429	480	524	524
	462	366	448	473
	434	277	393	431
Grinding	667	639	609	649
Peening	637	610	553	622
Peening & Grinding	670	651	604	669

Table 8: Results obtained from the experimental and calculated fatigue limit.

The prediction of the fatigue limit of different surface finishes was carried out by means of Eq. (30) where the residual stress factor F_{RS} is calculated by three different multiaxial fatigue methods such as SIH, QVH and EMP.

Fig. 13 presents a comparison between the experimental values of fatigue endurance limit and the predicted ones based on the investigated models discussed in this study.

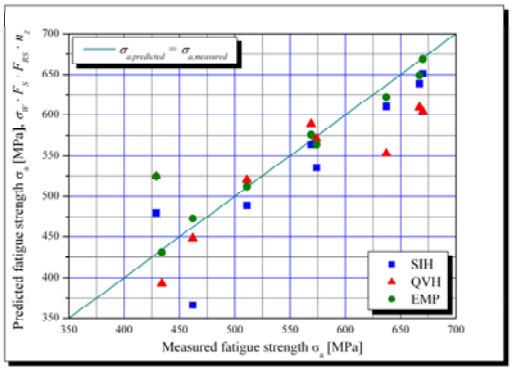

Fig. 13: Predicted vs. measured fatigue limit.

The comparison clearly shows that the proposed empirical model provides improved performance in the prediction of the fatigue limit.

4. Discussion

In order to evaluate the fatigue limit in the presence of residual stresses, a simple stress state which included two static biaxial normal stresses and an alternating axial stress was investigated. This stress state demonstrates the biaxial nature of residual stresses at the surface after machining which was imposed by the applied load.

To estimate the residual stress factor as an appropriate factor to correct the fatigue limit, two multiaxial fatigue criteria were employed in this study. The stabilized residual stresses at the surface were used to calculate the residual stress factor. This consideration provides a simple method to take into account the effect of residual stresses but their distribution below the surface is neglected. In other words, surface residual stresses take into account the crack initiation at the surface, however, the crack propagation at a distance below the surface is not considered.

The present authors employed the integral method to incorporate the residual stress distribution below the surface Eq. (32).

$$\sigma_{ij} = \frac{1}{l_0} \cdot \int_0^{l_0} \sigma_{RS}(x)\, dx \qquad \text{Eq. (32)}$$

where σ_{ij} is the axial (σ_{11}) or circumferential (σ_{22}) residual stresses. For the material investigated in this study, reasonable results were merely obtained for the value of l_0 very close to the surface where $l_0 \approx 0$.

Due to this observation, surface residual stresses were applied to evaluate the fatigue limit and their distribution below the surface was neglected. Nevertheless, it seems that the length l_0 would be a function of the micro structural length a_0, which characterizes the material behavior. Further investigation is needed to establish the correlation between residual stress and fatigue limit based on fracture mechanisms in the low fatigue crack growth region.

An empirical model was given to evaluate the residual stress factor. This model provides improved performance in prediction of the fatigue limit. The experimental data reported in literature is employed to verify the empirical model presented in this study. As far as the authors are aware, the experimental data reported in literature to evaluate the stress state $\sigma_{xa} + \sigma_{xm}$, σ_{ym} is quite limited. The references [27] and [32] present some experimental results which are used to show the accuracy of the empirical model to predict the fatigue limit under a particular stress state. The materials presented in this literature are E335 and 20MnCr5 with the material number 1.0060 and 1.7147, respectively. The reported material data is listed in Table 9.

Reference	Material	σ_W (MPa)	σ_{Sch} (MPa)	τ_W (MPa)	R_m (MPa)	R_e (MPa)
El-Magd	E335	294	500	176	765	550
Lüpfert & Spies	20MnCr5	516	832	303	1028	940

Table 9: Reported material data according to [27] and [32].

Table 10 shows the experimental data and predicted results using the empirical model mentioned in Eq. (29).

Material	σ_{xm} (MPa)	σ_{ym} (MPa)	$\sigma_{a,exp}$ (MPa)	$\sigma_{a,predic}$ (MPa)	$\sigma_{a,predic}/\sigma_{a,exp}$ (-)
E335	0	0	294	294	1.000
	0	306	290	277	0.955
	0	459	259	260	1.005
	76	306	286	278	0.974
	76	459	259	267	1.030
	153	306	279	275	0.987
	153	459	263	268	1.021
20MnCr5	0	0	516	516	1.000
	416	0	416	416	1.000
	0	-214.4	506	514	1.017
	-276.5	-214.4	553	540	0.977
	381	-214.4	381	372	0.976
	0	-428.8	502	503	1.003
	-285.5	-428.8	571	571	1.000

Table 10: Experimental data and predicted results obtained from the EMP model.

For the E335 and 20MnCr5 material the calculated values of the parameter p are 0.195 and 0.125, respectively. The fitting parameters q and s were determined using a regression analysis to obtain a least squares fitting for the data from Table 10.

Fig. 14 demonstrates the Haigh diagram calculated using EMP (empirical model) for biaxial mean stresses from the data listed in Table 10.

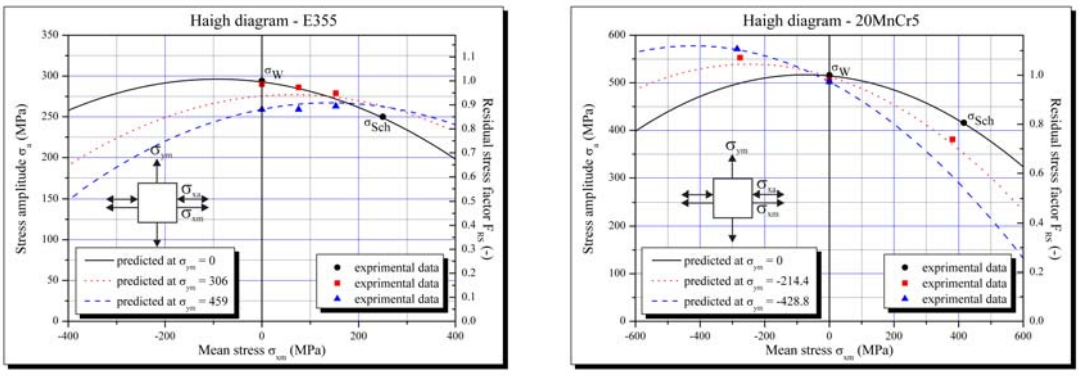

Fig. 14: Correlation between calculated and measured data using the Haigh diagram.

As can be derived, there is a fairly good agreement between predicted and measured data. Results show that the EMP model is able to evaluate the experimental data either in the tensile or in the compressive mean stress region.

Further experimental work is needed to validate this model for different materials.

5. Conclusion

From an investigation into the effect of residual stress on the fatigue strength of a quenched and tempered steel the following conclusions can be drawn.

1. The surface residual stresses are multiaxial, therefore a method for uniaxial stress evaluation is not appreciable.

2. The residual stresses were tensile in all the turning conditions while grinding and peening processes presented compressive residual stresses.

3. In the case of turned specimens, residual stresses are dominated by the process parameters namely feed rate and nose radius. An increase in feed rate and nose radius leads to an increase in residual stresses in both the axial and circumferential directions.

4. Not only the magnitude of residual stress at a special point but also its distribution at a distance will act on the short crack propagation and influence the fatigue limit.

5. The empirical model proposed in this study can evaluate the residual stress effect well.

6. To validate the empirical model for other materials or for other manufacturing processes which give rise to residual stress, additional tests are required.

Acknowledgements

This work was supported by Austrian Aeronautics Research. The authors would also like to thank Robert Schreiber and his team at Pankl Racing Systems Group for their support in sample machining.

References

[1] H. Jia-wen, H. Zhi-zhong and Z. Ding-quan, Influence of residual stress on fatigue limit in various carbon steels, International Conference on Shot Peening ICSP II Chicago 14-17 May, (1984) 340-345.

[2] Z. Jian-zong, H. Nai-sai and Z. Hui-jiu, Effect of shot peening on hardened high carbon steel and its mechanism, International Conference on Shot Peening ICSP II Chicago 14-17 May, (1984) 225-230.

[3] X. Jia-chi, Z. Ding-quan and S. Bang-jun, The fatigue strength and fracture morphology of leaf spring steel after prestressed shot peening, International Conference on Shot Peening ICSP I Paris 14-17 Sept., (1981) 367-373.

[4] K. Koibuchi, T. Hayama and S. Kawai, Residual stress and fatigue strength of surface hardened components, International Conference on Shot Peening ICSP I Paris 14-17 Sept., (1981) 413-419.

[5] P. Starker, H. Wohlfart and E. Macherauch, Biegewechselfestigkeit und Grösseneffekt bei unterschiedlich wärmebehandelten Stahlproben aus CK45 nach Kugelstrahlen, International Conference on Shot Peening ICSP I Paris 14-17 Sept., (1981) 613-623.

[6] R.L. Mattson and J.G. Roberts, The effect of residual stress induced by strain-peening upon fatigue strength, SAE Trans., 68 (1960) 130-136.

[7] J.F. Flavenot and N. Skalli, A comparison of multiaxial fatigue criteria incorporating residual stress effects, Biaxial and Multiaxial Fatigue, EGF 3 (Edited by M.W. Brown and K.J. Miller), Mechanical Engineering Publications, London, (1989) 437-457.

[8] Y.S. Garud, Multiaxial fatigue: A survey of the state of the art, Journal of Testing and Evaluation, 9(3) (1981) 165-178.

[9] G. Crossland, Effect of large hydrostatic pressures on the torsional fatigue strength of an alloy steel, Proc. of the Int. Conf. of Fatigue of Metals, London, (1956) 138-149.

[10] K. Dang Van, B. Griveau and O. Message, On a new multiaxial fatigue limit criterion: theory and application, Biaxial and Multiaxial Fatigue, (Edited by M.W. Brown and K.J. Miller), Mechanical Engineering Publications, London, (1989) 479-496.

[11] B. You and S. Lee, A critical review on multiaxial fatigue assessments of metals, Int. J. Fatigue, 18(4) (1996) 235-244.

[12] A. Karolczuk and E. Macha, A review of critical plane orientations in multiaxial fatigue failure criteria of metallic materials, Int. J. Fracture, 134 (2005) 267–304.

[13] V.V. Novozhilov, Theory of elasticity, (Translated from Russian by J.K. Lusher), Pergamon Press, London, 1961.

[14] A. Simbürger, Festigkeitsverhalten zäher Werkstoffe bei einer mehrachsigen phasenverschobenen Schwingbeanspruchung mit körperfesten und veränderlichen Hauptspannungsrichtungen, LBF-Bericht Nr. FB-121, Laboratorium für Betriebsfestigkeit, Darmstadt, 1975.

[15] H. Zenner, R. Heidenreich and I. Richter, Schubspannungsintensitätshypothese, Erweiterung und experimentelle Abstützung einer neuen Festigkeitshypothese für schwingende Beanspruchung, Konstruktion, 32 (1980) 143-152.

[16] H. Zenner and I. Richter, Eine Festigkeitshypothese für die Dauerfestigkeit bei beliebigen Beanspruchungskombinationen, Konstruktion, 29 (1977) 11-18.

[17] J. Liu, Beitrag zur Verbesserung der Dauerfestigkeitsberechnung bei mehrachsiger Beanspruchung, PhD thesis, Technical University of Clausthal, 1991.

[18] J. Liu and H. Zenner, Fatigue limit of ductile metals under multiaxial loading, Proc. of the 6th Int. Conf. on Biaxial/Multiaxial Fatigue and Fracture, Lisbon, (2001) 147-164.

[19] J. Liu, Weakest link theory and multiaxial criteria, Proc. of the 5th Int. Conf. on Biaxial/Multiaxial Fatigue and Fracture, Cracow, (1997) 45-62.

[20] W. Schütz, View points of material selection for fatigue loaded structures (in German), LBF-Bericht Nr. TB-80, Laboratorium für Betriebsfestigkeit, Darmstadt, 1968.

[21] H. Zenner, A. Simbürger and J. Liu, On the fatigue limit of ductile metals under complex multiaxial loading, International Journal of Fatigue, 22 (2000) 137-145.

[22] A. Troost and E. El-Magd, Allgemeine quadratische Versagensbedingung für metallische Werkstoffe bei mehrachsiger schwingender Beanspruchung, Metall, 31. Jahrgang, 7 (1977) 759-764.

[23] A. Troost and E. El-Magd, Allgemeine Formulierung der Schwingfestigkeitsamplitude in Haighscher Darstellung, Materialprüfung, 17(2) (1975) 47-49.

[24] J. Goodman, Mechanics applied to engineering, Longmans, Green & Co., New York, 1899.

[25] W. Gerber, Bestimmung der zulässigen Spannungen in Eisenkonstruktionen, Z. d. Bayerischen Architekten u. Ingenieurvereins, 6(6) (1874) 101-110.

[26] H. Dietmann, Festigkeitsberechnung bei mehrachsiger Schwingbeanspruchung, Konstruktion, 25(5) (1973) 181-189.

[27] E. El-Magd and S. Mielke, Dauerfestigkeit bei überlagerter zweiachsiger statischer Beanspruchung, Konstruktion 29(7) (1977) 253-257.

[28] A. Javidi, U. Rieger and W. Eichlseder, The effect of machining on the surface integrity and fatigue life, International Journal of Fatigue, 30 (2008) 2050–2055.

[29] A. Javidi, U. Rieger and W. Eichlseder, Estimating the surface fatigue factor of different surface finishes to predict the fatigue strength, in Submission.

[30] W. Eichlseder, Fatigue analysis by local stress concept based on finite element results, Computers and Structures, 80 (2002) 2109-2113.

[31] FKM-Guideline, Analytical strength assessment of components in mechanical engineering, 4th edition in German, VDMA-Verlag, Frankfurt/M., 2002.

[32] H.P. Lüpfert, H.J. Spies and P. Trubitz, Modelling and experimental verification of fatigue strength under multiaxial static pressure loading, 7th International Conference on Biaxial/Multiaxial Fatigue and Fracture, Berlin, (2004) 535-540.